DISSERTATION

The Vehicular Radio Channel in the 5 GHz Band

ausgeführt zum Zwecke der Erlangung des akademischen Grades eines
Doktors der technischen Wissenschaften

unter der Leitung von
Prof. Christoph F. Mecklenbräuker
Institut für Nachrichtentechnik und Hochfrequenztechnik

eingereicht an der Technischen Universität Wien
Fakultät für Elektrotechnik

von
Alexander Paier

Wien, im Oktober 2010

Die Begutachtung dieser Arbeit erfolgte durch:

1. **Prof. Christoph F. Mecklenbräuker**

   Institut für Nachrichtentechnik und Hochfrequenztechnik
   Technische Universität Wien

2. **Prof. Fredrik Tufvesson**

   Department of Electrical and Information Technology
   Lund University

to my little sister

Abstract

In this thesis I present a methodology, in order to characterize the time-variant vehicular radio channel. The radio channel is part of the communication system, which the engineer cannot influence. Therefore it has to be characterized in a way that the transmitters and receivers can be well designed, for specific applications. For this characterization we carried out two vehicular radio channel measurement campaigns in Lund, Sweden. In both campaigns we used a 4×4 multiple-input multiple-output channel sounder in the 5 GHz band. In general the radio channel can be described by the three main phenomena, pathloss, large-scale properties, i.e., shadowing, and small-scale properties, which I characterize by the concept of the Local Scattering Function (LSF). Pathloss models are developed for four different environments: rural, highway, urban, and suburban. For the rural environment a two-ray propagation model shows the best fit with the measurements. The pathloss for the other three environments is modeled via the classical power law model, with a pathloss exponent smaller than 2. The vehicular radio channel is highly time-variant, which is reflected in a non-Wide-Sense Stationary Uncorrelated Scattering (WSSUS) behavior. For the description of non-WSSUS radio channels, I use the concept of the LSF, which can be understood as a time- and frequency-variant scattering function. In this case the radio channel is assumed to be WSSUS for a limited region in the time domain (stationarity time) and frequency domain (stationarity bandwidth). I define and discuss the methodologies, in order to estimate the LSF from the measurement data. I observed a strong dependency of the stationarity time on the relative driving direction of the vehicles — in the range of double-digit milliseconds for vehicles driving in opposite directions and more than one second for vehicles driving in convoy. By investigations of the time-variant average power-delay profile and time-variant Doppler spectral density I observed that the most significant scatterers in vehicular environments are: traffic signs, trucks, bridges, and buildings.

Beside the channel measurements and characterization we carried out a communication system performance measurement campaign in Tyrol, Austria. As system we used a prototype implementation of the draft standard IEEE 802.11p, which is expected to be soon ratified and implemented in commercial vehicular communication systems. The Roadside Unit (RSU) was configured as the transmitter and the Onboard Unit (OBU) as receiver. In our vehicle-to-infrastructure measurements we investigated the performance of the Physical Layer (PHY) of IEEE 802.11p downlink broadcast with a *transparent* medium access layer (i.e., without retransmissions). This investigation of the PHY in real-world scenarios allows us to identify strengths for future PHY improvements to enable dependable connectivity. It turned out that the metal pillars of the gantry, where the RSU antenna was mounted, lead to an unsymmetric antenna pattern and therefore to an unsymmetric coverage area. Such an influence has to be taken into account for a IEEE 802.11p site planning. The road traffic on the lanes between the low RSU (1.8 m) and the OBU is shadowing the link between them and therefore strongly influences the performance of the IEEE 802.11p system. The maximum achievable coverage range at the high RSU (7.1 m) is about 700 m and was achieved with the lowest possible data rate of 3 Mbit/s. This coverage range decreases to less then 100 m at a data rate of 27 Mbit/s. For the low RSU the maximum achievable coverage range was up to 900 m, but varied strongly with the road traffic. The maximum correct received data volume, driving by the RSU, was achieved at low data rates of 4.5 Mbit/s, 6 Mbit/s, and 9 Mbit/s, which are using BPSK and QPSK as modulation scheme.

Kurzfassung

> *"Dem Ingeniör ist nichts zu schwör!"*
> DANIEL DÜSENTRIEB

In dieser Dissertation stelle ich eine Methodik zur Charakterisierung des zeitvarianten Fahrzeug-Funkkanals dar. Der Funkkanal ist Teil eines Kommunkationssystems, worauf man als Techniker keinen Einfluss hat. Darum muss er in einer Art und Weise charakterisiert werden, so dass Sender und Empfänger für spezifische Anwendungen entworfen werden können. Für so eine Charakterisierung haben wir zwei Fahrzeug-Funkkanal-Messkampagnen in Lund, Schweden durchgeführt. In beiden Messkampagnen verwendeten wir ein 4 × 4 Mehrfach-Eingabe Mehrfach-Ausgabe Kanalmessgerät (MIMO channel sounder) im 5 GHz Band. Im Allgemeinen kann der Funkkanal mittels drei Hauptphänomenen beschrieben werden, Streckendämpfung, großräumige Eigenschaften, d.h. Abschattung und kleinräumige Eigenschaften, welche ich mittels dem Konzept der lokalen Streufunktion (LSF) charakterisiere. Es wurden Streckendämpfungsmodelle für vier verschiedene Umgebungen entwickelt: ländlich, Autobahn, städtisch und vorstädtisch. Für die ländliche Umgebung zeigte ein Zwei-Strahlen Modell die beste Übereinstimmung mit den Messungen. Die Streckendämpfung für die drei anderen Umgebungen ist mit einem klassischen Leistungs-Gesetz-Modell, mit einem Streckendämpfungsexponenten kleiner als 2, modelliert. Der Fahrzeug-Funkkanal ist stark zeitvariant, was sich in einer "nicht-schwach-stationärer-unkorrelierter-Streuer" (non - wide sense stationary uncorrelated scatterer (WSSUS)) Eigenschaft widerspiegelt. Für die Beschreibung eines nicht-WSSUS Funkkanals verwende ich das Konzept der LSF, welche als zeit- und frequenzabhängige Streufunktion angesehen werden kann. In diesem Fall wird angenommen, dass der Funkkanal in einem begrenzten Bereich über die Zeit (Stationaritätszeit) und über die Frequenz (Stationaritätsbandbreite) die WSSUS Bedingungen einhält. Ich definiere und diskutiere die Methodik, um die LSF aus den Messdaten zu schätzen. Dabei beobachtete ich eine starke Abhängigkeit der Stationaritätszeit von der relativen Fahrtrichtung der Fahrzeuge

zueinander — im Bereich zweistelliger Millisekunden für Fahrzeuge, welche in entgegengesetzter Richtung fahren und mehr als eine Sekunde für Fahrzeuge, welche im Konvoi fahren. Bei Untersuchungen des mittleren Verzögerungs-Leistungsdichte-Spektrums und des Doppler-Leistungsdichte-Spektrums beobachtete ich folgende signifikante Streuer: Verkehrsschilder, Lastkraftwagen, Brücken und Gebäude.

Neben den Kanalmessungen und der Kanalcharakterisierung haben wir eine Kommunikationssystem-Effizienz-Messkampagne in Tirol, Österreich durchgeführt. Als System verwendeten wir eine Prototyp-Implementation des derzeitigen Entwurfs der Norm IEEE 802.11p, welche voraussichtlich in naher Zukunft ratifiziert und in kommerzielle Fahrzeug-Kommunikationssysteme implementiert wird. Die Straßeneinheit (roadside unit (RSU)) wurde als Sender konfiguriert und die Bordeinheit (onboard unit (OBU)) als Empfänger. In unseren Fahrzeug-zu-Infrastruktur Messungen haben wir die Effizienz der physikalischen Schicht (physical layer (PHY)) der IEEE 802.11p Abwärtsstrecke im Rundfunk-Betrieb mit einer *transparenten* Medienzugriffssteuerung (medium access control (MAC)) (d.h. ohne Sendewiederholungen) untersucht. Diese Untersuchung der PHY in realen Szenarien ermöglicht uns Stärken für zukünftige PHY Verbesserungen für zuverlässige Verbindungen zu identifizieren. Es zeigte sich, dass die metallischen Stützpfeiler der Signalbrücken, wo die RSU Antenne montiert war, zu einem unsymmetrischen Antennenrichtdiagramm und darum zu einem unsymmetrischen Sendegebiet führen. Dieser Einfluss muss bei der IEEE 802.11p Zellplanung berücksichtigt werden. Der Straßenverkehr auf den Fahrspuren zwischen der niedrigen RSU (1.8 m) und der OBU schattet die Verbindung zwischen ihnen ab und beeinflusst daher die Effizienz des IEEE 802.11p Systems stark. Die maximal erreichbare Sendereichweite der hohen RSU (7.1 m) beträgt ca. 700 m und wurde mit der kleinstmöglichen Datenrate von 3 Mbit/s erzielt. Diese Sendereichweite sinkt auf weniger als 100 m bei einer Datenrate von 27 Mbit/s. Für die niedrige RSU ist die maximal erreichbare Sendereichweite bis zu 900 m, schwankt aber stark mit dem Straßenverkehr. Das maximal korrekt empfangene Datenvolumen, wenn man an der RSU vorbeifährt, wurde bei niedrigen Datenraten von 4.5 Mbit/s, 6 Mbit/s und 9 Mbit/s erzielt, welche BPSK und QPSK Modulationsschemen verwenden.

Acknowledgments

First, I would like to thank my supervisor Christoph. It was really a nice experience to work with him during the past 4 years. I have learned a lot from him and enjoyed the joint days, evenings, and nights at conferences, meetings, and campaigns in foreign countries. Further, I want to thank my second examiner Fredrik for patiently awaiting my final thesis delivery and the nice weeks during the measurement campaigns in Lund. I have got a little insight into the way of life in Sweden, e.g., when I saw him singing in a choir inside a church.

Big thanks to my mother and her boyfriend for motivating me, every time when I saw them, which was not very often this year. Very special thanks go to my little sister, big sister, an my big brother for always supporting me (in good days and in bad days), which was very important to me, especially in the last months before finishing my thesis. Further thanks to my cousin Danuel for all the nice discussions in this eventful year 2010.

I have really enjoyed to carry out the measurement campaigns with friendly people, which helped to have fun during the sometimes exhausting work. Therefore, I want to thank the LUND'07 team Charlotte, Christoph, Fredrik, Johan, Helmut, Niki, and Andy. I am grateful for the cooperation with the DRIVEWAY'09 team, Laura, Oliver, Andreas, Fredrik, Johan, Andreas, Niki, Andy, and Yi, and just want to mention "*Tango to Romeo*!" and a funny wine evening. Special thanks are going to my copilot on the long way from Hannover to Lund and during the measurement week. Further, I want to thank the REALSAFE team Arrate, Roland, Dieter, Yi, Christoph, and Niki for the nice days in Tyrol.

Many thanks to Veronika for the support in the last weeks finishing my thesis after I have guided her to the master-certificate (roles can change!).

I don't want to forget to say thanks to the lunch group, where there was always time for sarcastic jokes about writing a PhD thesis. And last but not least I want to thank *The NoiSy cOOks* for the mental and ironic forces finalizing this thesis.

Contents

1

Introduction

SIGNIFICANT reduction of traffic congestions and road accidents is a serious challenge throughout the world. In order to address these challenges, expensive sensors, radars, cameras, and other technologies are currently implemented in vehicles, in order to enhance driver comfort and improve the vehicle safety. Recently, wireless communication-based applications, including Vehicle-to-Vehicle (V2V) and Vehicle-to-Infrastructure (V2I) communications, have attracted more attention from industry and governments, especially in the United States, Europe, Japan, and Australia. Vehicular communication applications have the potential to reduce traffic congestions and road accidents. Currently car manufacturers as well as road- and infrastructure operators are working together on a common standard for a vehicular communication system. The proposed standard IEEE 802.11p is an amendment to the well known Wireless Local Area Network (WLAN) standard IEEE 802.11 and is expected to be ratified in the near future.

The development of a dependable wireless communication system requires a deep understanding of the underlying propagation channels. However, the time-frequency selective fading of vehicular communication channels notably differs from the better explored cellular channels. Therefore dedicated radio channel measurement campaigns, radio channel characterization, and channel models are required. Before 2006, wideband vehicular radio channels were rarely investigated. Starting with 2006 the number of vehicular radio channel measurements has increased significantly.

Vehicular narrowband channel measurements were carried out by Cheng et al. [1], [2] and by Maurer et al. [3] already in 2002. Wideband measurements, in which the whole impulse response of the channel is recorded, were carried out with correlative sounders [4] by Sen et al. [5], Cheng et al. [6], Acosta and Ingram [7], Tan et al. [8], Paschalidis et al. [9], and Kunisch and Pamp [10]. Wideband measurements using multitone sounding (Orthogonal Frequency Division Multiplexing (OFDM)-like sounding signals) were practiced by Paier et al. [11], [12]. Multiple-Input Multiple-Output (MIMO) channel measurements were conducted by Renaudin et al. [13] as well as in [11] and [12]. An overview of the measurement results (pathloss, fading statistics, Doppler spreads, and delay dispersion) of the mentioned measurements is given in [14].

The first vehicular (V2V and V2I) radio channel measurement campaign under my guidance, was carried out in April 2007, where there was still a lack of vehicular measurement campaigns. It was one of the first MIMO channel measurements between vehicles in real-traffic scenarios. A further novelty is the methodology of characterizing the vehicular radio channel. Since vehicular scenarios are changing very fast, i.e., the radio channel is time variant, the radio channel does not fulfill anymore the Wide-Sense Stationary Uncorrelated Scattering (WSSUS) assumption [4]. Therefore I use the concept of the Local Scattering Function (LSF) [15] that can be seen as time- and frequency-variant scattering function for the characterization of the channel. As pointed out in [14] there was a lack of several aspects of vehicular channel measurements until 2009. In most of the measurements, the measurement vehicles were either driving in convoy of in opposite directions. Such scenarios do not really apply to many safety-critical V2V applications, e.g., collision avoidance in intersections, traffic congestions or when vehicles enter highways on entrance ramps. Further, only a few measurements were carried out with a realistic antenna mounting from a car manufacturer point of view. Usually a test antenna was used, mounted in an elevated position. Last but not least, the impact of vehicles, obstructing the direct path between Transmitter (Tx) and Receiver (Rx) as well as the possible gains of using multiple antenna elements at Tx and/or Rx has been little explored. We considered these missing issues especially in our second V2V channel measurement campaign in 2009. I selected specific traffic situations that are of particular interest for safety-related Intelligent Transport Systems (ITS) applications. We used realistic automotive multi-element antennas, especially designed for vehicular usage and realistic antenna mounting. Several traffic situations were chosen, where the Line-of-Sight (LOS) path was obstructed. As for the evaluation of the measurement data of the first campaign, I used the concept of the LSF for the characterization of the radio channel.

The IEEE 802.11p standard is based on OFDM [16], [17]. Before this standard is implemented in vehicular communication systems its performance needs to be evaluated, whether it complies with the strict requirements of ITS.

In [18] measurements with standard IEEE 802.11a/b/g equipment in V2V and V2I scenarios show that the vehicle distance and availability of line-of-sight (LOS) are very important performance factors. Further they observe higher number of retransmissions for larger packet sizes and a reduced communication range for higher-order modulation schemes. The work in [19] investigates the performance of IEEE 802.11a with different bandwidths and compares measured V2V channel parameters with critical parameters of IEEE 802.11a/p. The most critical parameter they found is the packet length, because it is longer than the coherence time of the radio channel, especially when using the smaller bandwidth of 10 MHz in IEEE 802.11p compared with 20 MHz in IEEE 802.11a. In [20] the modifications of IEEE 802.11p related to IEEE 802.11a, in order to make the new standard IEEE 802.11p more robust in vehicular scenarios are presented. Several investigations deal with simulation based performance evaluations, e.g., [21], [22].

Currently there are more simulation results available than results from real-world measurements of the standard IEEE 802.11p. For the simulations, realistic channel models have to be implemented, which is not always the case in the current available publications. Therefore it is necessary to carry out measurements in real-traffic scenarios, in order to evaluate the performance of IEEE 802.11p. For this reason we conducted a real-world measurement campaign, in order to evaluate the performance of the Physical Layer (PHY) in V2I scenarios. The dependency of different parameter settings at the Tx, e.g., packet length, data rate, and Tx power, on the coverage range and correctly received data volume, is the focus of these investigations.

During the work on this thesis I published several papers since 2006 as first author or as co-author. The content of most of them is discussed in this final thesis: In [11], [23], and [24] I give a description of the channel measurement campaign carried out in 2006 and characterize the radio channel in the time-delay and Doppler-delay domain. Pathloss models of four different scenarios are presented in [25]. The concept of applying the LSF estimator on vehicular measurement data is explained in [26] and [27]. In [28] and [29] a geometry-based stochastic channel model for highway scenarios is explained. A description of the second channel measurement campaign and results of the time-varying Average Power-Delay Profile (APDP) and Doppler Spectral Density (DSD) are presented in [12], [30], and [31], where the latter one is dealing with the vehicular antenna integration and design. In [32] I describe the measurement practice and performance results from our IEEE 802.11p system measurements. An overview about vehicular channel characterization and its implications for wireless system design and performance is presented in [33].

Other papers are not directly related with the work of this thesis and therefore not included: In [34] I present the spatial diversity and spatial correlation evaluation of measured V2V radio channels. Based on this paper the temporal evolution of channel capacity is presented in [35] and [36]. [37] describes the estimation of spectral divergence and coherence parameters for vehicular channels and [38] shows the Ricean K-factor variation over time, frequency, and space. In [39] a comparison of different wireless technologies for V2I communications is presented and [40] investigates the indoor coverage prediction and optimization of Universal Mobile Telecommunications System (UMTS) macro cells.

The remainder of this thesis is structured as follows. In Ch. 2 I give an overview about the history and state-of-the-art of vehicular communications, including the main research projects and standardization work. Chapter 3 describes the theory of time-variant radio channels, where I start with the basic mechanisms that govern the propagation of electromagnetic waves, emphasizing those aspects that are relevant for wireless communications. Further I explain the system-theoretic description of the radio channel, especially for non-WSSUS channels, which are the basics for the characterization of the time-variant vehicular radio channel. In Ch. 4 the two vehicular radio channel measurements and the IEEE 802.11p PHY performance measurements are described in detail. This description is followed by Ch. 5, where I characterize the vehicular radio channel based on our measurements. I explain the methodologies, in order to estimate the main characterization parameters and functions, i.e., pathloss, LSF, APDP, and DSD. This chapter closes with an explanation, why the proposed channel model in the early versions of the draft standard IEEE 802.11p does not reflect the real behavior of vehicular radio channels and suggestions for more reasonable channel models. In Ch. 6 I present performance evaluations of the IEEE 802.11p PHY measurement campaign in terms of distinguishing effects caused by specific propagation environments and effects due to different parameter settings. Conclusions of the work of this thesis are drawn in Ch. 7 followed by an outlook and future directions in Ch. 8.

2

Vehicular Communications — an Overview

VEHICLES "talking" to each other on the road will soon be reality. The number of vehicles is increasing and increasing. This increase leads to more traffic congestions and higher risk of accidents. The International Transport Research Documentation (ITRD) [41] is tracking the number of deaths on the roads since 1972. Passive safety applications, e.g., safety seat belt, airbag, Anti-Lock Braking System (ABS), helped to reduce the number of deaths on the road. In the 80s first research programs investigated the improvement of traffic safety and traffic efficiency by the use of wireless technologies for vehicular communications. Whereas passive safety systems try to lower the intensity of the accident, active safety systems intend to avoid an accident in advance. In addition to their use for active safety, vehicular communications potentially reduce congestions, travel-time and pollution through traffic efficiency applications. Further, vehicular communications support the availability of entertainment and information systems in vehicles. Overall vehicular communications applications can be classified in three major groups: *traffic safety applications*, *traffic efficiency applications*, and *commercial applications*. The communication requirements of each application significantly differ from each other. Safety applications require strict short predictable deadlines of the delay as well as reliability, whereas commercial applications require high data rates. The focus of my research on wireless channels and technology is on traffic safety applications, which include collision avoidance, hazardous location notification, wrong-way driving warning, and lane change assistance. A basic set of applications is defined in [42].

One of the first pan European programs was the Programme for a European Traffic of Highest Efficiency and Unprecedented Safety (PROMETHEUS) during 1987-1995, where driverless cars where driving in convoy and other cars were automatically tracked. Later on the activities in the field of vehicular communications diminished for several reasons. One reason was the lack of cost efficient radio technologies for such communications. Further the car manufacturers did not see the immediate benefits of vehicular communications systems. In the last ten years the number of research programs focusing on vehicular communications systems under the new keyword *cooperative systems* is increasing. One main impulse for these investigations was the allocation of a 75 MHz band at $5.850 - 5.925$ GHz dedicated to ITS in North America, by the Federal Communications Commission (FCC) in the year 1999.

In Europe there were/are several large projects dealing with cooperative systems, predominantly funded by the European Commission (EC), e.g., Preventive and Active Safety Applications (PReVENT), Network on Wheels (NoW), Safe Cooperative Driving — Smart Vehicles on Smart Roads (SAFESPOT), Cooperative Vehicle-Infrastructure Systems (CVIS), Cooperative Systems for Intelligent Road Safety (COOPERS), Preparation for Driving Implementation and Evaluation of C2X Communication Technology (PRE-DRIVE C2X), and Sichere Intelligente Mobilität — Testfeld Deutschland (SIM-TD). Further there exists a specific support action named Communications for eSafety (COMeSafety) [43] and the well-established "Car-to-Car Communication Consortium (C2C-CC)" [44].

The main goal of the PReVENT [45] project was to reduce the number of deadly accidents by 50 % until 2010. The project develops, demonstrates, and evaluates preventive safety applications by using advanced sensor, communication, and positioning technologies integrated into on-board systems for driver assistance. The national German project NoW [46] (2004-2008) focused on communication links. The main objectives of this project were to solve technical key questions on the communication protocols and data security for V2V communications and to submit the results to the standardization activities of the C2C-CC. SAFESPOT [47] targets traffic safety related applications, by developing key enabling technologies, i.e., ad hoc dynamic network, accurate relative localization, and dynamic local traffic maps. The CVIS [48] project focuses on the communications architecture and system concepts for a number of cooperative system applications. Common core components were developed, in order to support cooperation models in real-life applications. COOPERS [49] develops innovative telematics applications on the road infrastructure. The long term goal is a cooperative traffic management between vehicle and infrastructure, in order to reduce the gap of the development of telematics applications between car industry and infrastructure operators. PRE-DRIVE C2X [50] prepares a large-scale field operational test for vehicular communication technology with input from other projects, e.g., the European COMeSafety architecture for a V2V as well as a V2I communication system. The German project SIM-TD [51] aims at the implementation of several applications on an integrated platform, explored in a large Field Operational Test (FOT). The main difference to other projects is the large number of test vehicles. About 100 *controlled* vehicles will be tested at specific test sites. Further about 300 *uncontrolled* vehicles will be in operation in usual workaday life in the field test area near Frankfurt/Main, Germany.

The C2C-CC and the mentioned projects are delivering input to the European standardization activities within European Telecommunications Standards Institute (ETSI) Technical Committee (TC) ITS, in order to ensure interoperability between different vehicle manufacturers.

2.1 Radio Technologies / Standardization

One big step ahead for the realization of vehicular communications was the FCC allocation of a 75 MHz band at 5.850 – 5.925 GHz especially dedicated for ITS in North America in 1999. The American Society for Testing and Materials (ASTM) was asked to define an ITS standard and proposed the Institute of Electrical and Electronics Engineers (IEEE) 802.11 standard for WLAN with minor changes for high-speed vehicular environments. They termed the standard Dedicated Short Range Communication (DSRC), which is somewhat confusing, because the term DSRC was already given to a type of Radio Frequency Identification (RFID) systems, e.g., Electronic Toll Collection (ETC) in Europe and Japan in the 80s. This leads to some misunderstanding, because DSRC refers to RFID systems in Europe an in Japan, whereas in North America it refers to a type of WLAN. All the DSRC frequencies are located in the 5 GHz band, but the specific bands depend on the region. Table 2.1 summarizes the band allocations.

Table 2.1: DSRC frequency bands

Region	**System**	**Standard**	**Frequency**
Europe	RFID	EN 12253	5.795 – 5.815 GHz
ITU-R	RFID	ITU-R M. 1453-2	5.725 – 5.875 GHz
Japan	RFID	ARIB T55	5.770 – 5.850 GHz
North America	WLAN	ASTM E 2213-02	5.850 – 5.925 GHz

IEEE has now taken over the work from ASTM and is developing IEEE 802.11p in the Task Group (TG)p, which amends the IEEE 802.11 both at the PHY and Medium Access Control (MAC) layer. IEEE 802.11p is intended for the frequency band allocation in North America, where the 75 MHz band is divided in seven 10 MHz channels, one control channel and six service channels. In addition to the PHY and MAC layer, defined in IEEE 802.11p, IEEE develops an entire protocol stack called Wireless Access in Vehicular Environments (WAVE). Beside IEEE 802.11p it also defines the application layer, IEEE 1609.1 [52], security, IEEE 1609.2 [53], network and transport layers, IEEE 1609.3 [54], and IEEE 1609.4 [55] for the usage of the frequency channels (which type of messages are admitted or prohibited on which channel). The TGp finalized the draft standard IEEE 802.11p in April 2010 and submitted it to the IEEE for approval. It is expected to be ratified in November 2010. Currently, there is no other competing standard for ad hoc communications between vehicles.

A more general specification of IEEE 802.11p is developed by the International Organization for Standardization (ISO) under the framework Communication Architecture for Land Mobiles (CALM), where it is called CALM M5. In this framework several wireless technologies like 2G/3G/Long Term Evolution (LTE), wireless broadband access (e.g., Worldwide Interoperability for Microwave Access (WiMAX)), WLAN, CALM M5, DSRC (as defined in Europe and Japan), will be integrated to provide seamless wireless connection for all end users.

Due to the already allocated frequency bands in Europe it was politically impossible to allocate the same 75 MHz band for ITS as in North America. However, a frequency band of 30 MHz at $5.875 - 5.905$ GHz was allocated by the EC devoted to safety-related ITS applications in 2008 [56]. These 30 MHz are divided in three 10 MHz channels, one control channel and two service channels. Further the frequency band below $5.855 - 5.875$ GHz will likely be used for non-safety ITS applications in the future. Currently the ETSI [57] is working on a standardization profile for IEEE 802.11p for the European 30 MHz band.

3

Theory of Time-Variant Radio Channels

THE radio channel is the communications medium from the Tx to the Rx. Its properties define all performance limits of wireless communications and determine the behavior of specific wireless systems. Therefore it is essential to characterize the radio channel from measurements, in order to understand it and to model it adequately. The main difference to wired channels is that in radio channels the transmitted signal propagates via multiple paths (multipath propagation) to the Rx. Each Multipath Component (MPC) may involve reflection, diffraction, refraction, scattering, and waveguiding. Another important characteristic of the radio channel is its time-variance. This is especially true for vehicular radio channels, where the Tx, the Rx, and the scatterers are moving.

These characteristics make the modeling of the radio channel quite complex. In principle the radio channel can be described with deterministic models based on Maxwell's equations [58], but for this you have to describe the environment in much detail: geometry, propagation media, and boundary conditions. This is not feasible in many scenarios because the number of involved objects is huge and the resulting simulation time becomes too large. Therefore it has become common to characterize the radio channel statistically.

In the first part, Sec. 3.1, I describe the propagation aspects of the radio channel, i.e., the phenomena of the wave propagation. This includes the three main phenomena, pathloss, large-scale fading, and small-scale fading. Further I explain multipath propagation and time variance of the radio channel. In the last subsection of the first part I describe the waveguiding effect that plays an important role in vehicular communications, because of the specific physical structure of roads and their local environment.

In the second part, Sec. 3.2, I give a system-theoretic description of the radio channel. This description is used for the evaluation and quantifying of radio channel measurement data. I start with a characterization of deterministic linear time-variant systems that are developed by Bello 1963 in the famous paper [59]. Further I describe the stochastic system functions, which specify the second order statistics of the radio channel. One of the most important properties of the radio channel is the Wide-Sense Stationary (WSS) and Uncorrelated Scattering (US) property. I explain this property and show when the WSSUS assumption is fulfilled. This explanation is followed by a description of quasi-WSSUS and non-WSSUS channels. The chapter closes with main measures of the radio channel, the delay spread and the duality in the Doppler domain, the Doppler spread that is a result from the time variance of the radio channel.

3.1 Propagation Aspects of the Radio Channel

3.1.1 Pathloss, Large-Scale Fading, and Small-Scale Fading

The propagation of electromagnetic waves in complex environments can be understood as superposition of MPCs [60], where the signal of each path can be reflected, diffracted, or scattered between the Tx and the Rx. If the surface of the interacting object, where the waves are impinging is smooth, compared to the wavelength, the waves are reflected. In this case the relation between the angles of the impinging waves and reflected waves is described by *Snell's law* (the angle of incidence is the same as the reflected angle). In the other case, if the surface is rough, compared to the wavelength, the waves are diffusely scattered. The third phenomenon, diffraction, occurs at edges of objects. The most important parameter describing the wave propagation is the channel gain, because it determines the received power. Its variation is generally described by

- pathloss,
- large-scale fading, and
- small-scale fading.

The *pathloss* is described in a deterministic manner. It describes the variation of the channel gain over distance. One simple model is the free space pathloss, also known as *Friis' law*

$$P_{\mathrm{Rx}}(d) = P_{\mathrm{Tx}} G_{\mathrm{Tx,iso}} G_{\mathrm{Rx,iso}} \left(\frac{\lambda}{4\pi d} \right)^2, \tag{3.1}$$

where d is the distance between Tx and Rx, λ the wavelength, $G_{\mathrm{Tx,iso}}$ and $G_{\mathrm{Rx,iso}}$ the antenna gains of the Tx and Rx, and P_{Tx} and P_{Rx} the transmitted power and the received power, respectively. It determines the monotonically decreasing of channel gain with increasing distance for the Tx antenna and Rx antenna in free space, i.e., there are no objects interacting with the wave propagation. Further, more sophisticated, deterministic equations also include the propagation mechanisms, reflection, scattering, and diffraction.

The *large-scale fading* describes the variation of the channel gain over a larger scale — typically a few hundred wavelengths. The reason for this effect is shadowing by large objects. It can be clearly seen by moving the Rx in a circle around the Tx (i.e., that there is no distance dependency) that no pathloss variation can be observed. Usually this variation is described by its statistics. A commonly used distribution for the large-scale fading is the log-normal distribution.

The *small-scale fading* describes the channel gain fluctuations on a very short distance — comparable with one wavelength. The reason for this fluctuation is interference among several MPCs, which I describe in more detail in Sec. 3.1.2. Similar to the large-scale fading it is common to describe the small-scale fading by its statistics. Since the physical interpretation of the small-scale fading and the large-scale fading is fundamentally different also the statistics are different. Two commonly used distributions for the small-scale fading are the Rice distribution [61] and the Rayleigh distribution. The Rice distribution occurs usually in situations if there is a LOS link between the Tx and Rx. If there is Non-Line-of-Sight (NLOS) between the Tx and Rx, the distribution of the channel gain often follows a Rayleigh distribution.

3.1.2 Multipath Propagation

One of the major differences between a wired channel and a wireless channel is that multipath propagation occurs in wireless channels. The transmitted signal is reflected, diffracted, and scattered and arrives via multiple paths, with different phases, different delays, and different amplitudes, at the Rx. Figure 3.1 depicts such a scenario. A further description of the three propagation phenomena (reflection, diffraction, and scattering) is given in Sec. 3.1.1.

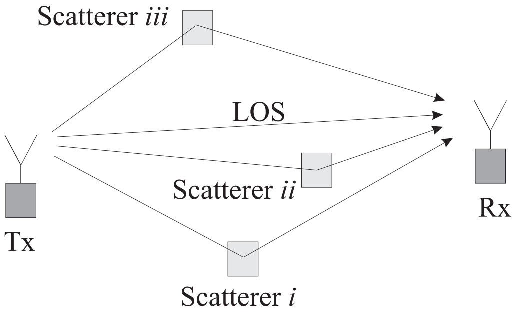

Figure 3.1: Multipath propagation scenario

Due to the superposition of the MPCs at the Rx, constructive and destructive interference occurs, which is known as small-scale fading. If there is a NLOS situation the Rayleigh distribution is most frequently used as model for the small-scale fading. The probability density function (pdf) of the Rayleigh distribution is given by

$$f_r(r) = \begin{cases} \frac{r}{\sigma^2} e^{-\frac{r^2}{2\sigma^2}}, & r \geq 0, \\ 0, & r < 0, \end{cases} \tag{3.2}$$

where r is the envelope of a signal that is zero-mean complex Gaussian with standard deviation σ. In the case of a LOS situation, i.e., one MPC has a dominant gain A^2, a Rice distribution is most commonly used to model the small-scale fading. The received signal is non-zero mean complex Gaussian and the Rice distribution is given by

$$f_r(r) = \begin{cases} \frac{r}{\sigma^2} e^{-\frac{r^2+A^2}{2\sigma^2}} I_0\left(\frac{Ar}{\sigma^2}\right), & r \geq 0, \\ 0, & r < 0, \end{cases} \tag{3.3}$$

where A is the amplitude of the dominant component and I_0 is the zero-order modified Bessel function of the first kind. The Rice distribution is usually characterized by its Ricean K-factor

$$K = \frac{A^2}{2\sigma^2}. \tag{3.4}$$

Then the pdf can be rewritten as

$$f_r(r) = \begin{cases} \frac{2(K+1)r}{\Omega} e^{-K-\frac{(K+1)r^2}{\Omega}} I_0\left(2\sqrt{\frac{K(K+1)}{\Omega}}r\right), & r \geq 0, \\ 0, & r < 0, \end{cases} \tag{3.5}$$

where $\Omega = \mathrm{E}\left\{r^2\right\}$ is the mean power. When $K = 0$, i.e., without dominant component, the Rice distribution reduces to the Rayleigh distribution.

As mentioned above, the MPCs arrive at the Rx at different delays, because the travel distance between the Tx and Rx differs for each path. This results in a frequency-variant signal and is called *frequency selective fading*. Delay dispersion is equivalent to frequency selectivity, which can be shown by performing Fourier transform from the delay τ domain to the frequency f domain, see Sec. 3.2.1 for further information.

The different delays of the signal for different MPCs cause Inter Symbol Interference (ISI). At the Rx the ith symbol arrives via a path with long delay and interferes with the $(i+1)$th symbol from a path with short delay.

3.1.3 Time Variance

Especially in vehicular communications we are confronted with time-variant channels, because the Tx, the Rx, and the scatterers are moving in V2V communications and either the Tx or the Rx and the scatterers are moving in V2I communications. The time selectivity causes a Doppler shift of the received frequency of

$$\nu = -f \cdot \frac{v}{c_0} \cos(\gamma), \tag{3.6}$$

where f is the frequency, v the relative speed between the Tx and Rx, c_0 the speed of light, and γ is the angle between direction of movement and direction of the impinging wave. If the direction of movement of the Rx is the same as the direction of the impinging wave ($\gamma = 0°$), i.e., Rx is moving away from the Tx, the Doppler shift is negative. In the other case, direction of Rx movement is in opposite direction as the impinging wave, ($\gamma = 180°$) the Doppler shift is positive.

3.1.4 Waveguiding

Waveguiding is of special interest in vehicular communications channels, because of the specific structure of the roads and their environment, e.g., street canyons, tunnels, traffic noise barriers, and guard rails. The basic equations of dielectric waveguiding are found in [62] and [63]. In vehicular communications these models have to be modified, because of the real-world environment (e.g., lossy materials, interrupted walls in street canyons, missing "upper" wall of the waveguide, and obstacles like vehicles). The propagation loss is increasing according to a power law with distance, $\propto d^n$, where n varies between 1.5 and 5. Note that the exponent can be smaller than 2, which is the exponent for free space propagation, see Eq. (3.1).

3.2 System-Theoretic Description of the Radio Channel

3.2.1 Characterization of Deterministic Linear Time-Variant Systems

The radio channel can be fully described by its Impulse Response (IR) $h(t, \tau)$. In the time-invariant case, the IR $h(\tau)$ does not depend on the time and the theory of Linear Time Invariant (LTI) systems can be used, [64]. In general, and especially for vehicular radio channels the IR $h(t, \tau)$ is varying with time. Thus, the theory of Linear Time Variant (LTV) systems has to be used. This generalization is not trivial and brings theoretical challenges. Mostly the channel is changing only slowly over time, i.e., that for each time a different IR can be considered. Such a channel is called quasi-static.

One of the most important publications about the characterization of time-variant linear channels was written by Bello [59]. The input-output relation is defined via the time-variant convolution

$$y(t) = \int_{-\infty}^{\infty} x(t-\tau) h(t, \tau) d\tau, \tag{3.7}$$

where $x(t)$ is the input signal and $y(t)$ is the output. Since the IR has two arguments, time t and delay τ, it is possible to define four different system functions via Fourier transform that are equivalent and each fully describes the channel. The *time-variant IR* $h(t, \tau)$ depends on time and on delay, the *time-variant Transfer Function (TF)* $H(t, f)$ depends on time and frequency, the *Doppler-variant IR* also known as *spreading function*

$S(\nu, \tau)$ depends on Doppler and on delay, and the *Doppler-variant TF* $B(\nu, f)$ depends on Doppler and on frequency. Figure 3.2 shows the relation between the four system functions that are found in [65].

$$\begin{tikzcd}
& h(t,\tau) \arrow[dl, dash, "\mathcal{F}_{\tau\leftrightarrow f}"'] \arrow[dr, dash, "\mathcal{F}_{t\leftrightarrow\nu}"] & \\
H(t,f) \arrow[dr, dash, "\mathcal{F}_{t\leftrightarrow\nu}"'] & & S(\nu,\tau) \arrow[dl, dash, "\mathcal{F}_{\tau\leftrightarrow f}"] \\
& B(\nu,f) &
\end{tikzcd}$$

Figure 3.2: Fourier relation between the system functions, [59]

3.2.2 Stochastic Second Order System Functions

Let us now model the radio channel as a the stochastic linear time-variant system. A full description requires the multidimensional pdf of the IR. Since this is usually unfeasible in practice, a second-order description, namely the Auto Correlation Function (ACF), is used. The ACF can be calculated out of the four stochastic system functions [59], [65]

$$R_h(t, t'; \tau, \tau') = \mathrm{E}\left\{h(t, \tau)h^*(t', \tau')\right\}, \tag{3.8}$$

$$R_H(t, t'; f, f') = \mathrm{E}\left\{H(t, f)H^*(t', f')\right\}, \tag{3.9}$$

$$R_S(\nu, \nu'; \tau, \tau') = \mathrm{E}\left\{S(\nu, \tau)S^*(\nu', \tau')\right\}, \text{and} \tag{3.10}$$

$$R_B(\nu, \nu'; f, f') = \mathrm{E}\left\{B(\nu, f)B^*(\nu', f')\right\}, \tag{3.11}$$

where $\mathrm{E}\{\cdot\}$ denotes the expectation over the ensemble of channel realizations and * denotes the complex conjugation operator. In general these ACFs depend on four arguments. With one of these ACFs and assuming a stochastic process as transmit signal, independent of the channel, the ACF of the output signal can be calculated, e.g., with the ACF of the IR

$$R_{yy}(t, t') = \int_{-\infty}^{\infty}\int_{-\infty}^{\infty} R_{xx}(t - \tau, t' - \tau')R_h(t, t'; \tau, \tau')d\tau d\tau'. \tag{3.12}$$

The four ACFs are related via two-dimensional Fourier transform, as depicted in Fig. 3.3

The WSSUS Model

Since the ACFs depend on four arguments they are rather difficult to estimate and handle, in order to characterize the radio channel. Simplifications of the ACF are possible with further statistical assumptions of the channel. Popular assumptions for the radio channel are the WSS and the US assumptions that yield much simpler ACFs.

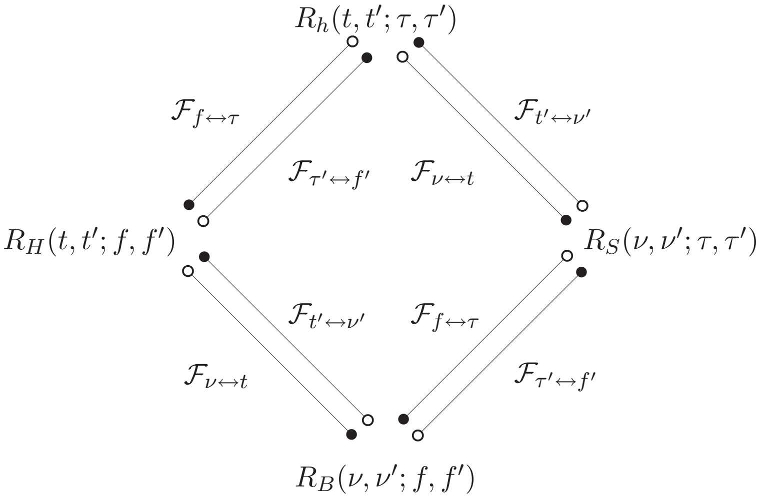

Figure 3.3: Relation between the ACFs, [59]

Wide-Sense Stationarity: A radio channel is called WSS, if its first and second order statistics do not change over time, i.e., the mean of the realization stays constant over time and the ACF does not depend on the absolute time, but only on the time separation $\Delta t = t - t'$. The ACF of the time-variant IR becomes

$$R_h(t,t';\tau,\tau') = R_h(\Delta t;\tau,\tau'). \tag{3.13}$$

Since the time domain is related to the Doppler domain via the two-dimensional Fourier transform, the WSS assumption also has influence on the ACF of the spreading function that simplifies to

$$R_S(\nu,\nu';\tau,\tau') = \widetilde{\widetilde{P_S}}(\nu;\tau,\tau')\delta(\Delta\nu), \tag{3.14}$$

where $\Delta\nu = \nu - \nu'$. This means that MPCs having different Doppler shifts are uncorrelated. Further the ACF of the Doppler-variant TF can be rewritten as

$$R_B(\nu,\nu';f,f') = P_B(\nu;f,f')\delta(\Delta\nu). \tag{3.15}$$

Uncorrelated Scatterers: US channels are the duality of WSS channels, but in the frequency domain. For these channels, MPCs arriving at different delays are uncorrelated. In this case the ACF of the time-variant TF can be simplified to

$$R_H(t,t';f,f') = R_H(t,t';\Delta f), \tag{3.16}$$

where $\Delta f = f - f'$. For the ACFs depending on the delay domain this means following simplifications

$$R_h(t,t';\tau,\tau') = P_h(t,t';\tau)\delta(\Delta\tau) \tag{3.17}$$

and

$$R_S(\nu,\nu';\tau,\tau') = \widetilde{P_S}(\nu,\nu';\tau)\delta(\Delta\tau), \tag{3.18}$$

where $\Delta\tau = \tau - \tau'$.

WSSUS Assumption: A further simplification can be achieved, if the WSS assumption and the US assumption are combined. In this case the first and second order statistics are time-invariant and frequency-invariant. This means that MPCs with different delays are uncorrelated *and* contributions with different Doppler shift are uncorrelated. The four-dimensional ACFs can then be simplified to the following set of equations

$$R_h(t, t'; \tau, \tau') = \delta(\Delta\tau) P_h(\Delta t; \tau), \tag{3.19}$$

$$R_H(t, t'; f, f') = R_H(\Delta t, \Delta f), \tag{3.20}$$

$$R_S(\nu, \nu'; \tau, \tau') = \delta(\Delta\nu)\delta(\Delta\tau) P_S(\nu; \tau), \text{and} \tag{3.21}$$

$$R_B(\nu, \nu'; f, f') = \delta(\Delta\nu) P_B(\nu; \Delta f). \tag{3.22}$$

The functions on the right hand side are two-dimensional, which is a major simplification. Since this functions are very important they were named in [65]

- $P_h(\Delta t; \tau)$: delay cross power spectral density
- $R_H(\Delta t, \Delta f)$: time frequency correlation function
- $P_S(\nu; \tau)$: scattering function
- $P_B(\nu; \Delta f)$: Doppler cross power spectral density

Of special interest is the scattering function $P_S(\nu; \tau)$ that is only non-zero for $\nu = \nu'$ and $\tau = \tau'$. It can be interpreted as the power that is arriving with Doppler shift ν and delay τ. The WSSUS assumption is not always fulfilled. Most notably radio channels for vehicular communications tend to be non-WSSUS, which is discussed in the following section.

Non-WSSUS / Quasi-WSSUS Channels

Unfortunately, the WSS and the US assumptions are rarely fulfilled in real-world radio channels, especially for vehicular radio communications channels. In order to fulfill the WSSUS assumption it would require that the first and second order statistics of the radio channel do not change over infinite time and frequency intervals. On the one hand, the statistics of the radio channel change over time (non-WSS) and, on the other hand, the MPCs at different delays can be correlated (non-US) due to interactions with large objects, e.g., buildings, bridges, and vehicles. For this reason the concept of quasi-WSSUS was firstly introduced in [59]. In this case the statistics of the radio channel do not change within a specific time and frequency window and therefore the simplifications based on the WSSUS assumption can be used within this window.

A more general concept for non-WSSUS is introduced in [15] and [66]. There the LSF $\mathcal{P}_S(t,f;\tau,\nu)$ is defined as an extension of the scattering function $P_S(\nu;\tau)$ to the non-WSSUS case. In the case of a non-WSSUS radio channel the time-variant TF $H(t,f)$ is nonstationary and therefore its power spectral density, the scattering function, is not defined. For this reason the LSF is defined, which can be interpreted as a time-frequency dependent scattering function. The LSF can be calculated by a two-dimensional Fourier transform of the ACF of the time-variant IR

$$\mathcal{P}_S(t,f;\tau,\nu) = \int_{-\infty}^{\infty}\int_{-\infty}^{\infty} R_h(t,\tau;\Delta t,\Delta\tau)\mathrm{e}^{-\mathrm{j}2\pi(\nu\Delta t+f\Delta\tau)}\mathrm{d}\Delta t\,\mathrm{d}\Delta\tau\,. \tag{3.23}$$

Note that this definition is consistent with the WSSUS case, where we have $\mathcal{P}_S(t,f;\tau,\nu) = P_S(\nu;\tau)$.
As explained in [15] the LSF is not guaranteed to be non-negative and furthermore depends on the whole correlation function $R_h(t,\tau;\Delta t,\Delta\tau)$. Therefore, [15] additionally defines a generalized LSF based on R linear time-variant prototype filters $\boldsymbol{G}_r$ whose TF $H_{\boldsymbol{G}_r}(t,f)$ is smooth and localized about the origin of the time-frequency plane. This means $\boldsymbol{G}_r$ amounts to a temporally localized low-pass filter.

The Generalized Local Scattering Function (GLSF) is defined as

$$\widetilde{\mathcal{P}_S}(t,f;\tau,\nu) = \mathrm{E}\left\{\sum_{r=0}^{R-1}\gamma_r\left|\mathcal{H}^{(\boldsymbol{G}_r)}(t,f;\tau,\nu)\right|^2\right\}, \tag{3.24}$$

where

$$\mathcal{H}^{(\boldsymbol{G}_r)}(t,f;\tau,\nu) = \mathrm{e}^{\mathrm{j}2\pi f\tau}\int_{-\infty}^{\infty}\int_{-\infty}^{\infty} H(t',f')H^*_{\boldsymbol{G}_r}(t'-t,f'-f)\mathrm{e}^{-\mathrm{j}2\pi(\nu t'-\tau f')}\mathrm{d}t'\mathrm{d}f' \tag{3.25}$$

and the coefficients γ_r need to fulfill

$$\sum_{r=0}^{R-1}\gamma_r = 1\,. \tag{3.26}$$

From (3.25) we see that the generalized LSF can be interpreted as the expectation of a multi-window spectrogram [67, 68] of the channel. This interpretation allows to define a practical estimation method [66] which I use for the evaluation of the vehicular channel measurements in Ch. 5.

In duality to the WSSUS case, where a ACF of the time-variant TF $R_H(\Delta t,\Delta f)$ is defined via a Fourier transform of the scattering function $P_S(\nu;\tau)$ a novel ACF for non-WSSUS channels is introduced in [66]

$$\mathcal{R}_h(\Delta t,\Delta f;\Delta\tau,\Delta\nu) = \int_{-\infty}^{\infty}\int_{-\infty}^{\infty} R_H(t,f;\Delta t,\Delta f)\mathrm{e}^{-\mathrm{j}2\pi(t\Delta\nu-f\Delta\tau)}\mathrm{d}t\,\mathrm{d}f\,. \tag{3.27}$$

If the channel fulfills the WSSUS assumption, the scatterers with different delays ($\Delta\tau \neq 0$) or different Doppler shifts ($\Delta\nu \neq 0$) are uncorrelated, i.e., $\mathcal{R}_h(\Delta t,\Delta f;\Delta\tau,\Delta\nu) =$

$R_H(\Delta t, \Delta f)\delta(\Delta\tau)\delta(\Delta\nu)$. Further the ACF for non-WSSUS channels can be calculated via a four-dimensional Fourier transform of the LSF

$$\mathcal{R}_h(\Delta t, \Delta f; \Delta\tau, \Delta\nu) = \int_{\mathbb{R}^4} \mathcal{P}_S(t, f; \tau, \nu) \mathrm{e}^{-\mathrm{j}2\pi(t\Delta\nu - f\Delta\tau + \tau\Delta f - \nu\Delta t)} \mathrm{d}t\, \mathrm{d}f\ \mathrm{d}\tau\, \mathrm{d}\nu\,. \tag{3.28}$$

3.2.3 Condensed Parameters

One important measure characterizing multipath propagation is the Root Mean Square (RMS) delay spread. For the definition of the delay spread, we need the time-varying Power-Delay Profile (PDP) $P_{\mathrm{PDP}}(t, \tau)$. The PDP is defined for time t_0 as the expectation of the squared magnitude of the complex IR

$$P_{\mathrm{PDP}}(\tau)|_{t_0} = \mathrm{E}\left\{|h(t_0, \tau)|^2\right\}. \tag{3.29}$$

In Sec. 5.3 I define an estimator for the PDP. The expectation in Eq. 3.29 is estimated by an averaging over a time interval, where the channel can be assumed as WSS. This estimation is called APDP. The RMS delay spread is the second central moment of the PDP [4]

$$\tau_{\mathrm{RMS}} = \sqrt{\frac{\int_0^\infty P_{\mathrm{PDP}}(\tau)\tau^2 d\tau}{\int_0^\infty P_{\mathrm{PDP}}(\tau) d\tau} - \bar{\tau}^2}, \tag{3.30}$$

where $\bar{\tau}$ is the mean delay

$$\bar{\tau} = \frac{\int_0^\infty P_{\mathrm{PDP}}(\tau)\tau d\tau}{\int_0^\infty P_{\mathrm{PDP}}(\tau) d\tau}. \tag{3.31}$$

In OFDM systems, like IEEE 802.11p for vehicular communications, the delay spread dictates the required length of the cyclic prefix if Inter Carrier Interference (ICC) needs to be avoided. Since the delay dispersion is equivalent to frequency selectivity, there also exists a related measure to τ_{RMS} in the frequency domain — the coherence bandwidth B_{coh}. It can be obtained from the frequency correlation function. The coherence bandwidth is bounded by [69],

$$B_{\mathrm{coh}} \gtrsim \frac{1}{2\pi\tau_{\mathrm{RMS}}}. \tag{3.32}$$

The coherence bandwidth is the frequency separation, where the correlation coefficient falls below 0.5.

Analogue to the delay spread in the case of multipath propagation, the Doppler spread is an important measure for the time selectivity of the radio channel. The integrated power in the Doppler domain is

$$P_{\mathrm{B,m}} = \int_{-\infty}^{\infty} P_B(\nu) d\nu, \tag{3.33}$$

where $P_B(\nu)$ is the Doppler cross power spectral density, see Sec. 3.2.2. The RMS Doppler spread is the second central moment of the integrated power [4]

$$\nu_{\mathrm{RMS}} = \sqrt{\frac{\int_{-\infty}^\infty P_B(\nu)\nu^2 d\nu}{P_{\mathrm{B,m}}} - \bar{\nu}^2}, \tag{3.34}$$

where $\bar{\nu}$ is the mean Doppler

$$\bar{\nu} = \frac{\int_{-\infty}^{\infty} P_B(\nu)\nu d\nu}{P_{\mathrm{B,m}}}. \tag{3.35}$$

Similar to the related measures in the delay domain (RMS delay spread) and frequency domain (coherence bandwidth), there also exists a related measure to the RMS Doppler spread in the time domain, the coherence time. It is estimated by the inequality, [69],

$$T_{\mathrm{coh}} \gtrsim \frac{1}{2\pi\nu_{\mathrm{RMS}}}. \tag{3.36}$$

The coherence time describes the time interval, where the correlation coefficient remains above 0.5.

4

Vehicular Measurement Campaigns

FOR the evaluation of vehicular communications in real-world scenarios, three vehicular measurement campaigns were carried out. In two of the measurement campaigns the radio channel was investigated. The first radio channel measurement campaign was carried out in 2007, in Lund, Sweden, and is called LUND'07. The second radio channel measurement campaign, with improved vehicular antennas, specific safety-related ITS application scenarios, and improved parameter settings, was conducted in the year 2009 also in Lund, Sweden, and is called DRIVEWAY'09, where DRIVEWAY stands for "**dir**ectional h**i**gh-speed channel characterization for **ve**hicular **w**ireless **a**ccess s**y**stems". With the third measurement campaign we investigated the V2I performance of the IEEE 802.11p PHY. This measurement campaign was part of the project REALSAFE, see [70].

In Sec. 4.1 the channel sounder for both radio channel measurement campaigns is described. Next the measurement parameter setup, the measurement equipment, the measurement scenarios, and the measurement practice for the LUND'07 and DRIVEWAY'09 campaign are described. Section 4.2 documents the measurement setup, equipment, and scenarios for the V2I performance measurement campaign.

4.1 Vehicular Radio Channel Measurement Campaigns

4.1.1 Channel Sounder

The measurements were carried out with the RUSK LUND channel sounder, manufactured by the company MEDAV, [71], that performs MIMO measurements based on the "switched-array" principle [72]. The transmitted signal is generated in the frequency domain, based on a broadband periodic multi-frequency excitation, OFDM-like, in order to guarantee a pre-defined spectrum over the whole bandwidth. The phases of each subcarrier are optimized, in order to minimize the *crest factor* (peak-to-average power ratio) which ensures a low distortion level in the amplifier and modulator circuits.

The transfer function of the channel $H(t, f)$ is calculated in the frequency domain from the received signal spectrum $Y(t, f)$ with

$$H(t,f) = \frac{Y(t,f)}{\hat{X}(t,f)}, \tag{4.1}$$

where $\hat{X}(t, f)$ is the excitation signal reference spectrum. It is measured by a back-to-back calibration procedure before the channel measurements, where the radio channel is replaced by an attenuator connected between the Tx and the Rx. This has the main advandage that the Tx- and Rx-frequency responses and the non-linear distortion of the Tx power amplifier are excluded from the channel TF $H(t, f)$. The Tx and Rx are synchronized via Rubidium clocks for accurate frequency synchronism and a defined time-reference. A block diagram of this channel sounder is depicted in Fig. 4.1.

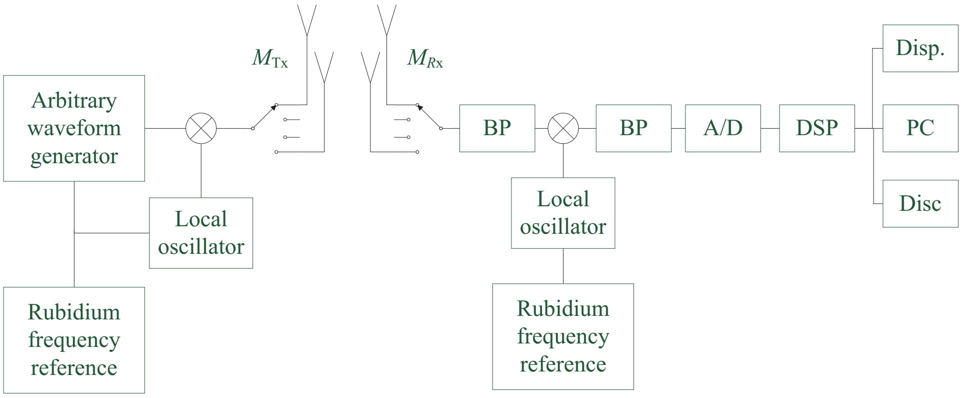

Figure 4.1: Block diagram of the RUSK LUND channel sounder

For channel sounding of non-WSSUS channels as described in Sec. 3.2.2 it has to be ensured that the channel is *underspread*. The radio channel is underspread, when the two-dimensional Nyquist criterion is fulfilled [15]

$$2\nu_{\max}\tau_{\max} \leq 1. \tag{4.2}$$

This criterion can be derived from the two following inequalities. Firstly the repetition time of the sounding signal t_{rep} must be shorter than the coherence time of the channel, i.e., the channel is not changing during the repetition time, which can be described by

$$t_{\mathrm{rep}} \leq \frac{1}{2\nu_{\mathrm{max}}}. \tag{4.3}$$

The repetition time is in the case of a Single-Input Single-Output (SISO) system simply the test signal length of the channel sounder $\tau_{\mathrm{max,\,CS}}$ plus a possible guard interval. For MIMO systems, the repetition time is the time interval over all measured single antenna links plus possible guard intervals. This time interval for the switched-array principle of the RUSK LUND channel sounder for our specific parameter settings is given in the end of this section. Secondly, it has to be ensured that consecutive sounding signals are not overlapping, i.e., that the repetition time of the sounding signal is longer than the maximum delay of the channel

$$t_{\mathrm{rep}} \geq \tau_{\mathrm{max}}. \tag{4.4}$$

Combining these two inequalities (Eq. (4.3) and Eq. (4.4)), Eq. (4.2) is yielded.

In our measurements, the maximum delay of significant signal contributions is approx. $2\,\mu$s and the maximum Doppler shift of significant contributions is approx. 2 kHz. These channel parameters fulfill the two-dimensional Nyquist criterion, Eq. (4.2), $2 \cdot 2\,\mu\mathrm{s} \cdot 2\,\mathrm{kHz} = 4 \cdot 10^{-3} \leq 1$. This means that our measured vehicular radio channels can be considered as underspread.

After the sounding signal is designed in the frequency domain, it is stored and periodically transmitted. At the receiver the signal is Band Pass (BP)-filtered, down-converted to an intermediate frequency of 160 MHz, demodulated, and sampled at 640 MHz. Subsequently the time-domain data is converted by a Fast Fourier Transform (FFT) to the frequency domain in the Digital Signal Processing (DSP) block.

For our measurements we used a measurement bandwidth of 240 MHz, which results in an intrinsic delay resolution of $\Delta\tau = 4.2$ ns. The test signal length was set to $\tau_{\mathrm{max,\,CS}} = 3.2\,\mu$s, which corresponds to a maximum propagation path length of 959 m. For the measurements we used the maximum Tx power of the channel sounder of 27 dBm. Our MIMO configuration consists of $M_{\mathrm{Tx}} = 4$ antenna elements at the Tx and $M_{\mathrm{Rx}} = 4$ antenna elements at the Rx. In the LUND'07, see Sec. 4.1.2, measurement campaign we always used the 4×4 MIMO configuration, whereas in the DRIVEWAY'09, see Sec. 4.1.3, measurement campaign we were measuring also in a SISO configuration, additionally to the 4×4 MIMO setup, in order to sample the channel faster. One of the most important goals of our measurements is to achieve a high resolvable maximum Doppler shift, i.e., we have to choose the snapshot repetition time t_{rep} properly.

The snapshot time, t_{snap}, i.e., the time over all $P = M_{\mathrm{Tx}} \times M_{\mathrm{Rx}} = 16$ temporal multiplexed channels, is equal to $2 \times P \times \tau_{\mathrm{max,\,CS}} = 2 \times 16 \times 3.2\,\mu\mathrm{s} = 102.4\,\mu\mathrm{s}$ (in the

Table 4.1: Measurement configuration parameters

Measurement bandwidth, BW	240 MHz
Delay resolution, $\Delta\tau = 1/BW$	4.2 ns
Frequency spacing, Δf	312.5 kHz
Transmit power, P_{Tx}	27 dBm
Test signal length, $\tau_{\mathrm{max,\ CS}}$	3.2 μs
Number of samples in frequency domain, N_f	769

case of the 4 × 4 MIMO configuration), where the factor 2 stems from the guard interval between consecutive snapshots used by the sounder.

The number of frequency bins over 240 MHz is 769 that results in a frequency spacing of $\Delta f = 312.5$ kHz. The output of the channel sounder is the discrete time-variant transfer function

$$H[k, q, p] = H(kt_{\mathrm{rep}}, q\Delta f, p). \tag{4.5}$$

Tab. 4.1 gives an overview of the main measurement parameters that are used in both radio channel measurement campaigns.

4.1.2 Measurement Campaign: LUND'07

This measurement campaign was carried out during April 16th - 20th 2007, in Lund, Sweden. A description of the measurement campaign can also be found in [73]. In the following sections I describe the specific measurement setup, the equipment, the chosen scenarios, and the measurement practice.

Measurement Parameter Setup

In this measurement campaign we used a center frequency of 5.2 GHz. The reason for this center frequency was the availability of readily calibrated antenna arrays at this time. This band is close enough to the 5.9 GHz band such that no significant differences in propagation characteristics are anticipated. To obtain feasible file sizes, but still allow for sufficient measurement time and high Doppler resolution, we set the snapshot repetition rate to $t_{\mathrm{rep}} = 307.2\,\mu$s. Using $N_t = 32500$ snapshots, we could continuously measure for 9.984 s (that will be called a 10 s measurement run in the following) recording a file of 1 GB for each measurement. The maximum Doppler shift for a time-variant channel is

$$\nu_{\mathrm{max}} = \frac{1}{2 \cdot t_{\mathrm{rep}}}. \tag{4.6}$$

With these settings, the maximum resolvable Doppler shift is equal to 1.6 kHz, which corresponds to a maximum speed of 338 km/h. The resulting TF, see Eq. (4.5), of the channel sounder has than an overall array size of $32500 \times 769 \times 16$ ($N_t \times N_f \times P$). Additional

Table 4.2: LUND'07 measurement configuration parameters

Center frequency, f_c	5.2 GHz
Measurement band	5.080 GHz - 5.320 GHz
Number of Tx antenna elements, M_{Tx}	4
Number of Rx antenna elements, M_{Rx}	4
Snapshot time, t_{snap}	102.4 μs
Snapshot repetition rate, t_{rep}	307.2 μs
Number of snapshots in time, N_t	32500
Recording time, t_{rec}	9.984 s
File size, FS	1 GB

to the main settings summarized in Tab. 4.1 the specific parameter settings of the LUND'07 campaign are shown in Tab. 4.2.

Measurement Equipment

Antennas: On both link ends we used elements from uniform cylindric arrays of microstrip antennas. Figure 4.2 shows the two antenna arrays. Each array consists of a cylindric geometry (the Rx array consists of 4 layers) of 16 dual-polarized elements, from which we selected 4 symmetrically placed, vertically polarized elements. With the reference bearing 0° (as seen from a top view of the arrays) being in the direction of driving, the selected antenna elements were directed at 45°, 135°, 225°, and 315°. The directions of the main lobes of these elements were the same for both measurement vehicles and are described in Fig. 4.3. The gain with respect to the isotropically radiated power of the Tx and Rx aggregated antenna pattern at 5.2 GHz is $G_{\mathrm{Tx,iso}} = G_{\mathrm{Rx,iso}} = 1.29$ (= 1.1 dBi).

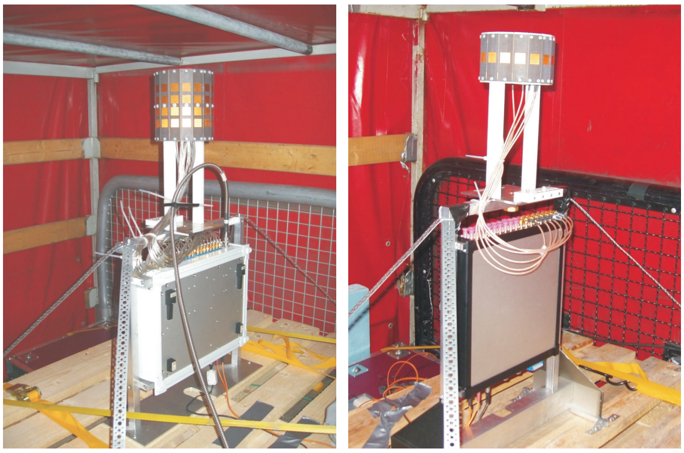
(a) (b)

Figure 4.2: (a) Rx antenna arrays and (b) Tx antenna array

Each antenna array was mounted on top of a stack of Euro pallets, which, when mounted on the vehicle's platform, provided a total antenna height of 2.4 m above the ground, see Fig. 4.4. Table 4.3 presents the allocation of the single antenna element link numbers to the antenna elements.

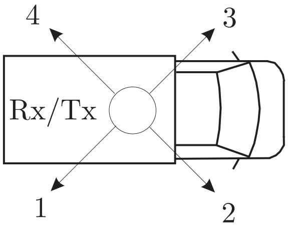

Figure 4.3: Direction of the main lobes of each antenna element for Rx and Tx

Table 4.3: Allocation between antenna elements and antenna element link numbers

Rx element	**Tx element**	**Antenna element link number**
1	1	1
2	1	2
3	1	3
4	1	4
1	2	5
2	2	6
3	2	7
4	2	8
1	3	9
2	3	10
3	3	11
4	3	12
1	4	13
2	4	14
3	4	15
4	4	16

Route Documentation: To document the routes and scenarios during the measurements (traffic, weather, environment) we used two video cameras. Each camera was equipped with a fisheye lens, in order to capture a field of view of about 150°. One camera was placed in the passenger compartment of the vehicle containing the Tx. The other camera was mounted in the back of the Rx transporter, where the vehicle's tarpaulin was opened at the back.

Global Positioning System (GPS) position data was directly available from the Tx and

(a) (b)

Figure 4.4: Loading spaces with the measurement equipment, (a) Rx and (b) Tx

Figure 4.5: Laser distance meter and video camera for documentation

Rx of the channel sounder at a rate of one position sample per second. Moreover, we used one additional GPS system in order to record the actual speed of the Tx vehicle. This GPS system also provided a real-time display of the actual vehicle position.

In order to obtain a more accurate measurement of the distance between the vehicles, we also used a laser distance meter LD90-3100HS from Riegl Laser Measurement Systems GmbH, [74]. It was programmed such that it supplied the actual distance every 100 ms (and in some measurements every 200 ms). Figure 4.5 shows the laser distance meter and one of the video cameras, which were mounted together on a monopod.

Vehicles: As measurement vehicles, we used two Volkswagen LT35 transporters (similar to pickup trucks), which are depicted in Fig. 4.6. The loading platform of the transporters were covered with a plastic tarpaulin to protect the measurement equipment and antennas against air stream and rain, thus providing greater stability for the antennas. Since the height of the tarpaulin cover is larger than the driver's cabin, the antennas were mounted on the loading platform in such a way that they could "see" over the driver's cabin (though

Figure 4.6: Measurement vehicle

(a) (b) (c)

Figure 4.7: Satellite photo of (a) the rural scenario in the north-east of Lund, (b) the highway E22 in the east of Lund, (c) the urban scenario with the measurement route on the street "Esplanaden" in the center of Lund (source: [75])

we cannot exclude the possibility that waves reflected from the road, and thus arriving from an elevation angle smaller than 0 degree, might have been attenuated by the driver's cabin). Figure 4.4 presents the measurement vehicles containing the channel sounders, batteries, and antennas placed on the loading space (battery lifetime of the Rx equipment was extended by means of a petrol-driven power generator, which was also mounted on the loading space).

Measurement Scenarios

Three different scenarios, rural, highway, and urban, were measured. Satellite photographs of the scenarios are depicted in Fig. 4.7.

In each scenario we carried out two kinds of V2V measurements: with the two measurement vehicles driving in (i) the same, and (ii) opposite directions. Vehicle speed and the distance between the vehicles was varied between different measurement runs in the range of $30 - 110\,\text{km/h}$ and $30 - 130\,\text{m}$, respectively. In the highway scenario, we also carried out V2I measurements, where the Tx was placed on a bridge above the road.

Measurement Practice

The measurement campaign was conducted during three days, and a total of 141 measurement runs were recorded.

In the Rx vehicle, one person acted as driver, a second colleague controlled the channel sounder, and the third colleague wrote the measurement protocol. The Tx vehicle was steered by one driver, another person controlled the additional GPS-system and the laser distance meter with a laptop. The third person was responsible for the video documentation and pointing the laser distance meter onto the Rx vehicle using a telescope.

The laser distance meter was only used for V2V measurements in same direction. In this case the Tx vehicle followed the Rx vehicle. Consequently it was also possible to hold approximately the same distance between the vehicles during the measurement runs. Communication between the two vehicles was handled through walkie-talkies operating at a frequency of 446 MHz.

4.1.3 Measurement Campaign: DRIVEWAY'09

Until 2009 there was a lack of application specific radio channel measurements in several aspects, see [14]. First, most measurements conducted so far have been done with the Tx and Rx cars driving either in convoy, or in opposite, parallel directions. The results of such investigations do not necessarily apply to many safety-critical V2V applications, e.g., [42],

- collision avoidance,
- emergency vehicle warning,
- hazardous location notification,
- wrong-way driving warning,
- co-operative merging assistance,
- traffic condition warning,
- slow vehicle warning, or
- lane change assistance.

Secondly, few measurements have been conducted with an antenna mounting that is realistic from a car manufacturers point of view. Usually a “regular” antenna array was mounted in an elevated position. Third, the impact of vehicles obstructing the direct path between Tx and Rx as well as the possible gains of using multiple antenna elements at Tx and/or Rx has been little explored.

Table 4.4: DRIVEWAY'09 measurement configuration parameters

Parameter setup	**1**	**2**	**3**	**4**
Center frequency, f_c	5.6 GHz			
Measurement band	5.480 - 5.720 GHz			
Number of Tx antenna elements, M_{Tx}	4	4	4	1
Number of Rx antenna elements, M_{Rx}	4	4	4	1
Snapshot time, t_{snap}	102.4 μs	102.4 μs	102.4 μs	6.4 μs
Snapshot repetition rate, t_{rep}	307.2 μs	102.4 μs	921.6 μs	6.4 μs
Number of snapshots in time, N_t	32500			
Recording time, t_{rec}	9.984 s	3.328 s	29.952 s	0.208 s
File size, FS	1 GB			

In order to address these issues, and perform a realistic characterization of propagation channels for safety-related ITS applications a follow-up measurement campaign to LUND'07, called DRIVEWAY'09, was conducted in June 2009. The key features of the measurements are the following:

- Measurements performed in traffic situations that are of particular interest for safety-related ITS applications, such as intersections, traffic congestion and merge lanes, see [42, 43, 50]
- Realistic antennas, especially designed for vehicular usage and realistic antenna mounting
- Investigation of important propagation mechanism such as LOS obstruction
- Investigation of multiantenna benefits

An overview of the DRIVEWAY'09 channel measurement campaign can also be found in [12].

Measurement Parameter Setup

As in the LUND'07 measurement campaign we used the RUSK LUND channel sounder, see Sec. 4.1.1 for description.

Figure 4.8: DRIVEWAY'09 logo

We were measuring with a bandwidth of $BW = 240\,\text{MHz}$ at a center frequency of $f_\text{c} = 5.6\,\text{GHz}$. This center frequency was the highest allowed by the channel sounder and considered close enough to the allocated 5.9 GHz frequency band for ITS in Europe for no significant differences to be expected. The Tx power was set to $P_\text{Tx} = 27\,\text{dBm}$, and the adjustable test signal length $\tau_\text{max, CS} = 3.2\,\mu\text{s}$. The temporal sampling as well as time duration of the measurements were set for different measurements depending on specific conditions such as (Tx/Rx) car speed and are summarized in Tab. 4.4.

The vast majority of the measurements were 4×4 MIMO measurements. However, since the allowable sample rate of a switched-array system depends on the number of measured links, we also carried out a number of SISO measurements in order to sample the radio channel as fast as possible. The corresponding maximum resolvable Doppler shifts can be calculated with Eq. (4.6) and range from 543 Hz for parameter setup 3 (MIMO) to 78 kHz for parameter setup 4 (SISO), respectively.

Measurement Equipment

Antennas: Application-specific antenna modules were designed, [31], and integrated into the conventional mounting position for roof-top antennas on the rear part of the vehicles that we used (custom Volkswagen Tourans), see Fig. 4.9. Identical antenna modules were used for the Tx and Rx cars. Each antenna module consists of a four-element Uniform Linear Array (ULA) with an interelement spacing of $\lambda/2$, see Fig. 4.10. The array consists of circular patch antennas that are excited in a higher-operational mode yielding terrestrial beam patterns with vertical polarization. To enable (future) directional estimation of the measurement data, the ULA orientation was chosen perpendicular to driving direction (thus implying a 90° rotation of the conventional antenna housing). Calibrated in-situ antenna measurements were taken in a large automated antenna measurement facility, see Fig. 4.11. Table 4.5 presents the allocation of the antenna element link numbers to the antenna elements.

Figure 4.9: The conventional antenna housing of a Volkswagen Touran

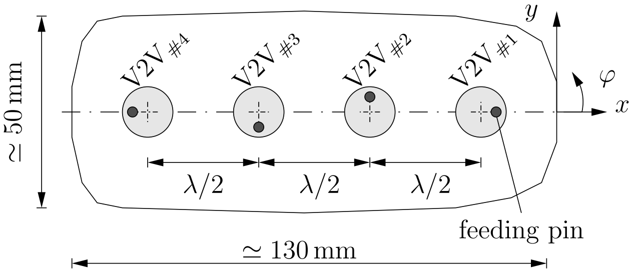

Figure 4.10: Block diagram of the ULA. The driving direction is along the y-axis


(a)

(b)

Figure 4.11: Delphi antenna calibration facility in Bad Salzdetfurth, (a) outside and (b) inside

Table 4.5: Allocation between antenna elements and antenna element link numbers

Rx element	**Tx element**	**Antenna element link number**
4	1	1
3	1	2
2	1	3
1	1	4
4	2	5
3	2	6
2	2	7
1	2	8
4	3	9
3	3	10
2	3	11
1	3	12
4	4	13
3	4	14
2	4	15
1	4	16

Route Documentation: For the documentation of the traffic and environment during the measurement runs, videos were taken with two digital compact cameras. Both were orientated to the front of the Tx and Rx vehicle, respectively. Additionally, notes of important events were written down. The coordinates of the routes during the measurements were logged with GPS receivers at the Tx and Rx vehicle that were connected directly to the channel sounder. Unfortunately the GPS receiver in the Rx vehicle was not working correctly and therefore the GPS data of the Rx from almost all of the measurement runs is missing.

Vehicles: As measurement vehicles we used two similar custom Volkswagen Touran, see Fig. 4.12 (a). Figure 4.12 (b) shows the Rx unit of the channel sounder packed into the trunk of the car. The height of the vehicles, which is also the height of the mounting position of the antennas, is 1.73 m.

Measurement Scenarios

The following scenarios of importance for safety-related ITS applications were measured:

- **Road crossings**: A specific feature of road crossings is that the LOS contribution of the radio signal between two cars approaching it (from perpendicular directions) may be obstructed for long durations. Thus, the reliability of a V2V link depends on the availability of other propagation paths, such as reflections from nearby buildings.

(a) (b)

Figure 4.12: (a) Measurement vehicle and (b) Rx vehicle equipped with the channel sounder

To investigate the quality of such links and the importance of additional scatterers, we let the Tx and Rx cars approach four different four-way intersections from perpendicular directions:

- Open area intersection: This suburban scenario is characterized by little to no buildings next to intersecting roads. No severe LOS obstruction is expected but the traffic situation is busy.
- Obstructed LOS without surrounding buildings: The LOS path is blocked by a building until the cars meet in the intersection, but there are no buildings on the other sides of the intersection. There is no traffic, and we thus expect few additional scatterers to provide additional propagation paths.
- Obstructed LOS with surrounding buildings and single-lane streets: There are buildings and parked cars on all sides of the intersection; these are expected to provide additional propagation paths. There is little traffic and no traffic lights.
- Obstructed LOS with surrounding buildings and multi-lane streets: Similar to previous scenario, but with a larger intersection. There are traffic lights, busy traffic and each two-lane street has turn lanes (for left turns). Many additional propagation paths are expected, though their lifetime (visibility) may be short.

- **Merge lanes**: Similar to road crossings, an important aspect of this scenario is the possibility of an obstructed LOS path. These measurements were conducted with the Rx car driving on a highway whereas the Tx car was entering it from an entrance ramp.
- **Traffic congestion**: Traffic congestions are interesting due to their large number of involved vehicles, usually at low to zero speed. These radio links may thus be

subject to LOS obstruction. It is also of interest to find out how many of the available scatterers (vehicles) that actually contribute to the received signal. We performed measurements for different congestion situations, such as when both cars are stuck in one, when one car stuck in congestion is overtaken by the other one, or when one car is approaching congestion where the other car is stuck.

- **Tunnel**: Tunnels potentially provide rich scattering environments, and we thus expect a denser impulse response from these measurements that were conducted in the tunnel (following the Öresund bridge) between Denmark and Sweden. Both cars were driving in the same direction with different distances and a varying number of cars in between.

- **General LOS obstruction**: The goal of this scenario is to, in a controlled way, analyze the impact of an appearing/disappearing LOS path on the received signal. The measurements are conducted with both cars driving in the same direction on a highway, positioned such that trucks or other large vehicles are blocking the LOS during parts of each measurements.

Measurement Practice

In each measurement vehicle there was at least one person beside the driver for taking the videos and the documentation. For communication between the two vehicles cell phones and walky-talkies were used. In the case of the general LOS obstruction scenarios a third vehicle (a small truck) was rented, in order to be able to control the obstruction events between the two measurement vehicles. Ten to twenty measurement runs were made within each scenario, resulting in a total of about 140, which implies recording of more than 5 million MIMO impulse responses.

4.2 Vehicular PHY Measurement Campaign

4.2.1 Measurement Campaign: REALSAFE

These measurements were carried out for investigating the characteristics of the PHY of the draft IEEE 802.11p standard, also called WAVE, [76]. The draft standard IEEE 802.11p uses OFDM signaling with 48 data subcarriers within a 10 MHz bandwidth. In Fig. 4.13 the yellow arrows are pointing to the access points above the PHY on Tx and Rx side that are used in these measurements. The campaign was carried out in July 2009 on the highway A12 in Tyrol, Austria, within the REALSAFE project, [70].

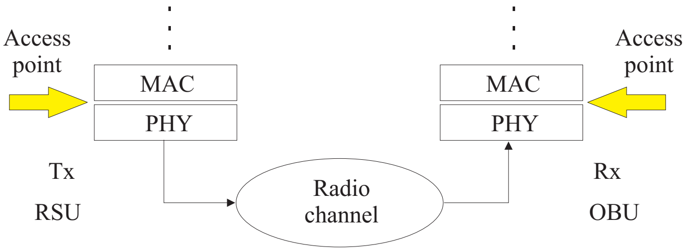

Figure 4.13: IEEE 802.11p measurements overview with RSU as Tx and OBU as Rx

Type of Measurements

In these measurements we filled the Medium Access Control Service Data Unit (MSDU) with data of a specific length, in the following simply called packet length N_{MSDU}. The MSDU is directly above the Medium Access Control Protocol Data Unit (MPDU). The measurements were taken without any MAC functions, i.e., no acknowledgments and no retransmissions were sent. This separate investigation of the PHY offered us the possibility to evaluate the strengths and weaknesses and possible improvements of the PHY protocol design, in order to get a robust V2I communication system in real-world scenarios. Figure 4.14 depicts the structure of the frames in the PHY and MAC layer. It can be seen that the MPDU frame, which is directly related with the MSDU frame, is extended with a header, padding bits, and training symbols on the PHY Convergence Procedure (PLCP). The resulting frame on the PHY Physical Medium Dependent (PMD) is called the OFDM frame, existing of 4 OFDM symbols for the PLCP preamble (2 symbols for the short preamble and 2 symbols for the long preamble), 1 OFDM symbol for signaling, and a variable number of OFDM symbols for data. The number of data OFDM symbols depends on the packet length N_{MSDU} and data rate (modulation scheme and coding rate) and is shown in Tabs. 4.7, 4.8, and 4.9 in the fourth column for each parameter setting. The PHY Sublayer Data Unit (PSDU) length in Byte is given by the packet length with

$$N_{\mathrm{PSDU}} = N_{\mathrm{MSDU}} + 38\,\mathrm{Byte}. \tag{4.7}$$

The number of OFDM symbols is defined by

$$N_{\mathrm{sym}} = \lceil (16 + 8N_{\mathrm{PSDU}} + 6)\,/N_{\mathrm{dbps}} \rceil\,, \tag{4.8}$$

where $\lceil \cdot \rceil$ denotes the smallest integer value greater than or equal to its argument and N_{dbps} is the number of data bits per OFDM symbol, see Tab. 4.6. The number of data bits in the whole OFDM frame is then given by

$$N_{\mathrm{data}} = N_{\mathrm{sym}} N_{\mathrm{dbps}}. \tag{4.9}$$

Table 4.6 shows the relation between data rate, modulation scheme, coding rate, and data bits per OFDM frame.

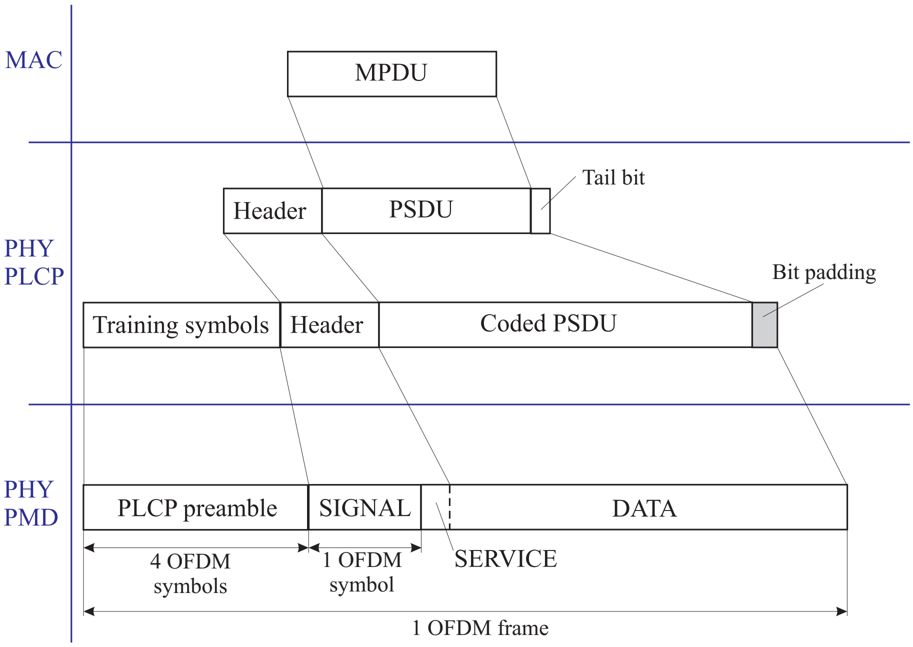

Figure 4.14: Schematic of MAC and PHY frame formats

Measurement Parameter Setup

For our measurements we used the 10 MHz frequency band centered at 5880 MHz. The impact of four different parameters was investigated:

- Tx-power (Equivalent Isotropically Radiated Power (EIRP)) of RSU
- Data rate (modulation scheme and coding rate)
- Packet length (MSDU length)
- Speed of the vehicle (OBU)

We carried out measurements with two different speeds of the OBU-vehicle, 80 km/h (low speed) and 120 km/h (high speed). The lower speed of 80 km/h was chosen, because of the traffic on the A12. It was not expected that it is possible to drive slower than 80 km/h, without constricting the usual traffic. We were always driving on the right lane with the lower speed. The higher speed of 120 km/h was chosen, in order to have a margin to the speed limit of 130 km/h on this part of the A12. With the higher speed, we were always driving on the left lane.

Parameter Setting I — Range Test: With Parameter setting I we investigated the impact of the Tx power. We chose a Tx power (EIRP) of 16 dBm and 7.5 dBm for the low RSU and 15.5 dBm and 10.5 dBm for the high RSU. The difference in the transmit power for the high RSU and the low RSU is coming from the different length of the Radio

Table 4.6: Rate-dependent parameters for IEEE 802.11p

Data rate [Mbit/s]	**Modulation**	**Coding rate**	**Coded bits per subcarrier** N_{bpsc}	**Coded bits per OFDM symbol** N_{cbps}	**Data bits per OFDM symbol** N_{dbps}
3	BPSK	1/2	1	48	24
4.5	BPSK	3/4	1	48	36
6	QPSK	1/2	2	96	48
9	QPSK	3/4	2	96	72
12	16-QAM	1/2	4	192	96
18	16-QAM	3/4	4	192	144
24	64-QAM	2/3	6	288	192
27	64-QAM	3/4	6	288	216

Frequency (RF) cables to the antennas and the non-linear behavior at the CVIS box power setting. There are two extreme-case settings for the data rate: the highest data rate of 27 Mbit/s, and lowest data rate of 3 Mbit/s. The speed of 80 km/h was chosen for this setting. The smallest packet length of 0 Byte leading to a packet length of 2 OFDM symbols was chosen, in order to get the maximum achievable distance, by using the lowest data rate of 3 Mbit/s and the highest power of 15.5 dBm (16 dBm). Table 4.7 summarizes the parameter settings.

Table 4.7: Parameter setting I for range test

Parameter setting	**Tx power low RSU / high RSU**	**Data rate**	**Packet length (number of OFDM symbols)**	**Speed**
PS 1.1	16 dBm / 15.5 dBm	27 Mbit/s	0 Byte (2)	80 km/h
PS 1.2	16 dBm / 15.5 dBm	3 Mbit/s	0 Byte (14)	80 km/h
PS 1.3	7.5 dBm / 10.5 dBm	27 Mbit/s	0 Byte (2)	80 km/h
PS 1.4	7.5 dBm / 10.5 dBm	3 Mbit/s	0 Byte (14)	80 km/h

Parameter Setting II — Packet Length Test: With Parameter setting II we investigated the impact of packet length, which results in a different number of OFDM symbols per frame. The higher Tx power is chosen, in order to have a larger coverage area. The data rate is fixed (extreme case at 3 Mbit/s) and both vehicle speeds were used. The first parameter setting (0 Byte, 80 km/h) is included in Parameter setting I. The five different parameter settings are summarized in Tab. 4.8.

Table 4.8: Parameter setting II for packet length test

Parameter setting	**Tx power low RSU / high RSU**	**Data rate**	**Packet length (number of OFDM symbols)**	**Speed**
PS 2.1	16 dBm / 15.5 dBm	3 Mbit/s	0 Byte (14)	120 km/h
PS 2.2	16 dBm / 15.5 dBm	3 Mbit/s	1554 Byte (532)	80 km/h
PS 2.3	16 dBm / 15.5 dBm	3 Mbit/s	1554 Byte (532)	120 km/h
PS 2.4	16 dBm / 15.5 dBm	3 Mbit/s	787 Byte (276)	80 km/h
PS 2.5	16 dBm / 15.5 dBm	3 Mbit/s	787 Byte (276)	120 km/h

Parameter Setting III — Modulation and Coding Scheme Test: With Parameter setting III we investigated the impact of different modulation and coding schemes at a reasonable packet length of 200 bytes at different speeds. Because of time limitation we measured only a subset of the parameter settings with the lower speed of 80 km/h. In Tab. 4.9 the different parameter settings can be found.

Table 4.9: Parameter setting III for modulation and coding scheme test

Parameter setting	**Tx power low RSU / high RSU**	**Data rate**	**Packet length (number of OFDM symbols)**	**Speed**
PS 3.1	16 dBm / 15.5 dBm	3 Mbit/s	200 Byte (81)	120 km/h
PS 3.2	16 dBm / 15.5 dBm	4.5 Mbit/s	200 Byte (54)	120 km/h
PS 3.3	16 dBm / 15.5 dBm	6 Mbit/s	200 Byte (41)	120 km/h
PS 3.4	16 dBm / 15.5 dBm	9 Mbit/s	200 Byte (27)	120 km/h
PS 3.5	16 dBm / 15.5 dBm	12 Mbit/s	200 Byte (21)	120 km/h
PS 3.6	16 dBm / 15.5 dBm	18 Mbit/s	200 Byte (14)	120 km/h
PS 3.7	16 dBm / 15.5 dBm	24 Mbit/s	200 Byte (11)	120 km/h
PS 3.8	16 dBm / 15.5 dBm	27 Mbit/s	200 Byte (9)	120 km/h
PS 3.9	16 dBm / 15.5 dBm	3 Mbit/s	200 Byte (81)	80 km/h
PS 3.11	16 dBm / 15.5 dBm	6 Mbit/s	200 Byte (41)	80 km/h
PS 3.12	16 dBm / 15.5 dBm	9 Mbit/s	200 Byte (27)	80 km/h
PS 3.13	16 dBm / 15.5 dBm	12 Mbit/s	200 Byte (21)	80 km/h

Measurement Equipment

Transceiver: For the RSU and the OBU a Peripheral Component Interconnect (PCI) card, developed by Q-FREE, [77], in the framework of the CVIS project, [48], was used. The PCI card (M5 Radio Module) is installed in a mobile applicable PC, in the following called CVIS PC. The M5 Radio Module is equipped with an Atheros chipset, implementing the draft standard IEEE 802.11p at 5.9 GHz. It is also equipped with a GPS receiver, in order to log the location of the OBU and give a global timestamp to both the OBU and

(a) (b)

Figure 4.15: (a) RSU installation and (b) OBU antenna

the RSUs. Figure 4.15 (a) shows the CVIS PC setup as RSU.

OBU Antenna: As OBU antenna, a vehicular antenna developed within the CVIS project was used. The beam pattern was specifically designed to provide omni-directional coverage with linear vertical polarization in azimuth including mutual coupling between individual antennas located in the same multistandard antenna compartment. Vehicular integration effects were not taken into account for beam pattern optimization. It was mounted with magnets on the rear part of the roof of the test vehicle in a height of 2 m. Figure 4.15 (b) shows the OBU antenna mounted on the test vehicle.

RSU Antenna: As RSU antenna we used a vertically polarized monopol with omnidirectional antenna pattern and a nominal antenna gain of 9 dBi. The antenna (V09/54) is from the company SMARTEQ, [78]. Figure 4.16 (a) shows the RSU antenna mounted at the lower position.

Test Vehicle: As test vehicle we used a Volkswagen Multivan provided by the Austrian roadoperator Autobahnen- und Schnellstraßen-Finanzierungs-AG (ASFINAG), [79], see Fig. 4.16 (b).

Documentation Equipment: As documentation equipment we used digital cameras. One camera was used in order to take videos in driving direction of the test vehicle, and a second camera was leading to the back of the vehicle during the measurements. Beside the video documentation, notes of important events during the measurement runs were taken.

(a) (b)

Figure 4.16: (a) RSU antenna and (b) test vehicle

Measurement Scenarios

Scenario 1 (high RSU): The first scenario is denoted as RSU 1 or “high RSU”, which refers to a numbering of the gantries in driving direction west and the antenna position, respectively. In this scenario the antenna is mounted on top of the gantry. The highway in the vicinity of the gantry is surrounded by trees in both directions. The middle strip that divides the lanes consists of a waist-high concrete wall followed by bushes of the same height. After a 250 m straight lane in both directions relative to the gantry position, the highway starts to bend to the right. This scenario is referred to as low scattering environment. Figure 4.17 (a) shows the high RSU gantry and the surrounding of the site. The view from the gantry and the course of the highway in direction west is illustrated by Fig. 4.17 (b).

The antenna is mounted on a top metal pillar close to the ladder which is shown by Fig. 4.18 (a). The antenna height is 7.1 m above the road level. A low loss RF cable connects the antenna with the CVIS PC which is placed in a weather protection box close to the gantry.

The gantry is located at highway kilometer 58.753. Figure 4.18 (b) shows an aerial photography of the location of the high RSU, which illustrates the bending of the lane at this part of the highway. This part of the highway follows the course of the river Inn and is surrounded by flat agriculture terrain. There are neither off-ramps nor bridges in the neighborhood of the gantry.

Scenario 2 (low RSU): The second scenario is denoted as RSU 2 or “low RSU”. The antenna is mounted next to the gantry on a snow protection wall. The antenna height is 1.8 m above the road level. The highway in the vicinity of the gantry is surrounded by noise protection walls in both directions. The middle strip consists of a waist-high concrete wall surrounded by green area. In direction east, the lane is straight whereas

(a) (b)

Figure 4.17: (a) High RSU gantry and vicinity and (b) view from the high RSU gantry in direction west

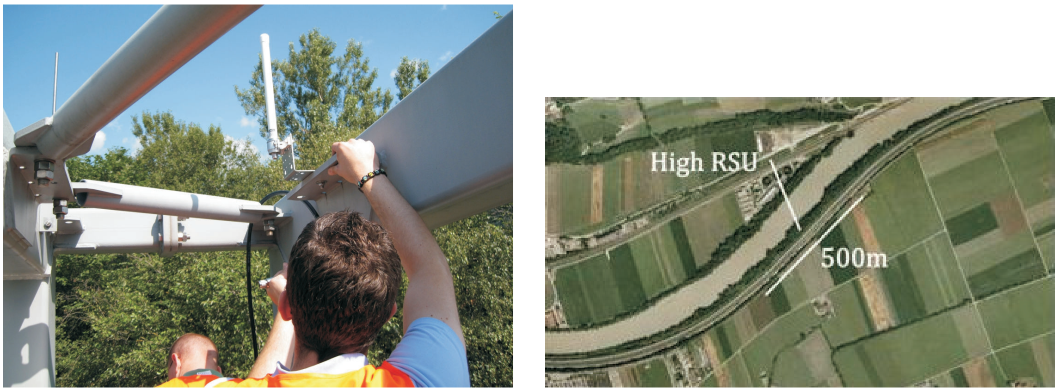

(a) (b)

Figure 4.18: (a) Mounting of the antenna and (b) satellite photo of the high RSU

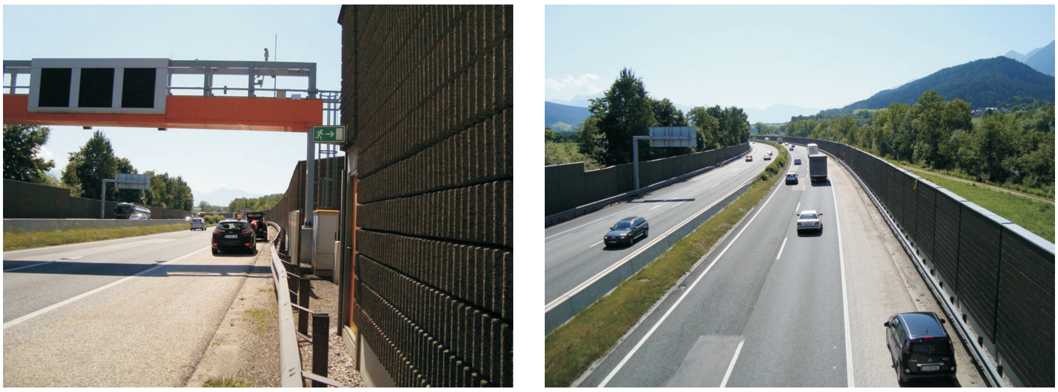

(a) (b)

Figure 4.19: (a) Low RSU gantry and vicinity and (b) view from the low RSU gantry in direction west

(a) (b)

Figure 4.20: (a) Mounting of the antenna and (b) satellite photo of the low RSU

in driving direction the highway follows a left turn. This scenario is referred to as rich scattering environment.

Figure 4.19 (a) shows the low RSU gantry and the snow protection wall next to the gantry pillar where the antenna is mounted. In Fig. 4.19 (b) the view from the top of the gantry in direction west, where the highway follows a slight left turn, is shown.

The setup of the measurement equipment is depicted in Fig. 4.20 (a). The antenna (left upper corner of the picture) is connected to the CVIS platform which is placed in a weather protection box next to the snow protection wall.

Figure 4.20 (b) shows an aerial photography of the location of the low RSU. Driving in direction east, there is an off-ramp to Wattens about 250 meters relative from the gantry position, followed by two bridges that cross the highway about 500 m and 800 m after passing the gantry.

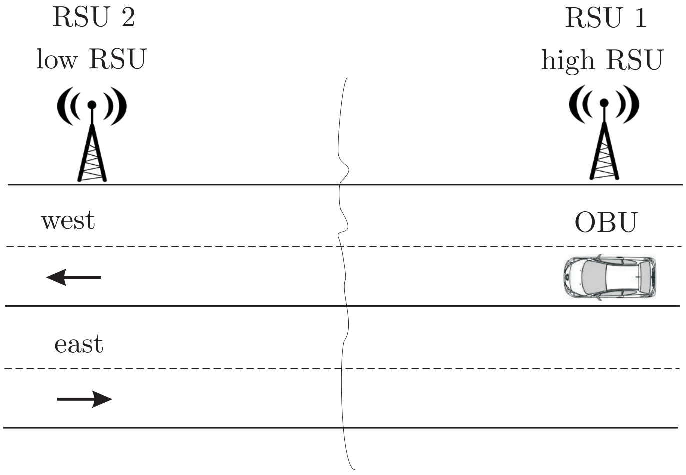

Figure 4.21: Schematic scenario overview

Measurement Practice

Two RSUs were installed at two different gantries, described in the last section. In the measurement vehicle the OBU was installed. During one measurement lap both RSUs were passed two times, one time in direction west and one time in direction east. Figure 4.21 shows an schematic overview of the measurement scenario. The RSUs were transmitting continuously all the time, where the OBU, acting as receiver, was switched on before entering the coverage area of the RSU. The maximum coverage area was found in first trials before the real measurements and adding a margin, in order to switch on the receiver long enough before entering the coverage area. Each parameter setting was measured three times. An overview of this measurement campaign and measurement results for scenario 1 (high RSU) can be found in [32].

5

Measurement Based Vehicular Radio Channel Characterization

In this chapter I present the results from the channel measurement campaigns described in Ch. 4, in order to characterize the vehicular radio channel. In each section the methodology, i.e., the mathematical equations, in order to get the channel characteristics and metrics are described. Further, examples of typical measurement runs from the different scenarios of the two measurement campaigns, LUND'07 and DRIVEWAY'09, are given. All these characteristics are important for the description of the vehicular radio channel and further for the development or parametrization of channel models. One channel model, developed and parametrized based on measurement results on the highway from the LUND'07 campaign is explained in [28]. It is a geometry-based stochastic MIMO model for V2V communications.

Sec. 5.1 describes the pathloss evaluation from our measurements, including pathloss models for four different scenarios (rural, highway, urban, and suburban). In Sec. 5.2, I show how the LSF can be estimated from our measurement data and the estimation of the stationarity time. Section 5.3 describes the time evolution of the APDP and DSD in various scenarios. This chapter closes with Sec. 5.4, where I present a comparison of the vehicular channel model proposed in [80] with our channel measurement data.

5.1 Pathloss

The pathloss is the single most important quantity of any wireless system. Therefore I describe the pathloss derivation from our LUND'07 measurement campaign in this section. I present the pathloss model, developed by Karedal et al. [25], for the four different scenarios considered in the LUND'07 measurement campaign: highway, rural, urban, and suburban. In the beginning I exemplify how the pathloss from one measurement run fits to the standard pathloss model [4, Ch. 4].

The small-scale averaged channel gain at time i is derived, as explained in [25], from the TF $H[k, q; p]$ with

$$G_{\mathrm{ch}}[i] = \frac{1}{K_{av} N_f} \sum_{k=i}^{i+(K_{av}-1)} \sum_{q=1}^{N_f} \sum_{p=1}^{P} |H[k, q; p]|^2, \tag{5.1}$$

where k is the discrete time, q is the discrete frequency, p is the antenna element link number, P is the maximum number of antenna element links, N_f is the overall number of frequency bins, and K_{av} is the number of snapshots of the averaging window. The averaging time interval K_{av} is chosen to approximately equal the distance of 20 wavelengths for convoy measurements and 10 wavelengths for opposite direction measurements. It has to be ensured that the channel is staying WSS during this time interval, see Sec. 5.2 for more details. The pathloss PL at time instant k is then calculated by

$$PL[k] = 10 \log_{10} (G_{\mathrm{Tx,iso}}) + 10 \log_{10} (G_{\mathrm{Rx,iso}}) - 10 \log_{10} (G_{\mathrm{ch}}[k]) \tag{5.2}$$

where $G_{\mathrm{Tx,iso}}$ and $G_{\mathrm{Rx,iso}}$ are the antenna gains of the Tx and Rx, respectively. The distance between the measurement vehicles was estimated by the propagation delay τ of the first arriving MPC, because the GPS data was found to be too inaccurate especially in the urban scenarios. The distance d was then calculated from $d = \tau c_0$, where c_0 is the speed of light.

Example - V2V Highway Scenario: In this example I consider a highway scenario with medium traffic (approximately 1 vehicle per second), where the vehicles traveled in opposite directions. Figure 5.1 (a) shows the Rx vehicle traveling on the opposite lane just before the vehicles were passing. The satellite photo of the highway scenario indicates that the Tx vehicle was heading in southwest direction while the Rx vehicle headed northeast. This example is also presented in [24]. Each vehicle was traveling with a speed of 90 km/h, which results in a relative speed between the vehicles of 180 km/h.

In this example I used an averaging time window of $K_{av} = 75$ snapshots that equals $t_{av} = 23$ ms or 20 wavelengths. For this scenario, the channel can be considered to be WSS during time intervals of 23 ms duration, cf. stationarity time investigations in [26]. This result of the stationarity time is also shown in Sec. 5.2.

(a) (b)

Figure 5.1: (a) Photo of the highway from the passenger compartment, (b) satellite photo of the highway E22 in the east of Lund (source: [75])

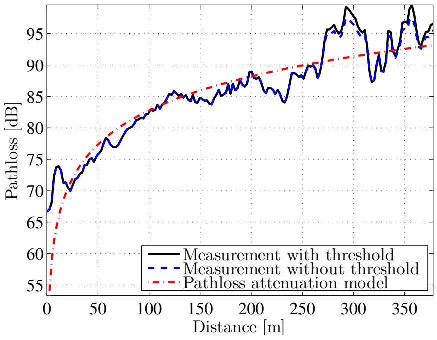

Figure 5.2: Comparison between measured pathloss (*with* and *without* noise threshold) and a pathloss model with attenuation coefficient 1.8

After calculating the Rx power and investigating the noise level, I used a noise threshold of $-102.7\,\mathrm{dBm}$ for this example. In the following, I show that a noise threshold does not have a large effect on the calculation of the pathloss. All values below the noise threshold are considered as noise and set to zero. Figure 5.2 presents the pathloss PL (with and without noise threshold). We fitted the measured pathloss in dB to the classical power law model [4, Ch. 4]

$$PL(d) = 20\,\log_{10}\left(\frac{4\pi f_\mathrm{c}}{c_0}\right) + 10\,n\,\log_{10}(d), \tag{5.3}$$

where d is the distance between Tx and Rx, f_c is the center frequency, and n is the attenuation coefficient. An attenuation coefficient of $n = 1.8$ yields the lowest RMS error of $3.3\,\mathrm{dB}$ considering the noise threshold and $3.1\,\mathrm{dB}$ without considering the noise threshold. The measurement results are taken from the first $7.5\,\mathrm{s}$ of our measurement run, where the two vehicles were approaching each other. In Fig. 5.2, it can be seen that the pathloss curves calculated *with* and *without* considering the noise threshold are very close. In our measurement, small differences only occur at distances greater than $250\,\mathrm{m}$

(see Fig. 5.2). This is because large pathlosses correspond to small Rx power and then the noise power affects the result. It can be concluded that the inclusion of a noise threshold has no significant impact on the pathloss.

Pathloss Modeling: The development of this pathloss modeling, based on the LUND'07 measurement campaign, is published by Karedal et al. [25] In the observations of the pathloss over time (distance) from our measurements we found that there is an offset between the pathloss when the vehicles are approaching each other and when the vehicles are leaving. The reason for this is the combined antenna gain including the vehicle structure. Considering the antenna mounting of the LUND'07 measurement campaign in Figs. 4.2, 4.4, and 4.6 you can observe that there are differences of the structure of the vehicle into the front direction, compared to the reverse direction. In our case the pathloss is always higher when the vehicles were leaving, which means that the combined antenna gain (including the vehicle) is larger into the driving direction, compared to the reverse direction. This also shows the importance of antenna pattern measurements including the vehicle, for the evaluation and modeling of measurement data, as we did it in our second vehicular channel measurement campaign DRIVEWAY'09. The effect of different gains, depending on the direction, is also confirmed by our pathloss values from the measurements where the vehicles were traveling in the same direction. In these measurements the pathloss is on average the approximate mean of the corresponding "forward" and "reverse" pathloss. In order to include this effect of different pathlosses, depending on the position of the vehicles we split the measurements in three groups (vehicles are approaching, vehicles are leaving, and vehicles in convoy), extract the model parameters separately for each group and derive the final model parameters by averaging over the separated parameters. The constant offset for the "forward" and "reverse" pathloss is included by introducing a correction term which is added (reverse direction), subtracted (forward direction) or ignored (convoy).

For the rural scenario we found that the pathloss fits to the well-known two-ray propagation model [4]. This can be explained by the existence of only a few scatterers in this scenario. Therefore we get a dominant LOS and one dominant MPC from a ground reflection. The two-ray propagation model was also proposed in [10] for a rural and for a highway scenario. We model the pathloss PL for the rural scenario as in [10] with this two-ray propagation model

$$\begin{aligned} PL(d) = 20\log_{10}\left(\frac{4\pi f_\mathrm{c}}{c_0}\right) - G_{12} + X_{\sigma_1} + \zeta PL_c \\ - 20\log_{10}\left|\frac{\exp\{-\mathrm{j}k_0 d\}}{d} + \rho\frac{\exp\left\{-\mathrm{j}k_0\sqrt{d^2+4h_\mathrm{ant}^2}\right\}}{\sqrt{d^2+4h_\mathrm{ant}^2}}\right|, \quad (5.4) \end{aligned}$$

where G_{12} is a constant, X_{σ_1} a zero-mean, normally distributed random variable with standard deviation σ_1, $k_0 = 2\pi f_\mathrm{c}/c_0$ is the wavenumber at the center frequency f_c, ρ is the ground reflection coefficient, h_ant is the antenna height (which is assumed to be equal on both link ends), PL_c is a correction term that accounts for the offset between "forward" and "reverse" pathloss, and ζ is 1 for "reverse" pathloss, -1 for "forward" pathloss, and 0 for convoy pathloss.

At small distances between the Tx and Rx the two-ray structure cannot be observed, therefore we limit the range of validity of the models to distances $d \geq 20\,\mathrm{m}$.

For the other three environments (suburban, urban, and highway) the comparison of the two-ray propagation model with our measured pathloss did not produce meaningful results. The reason for this is that in this scenarios there are much more scatterers in the vicinity (vehicles, traffic signs, guard rails, etc.) so that the single MPC from the reflection of the ground is not dominant anymore. Further, since there was more traffic on the roads during our measurements the other vehicles are blocking the ground reflection. For this reason we apply the classical power law to the data of these scenarios. The pathloss from the classical power law is given by

$$PL(d) = PL_0 + 10\, n \log_{10}\left(\frac{d}{d_0}\right) + X_{\sigma_2} + \zeta PL_c, \quad \text{for} \quad d > d_0 \tag{5.5}$$

where PL_0 is the pathloss at a reference distance d_0 and X_{σ_2} a zero-mean, normally distributed random variable with standard deviation σ_2. From our measurements we have just a few samples of the pathloss at distances smaller than 10 m, therefore we let $d_0 = 10\,\mathrm{m}$ and limit the model to a range of validity of $d \geq 10\,\mathrm{m}$. It can be seen that Eq. (5.3) is equal to the deterministic part of Eq. (5.5), without the pathloss correction term ζPL_c, and $PL_0 = 20\log_{10}(4\pi f_\mathrm{c}/c_0)$ at $d_0 = 1\,\mathrm{m}$.

The best-fit of the derived rural pathloss from the measurements to the deterministic part of the model Eq. (5.4) and the derived highway, urban, and suburban pathloss to the deterministic part of the model Eq. (5.5) is shown in Fig. 5.3 (a), (b), (c), and (d), respectively. It can be seen that the highs and lows of the multiple measurements from the rural scenario are very consistent and fit very well to the two-ray pathloss model. For the other scenarios there are some deviations, e.g., the large pathloss at distances $d = 20-30\,\mathrm{m}$ in the highway scenario can be explained by LOS obstruction in a particular measurement run.

In Tab. 5.1 the extracted model parameters for the four scenarios are summarized. In the case of the suburban measurements, only convoy measurement runs were carried out, which is the reason for the absence of the pathloss correction term. The extracted parameters from the power law model of the highway scenario ($n = 1.78$, $\sigma = 3.2$) and urban scenario ($n = 1.68$, $\sigma = 1.7$) agree very well with the paramters found in [10] (highway: $n = 1.85$, $\sigma = 3.2$, urban: $n = 1.61$, $\sigma = 3.4$). It is interesting that all the

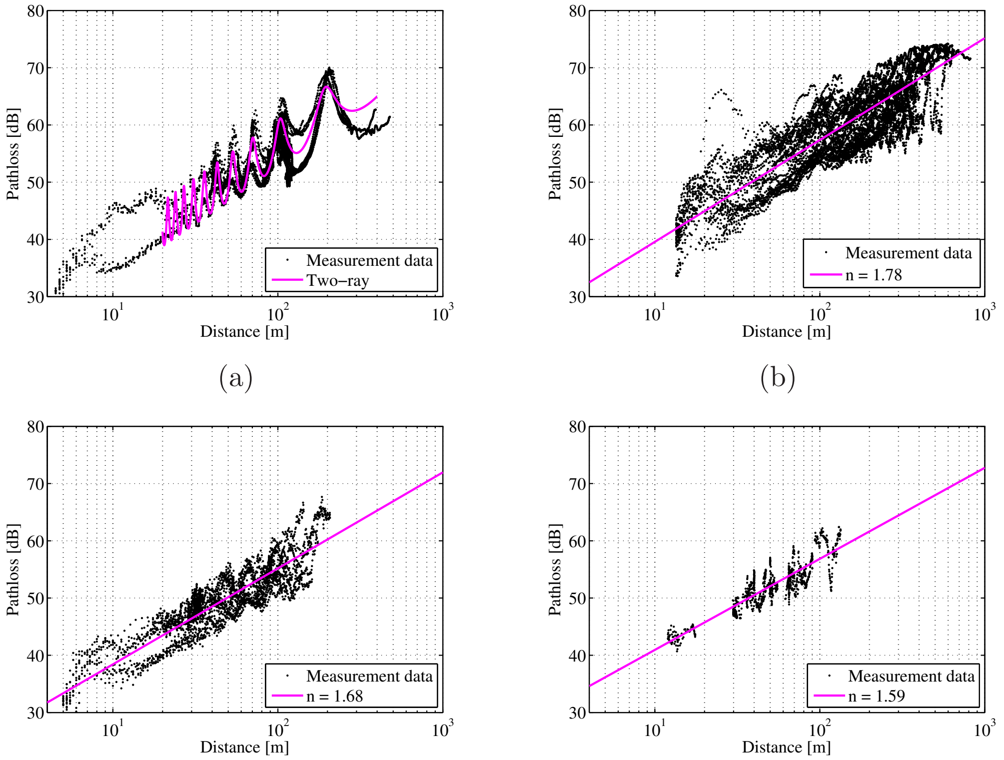

(a) (b) (c) (d)

Figure 5.3: Measured pathloss and best-fit (in a least-square sense) to the deterministic part of the applied pathloss models for (a) rural, (b) highway, (c) urban, and (d) suburban environments (source: [25])

Table 5.1: Parameters for the two-ray model (rural) and power law model (highway, urban, and suburban) (source: [25])

Scenario	**Power law**		**Two-ray model**					
	PL_0	n	G_{12}	h_{ant}	$\lvert\rho\rvert$	$\angle\rho$	$\sigma_{1,2}$	PL_c
Rural	-	-	30.9	2.53	0.44	$-130°$	2.6	2.3
Highway	39.6	1.78	-	-	-	-	3.2	3.3
Urban	38.4	1.68	-	-	-	-	1.7	1.5
Suburban	40.9	1.59	-	-	-	-	2.1	N/A

pathloss exponents are smaller than 2, which is the exponent of free space propagation. Such low pathloss exponent were also found, e.g., in [81], from measurements in indoor environments. This effect can be caused by waveguiding effects, see Sec. 3.1.4. This effect is simply explainable for the urban and suburban environments, due to the presence of street canyons, but maybe less obvious for the highway environment. One possible explanation for this waveguiding on the highway can be found in the guard rails. They do not have so large dimensions as the buildings next to the street in the urban and suburban environments, but enforce the waveguiding effect concerning its metallic material.

A further evaluation, especially on the frequency dependency of the explained models can be found in [25].

5.2 Local Scattering Function

In Sec. 3.2.2 I described the common continuous concept of the LSF $\mathcal{P}_S(t, f; \tau, \nu)$ and the GLSF $\widetilde{\mathcal{P}_S}(t, f; \tau, \nu)$ as it is defined in [15]. In the following I give a description how the estimation of the discrete GLSF $\widetilde{\mathcal{P}_S}[k, q; l, m]$ can be applied on our vehicular channel measurement data. A similar description of this estimation method can be find in [26].

For the sake of simplicity I will from now on omit the explicit dependency of $\widetilde{\mathcal{P}_S}[k, q; l, m]$ on the frequency q considering the dependency of the GLSF $\widetilde{\mathcal{P}_S}[k; l, m]$ on the time k only. An extension to time *and* frequency dependency is presented in [37].

I use a discrete time implementation of the scattering function estimator. The temporally localized low-pass filters $\boldsymbol{G}_r$ are represented by the sampled TF $H_{\boldsymbol{G}_r}[k, q]$ for $q \in \{-Q/2, \ldots, Q/2 - 1\}$. I apply the discrete time equivalent of the separable TF used in [66]

$$H_{\boldsymbol{G}_r}[k, q] = u_i[k + K/2]\, \tilde{u}_j[q + Q/2]\,, \tag{5.6}$$

where $r = iJ + j$, $i \in \{0, \ldots, I - 1\}$, and $j \in \{0, \ldots, J - 1\}$. The sequences $u_i[k]$ are the Discrete Prolate Spheroidal (DPS) sequences with concentration in the interval

$\mathcal{I}_K = \{0, \ldots, K-1\}$ and bandlimited to $[-I/K, I/K]$, defined as [82]

$$\sum_{\ell=0}^{K-1} \frac{\sin(2\pi I/K(\ell-k))}{\pi(\ell-k)} u_i[\ell] = \lambda_i u_i[k] \,. \tag{5.7}$$

The sequences $\tilde{u}_j[q]$ are defined similarly with concentration in the interval $\mathcal{I}_Q$ and bandlimited to $[-J/Q, J/Q]$. The multi-window spectrogram is computed according to

$$\widetilde{\mathcal{P}_S}[k; l, m] = \frac{1}{IJKQ} \sum_{r=0}^{R-1} \left| \mathcal{H}^{(\boldsymbol{G}_r)}[k; l, m] \right|^2 \tag{5.8}$$

with $l \in \{0, \ldots, Q-1\}$ and $m \in \{-K/2, \ldots, K/2-1\}$ where

$$\mathcal{H}^{(\boldsymbol{G}_r)}[k; l, m] = \sum_{k'=-K/2}^{K/2-1} \sum_{q'=-Q/2}^{Q/2-1} H[k', q'] H_{\boldsymbol{G}_r}[k'-k, q'] \mathrm{e}^{-\mathrm{j}2\pi(mk'-lq')} \,. \tag{5.9}$$

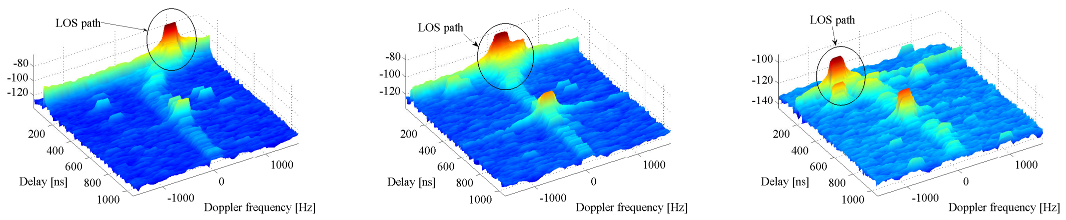

(a) (b) (c)

Figure 5.4: Estimated GLSF for different time snapshots from the example scenario: (a) $t = 0\,\mathrm{s}$, (b) $t = 0.5\,\mathrm{s}$, and (c) $t = 1.5\,\mathrm{s}$

Example - V2V Highway Scenario: I estimate the LSF from noisy measurements using Eq. (5.8). As temporal windows I use $I = 5$ DPS sequences with energy concentration in an interval with length $K = 64$ assuming a lower bound of the stationarity time of $T_{\mathrm{stat}} > K t_{\mathrm{rep}} = 19.7\,\mathrm{ms}$, where $t_{\mathrm{rep}} = 3.2\,\mu\mathrm{s}$ (LUND'07 measurement campaign). In the frequency domain I use $J = 1$ DPS sequence with concentration in the interval with length $Q = 256$ assuming a stationarity bandwidth of $B_{\mathrm{stat}} > 240\,\mathrm{MHz}$. This assumption can be justified by the fact that 240 MHz corresponds to less than 5% relative bandwidth and the antenna Voltage Standing Wave Ratio (VSWR) varies by less than 1 dB over the measurement bandwidth. With these assumptions I achieve a Doppler resolution of 51 Hz for the GLSF.

The estimated GLSF can directly be related to the propagation scenario. In the following I describe the estimated GLSF by means of the measurement of an example scenario. It is the same example scenario as considered for the pathloss calculation in Sec. 5.1, V2V highway, see Fig. 5.1. Figure 5.4 presents the estimated GLSF from this example scenario for three different time snapshots: (a) $t = 0\,\mathrm{s}$ — vehicles are approaching, (b) $t = 0.5\,\mathrm{s}$ — vehicles are passing and (c) $t = 1.5\,\mathrm{s}$ — vehicles are leaving.

The time variance of the GLSF can be explained by focusing on the LOS component. In Fig. 5.4 (a) the LOS component has a delay of approx. 110 ns and a Doppler frequency of approx. 865 Hz. This Doppler frequency agrees exactly with our intended speed of 180 km/h, 90 km/h for each of the two vehicles. Figure 5.4 (b) shows a LOS component with reduced delay (approx. 60 ns) — vehicles are now closer together — and a Doppler frequency near to 0 Hz. In this passing scenario the LOS component wave propagation is perpendicular to the driving direction. In Fig. 5.4 (c) an increased delay of approx. 190 ns and a Doppler frequency of approx. −815 Hz can be observed. In this case the relative speed between the two vehicles is a little bit lower than the intended speed of 180 km/h. The negative Doppler frequency confirms that the vehicles are leaving at this time.

Beside this strong LOS component in Fig. 5.4 there also exists smaller MPCs with variant delays and Doppler frequencies, which also indicate the time variance of the GLSF, and therefore a non-WSS channel.

Parametrization of the GLSF Estimator: The parametrization of the GLSF, based on the LUND'07 measurements, is published by Bernadó et al. [27]. As stated above the estimation of the GLSF depends on several parameters: number of multitapers in time I and frequency J, which are chosen to be DPS sequences, length of stationarity region in time K and frequency Q. In the example above the length of the stationarity regions is assessed by means of the collinearity measure without optimizing the estimator parameters. [27] investigates the Mean Square Error (MSE) between the original TF and the estimated TF by the GLSF. The GLSF estimator parameters I, K, and Q (the frequency stationarity region is assumed to be larger than 240 MHz as mentioned above and therefore a constant $Q = 256$ is chosen) are optimized, by minimizing the MSE.

A detailed description of the optimum parameters is explained in [27]. In the following I give an overview of the considered scenarios from the LUND'07 measurement campaign and the resulting optimum parameters. Three different scenarios were chosen, where in each of them the vehicles were driving in opposite directions, because this yields the largest time variations. Further two different speeds of the vehicles (the same speed for the Tx and Rx vehicle) were considered in each scenario:

Scenario 1: Highway environment. There exists a strong LOS component and diffuse as well as discrete MPCs. Considered speeds: (a) 110 km/h and (b) 90 km/h.

Scenario 2: Rural environment. There exists a strong LOS component and diffuse MPCs, but no additional components. Considered speeds: (a) 70 km/h and (b) 50 km/h.

Scenario 3: Urban environment. There exists a strong LOS component and large diffuse MPCs and additional discrete MPCs comming from reflections from close objects.

Table 5.2: MMSE for the optimal choice of $(I,\ J)$ for different scenarios and different stationarity length K. The values of MMSE are scaled by 10^{-4} (source: [27])

Scenario		**Stationarity length K**			
		64	128	256	512
Highway	110 km/h	(1, 4) - 10.07	(2, 3) - 9.11	(3, 4) - 8.97	(3, 4) - 10.07
Highway	90 km/h	(1, 4) - 8.48	(3, 3) - 7.95	(3, 3) - 7.92	(3, 4) - 8.92
Rural	70 km/h	(1, 4) - 6.61	(3, 3) - 5.97	(3, 3) - 5.80	(5, 3) - 6.06
Rural	50 km/h	(1, 4) - 6.24	(1, 4) - 5.53	(3, 3) - 5.28	(3, 3) - 5.43
Urban	50 km/h	(1, 4) - 8.94	(1, 4) - 7.50	(3, 3) - 7.21	(3, 3) - 7.29
Urban	30 km/h	(1, 4) - 8.23	(1, 4) - 6.70	(3, 3) - 6.11	(3, 3) - 6.10

Considered speeds: (a) 50 km/h and (b) 30 km/h.

The delay spread in Scenario 1 (highway) is short, but some MPCs arrive at late delays. In Scenario 2 (rural) the delay spread is longer and Scenario 3 (urban) shows the largest delay spread with a lot of MPCs coming from close objects. In Tab. 5.2 the MMSE for the optimal choice of the number of multitapers for four different stationarity lengths $I = 64$, 128, 256, and 512 are presented. By choosing the stationarity length K properley, it can be ensured that MPCs at different delays are not correlated, i.e., they come from different scatterers. The MMSE shows the same qualitative behavior for all scenarios. When increasing the stationarity length K the MSE gets smaller and than grows again. It can be seen that the increase is higher for higher speeds (highway scenario: 110 km/h and 90 km/h). Furthermore it can be observe that the number of multitapers is increasing by increasing the stationarity length. This can be explained by a higher variation of the process for longer stationarity regions and therefore more multitaper windows are needed for the GLSF estimator.

Considering the same scenario but the different speeds, it can be seen that the MMSE is always smaller for the lower speed. This is because a higher speed results in more time fluctuations, which results in a larger MMSE. Even the vehicles are driving faster in the rural scenario, compared to the urban scenario, the MMSE is smaller in the rural scenario. This is because the delay spread in the urban scenario is higher with a lot of MPC from close objects, resulting in a high time-varying process.

5.2.1 Stationarity Time

The stationarity time T_{stat} is a very important metric for non-WSSUS channels that is also necessary for the parametrization of the GLSF estimation. In the following I describe how T_{stat} can be estimated from the collinearity of the GLSF. This description is also presented in [26].

Collinearity of the GLSF Sequence

The collinearity of the GLSF sequence between two time instances allows to quantify the dimension of the stationarity region in time, i.e., the stationarity time T_{stat} of the non-WSSUS fading process. For the duration of the stationarity time simplified WSSUS models can be applied. Note that the stationarity time will be itself time-variant $T_{\text{stat}}[k]$ since it depends on the changing environment.

In [83] the APDP is used to obtain an estimate of the stationarity time of the fading process. I extend this approach by using the GLSF which incorporates dispersion in delay and Doppler. To obtain estimates for the time-variant stationarity time $T_{\text{stat}}[k]$ I proceed in two steps. Firstly I compute collinearity of the GLSF sequence. Secondly I set a threshold for the collinearity. Similar to [83] I define the stationarity time as the support of the region where the collinearity exceeds the given threshold.

I stack all $K \times Q$ (delay $\times$ Doppler) elements of the GLSF $\widetilde{\mathcal{P}_S}$ in the vector $\widetilde{\boldsymbol{\mathcal{P}}_{\boldsymbol{S}}}[k]$ computing the collinearity of the GLSF

$$R_{\widetilde{\mathcal{P}_S}}[k_1, k_2] = \frac{\widetilde{\boldsymbol{\mathcal{P}}_{\boldsymbol{S}}}[k_1]^{\mathrm{T}} \widetilde{\boldsymbol{\mathcal{P}}_{\boldsymbol{S}}}[k_2]}{\|\widetilde{\boldsymbol{\mathcal{P}}_{\boldsymbol{S}}}[k_1]\| \|\widetilde{\boldsymbol{\mathcal{P}}_{\boldsymbol{S}}}[k_2]\|} \tag{5.10}$$

for two time instances k_1 and k_2, i.e., a distance measure in Hilbert space.

For the following examples I calculate $R_{\widetilde{\mathcal{P}_S}}[k_1, k_2]$ using a step size of $\Delta k = 10$, $k_1 = \Delta k k_1'$ and $k_2 = \Delta k k_2'$ for $k_1', k_2' \in \{0 \dots K_{\text{seg}}/\Delta k - 1\}$ to limit the computational complexity, where K_{seg} is the considered segment length in time domain. I consider three different scenarios for the further estimation of the stationarity time:

Scenario 1: Highway environment, where the vehicles are driving in opposite directions with a speed of 90 km/h.

Scenario 2: Highway environment, where the vehicles are driving in the same direction with a speed of 90 km/h.

Scenario 3: Urban environment, where the vehicles are driving in the same direction with a speed of 30 km/h.

No significant signal components were measured for delays larger than $1\,\mu$s, hence I consider only the first $Q = 256$ delay samples, $l \in \{0, \dots, Q-1\}$. The time index k was limited to a segment with time duration of 2 s for all three scenarios, $k \in \{0, \dots, K_{\text{seg}} - 1\}$ with $K_{\text{seg}} = 6500$.

I consider only a single antenna link out of the set of 16 individual links. In the case of Scenario 1 I investigate the link between the antenna elements whose main lobes are facing towards each other, when the vehicles are approaching. In the other two Scenarios 2 and 3 I also consider a link where the elements are facing towards each other during the whole time duration of 2 s.

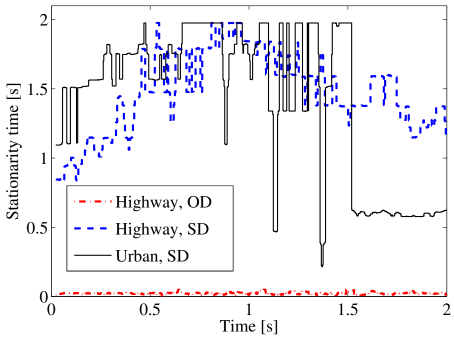

Figure 5.5: Stationarity time for the three scenarios: Scenario 1 - highway, opposite directions (OD), Scenario 2 - highway, same directions (SD), Scenario 3: urban, same directions

Stationarity Time Estimates

In order to estimate the stationarity time I have to set a threshold for the collinearity. Similar to [83] I define the stationarity time as the support of the region where the collinearity exceeds a certain threshold. I define the indicator function

$$\gamma[k', \tilde{k}] = \begin{cases} 1 & \text{for} \quad R_{\widetilde{\mathcal{P}_S}}[k', k' + \tilde{k}] > c_{\text{thres}} \\ 0 & \text{otherwise} \end{cases} \tag{5.11}$$

to estimate the (time-variant) stationarity-time as

$$T_{\text{stat}}[k'] = \Delta k t_{\text{rep}} \sum_{\tilde{k}=-K_{\text{seg}}/\Delta k-1}^{K_{\text{seg}}/\Delta k-1} \gamma[k', \tilde{k}]. \tag{5.12}$$

In contrast to the spatial distance expression in [83] I specify a stationarity time. Spatial distances are difficult to compare if both, Tx and Rx, are moving. For the estimation of the stationarity time I specify a threshold of $c_{\text{thres}} = 0.9$ ($10\log_{10}(0.9) = -0.46$).

Figure 5.5 shows the time-variant stationarity time for each of the three scenarios over the duration of 2 s. A very short stationarity time with a mean of 23 ms for the highway scenario, where the vehicles are driving in opposite directions (Scenario 1), can be observed. The highway scenario, where the vehicles are driving in the same direction (Scenario 2), shows a mean stationarity time of 1479 ms and the urban scenario, where the vehicles are driving in the same direction (Scenario 3), a mean time of 1412 ms.

In the case of Scenario 1, where the vehicles are traveling in opposite directions the stationarity time is very short. Scenario 2 and 3, where both vehicles are traveling in the same direction, show a larger stationarity time. It is interesting that the stationarity times of these two scenarios are in a similar range, because the number of scatterers in these scenarios is very different — only a few scatterers in Scenario 2 and many scatterers in

Scenario 3. In this case it is also important to consider the different speed of the vehicles in the two scenarios — 90 km/h in Scenario 2 and 30 km/h in Scenario 3. This means that the vehicles in Scenario 2 cover a larger distance than in Scenario 3.

5.3 Average Power-Delay Profile and Doppler Spectral Density

In this section I characterize the vehicular radio channel in the time-delay domain and time-Doppler domain. The time-delay characterization is based on the PDP given in Eq. (3.29). I define an estimator for the PDP called APDP $P_{\mathrm{APDP}}(t,\tau)$. The APDP is calculated by averaging the magnitude squared of the IR over a specific time interval K_{av} (ensemble realizations over time) in order to average over the small scale fading, and taking the sum over all single antenna element links (ensemble realizations over space). The length of the time interval has to be chosen long enough, in order to get a reasonable averaging, and not longer than the WSS of the channel is valid, see Sec. 3.2.1. Then the APDP at the time i is calculated via

$$P_{\mathrm{APDP}}[i,l] = \frac{1}{K_{av}} \sum_{k=i}^{i+(K_{av}-1)} \sum_{p=1}^{P} |h[k,l;p]|^2. \tag{5.13}$$

In the following I present two examples of the time-varying APDP of selected scenarios from the LUND'07 channel measurement campaign (urban, V2V, opposite directions and highway, V2V, opposite directions). Further I present two application specific example scenarios from the DRIVEWAY'09 measurement campaign. The first scenario was measured on the highway, where the Rx vehicle is overtaking the Tx vehicle in a traffic jam. Possible safety-related applications for this scenario are collision avoidance, traffic condition warning, and lane change assistance. The second selected example scenario is called general LOS obstruction. There is a truck between our two measurement vehicles. This scenario is also typical for lane change assistance. For these two scenarios I present the APDP and the DSD calculated from the GLSF described in Eq. (5.8). With the GLSF the time-variant APDP is calculated by

$$P_{\mathrm{APDP}}[k;l] = \sum_{m=-K/2}^{K/2-1} \sum_{p=1}^{P} \widetilde{\mathcal{P}_S}[k;l,m;p], \tag{5.14}$$

and the time-variant DSD

$$P_{\mathrm{DSD}}[k;m] = \sum_{l=-Q/2}^{Q/2-1} \sum_{p=1}^{P} \widetilde{\mathcal{P}_S}[k;l,m;p], \tag{5.15}$$

where I sum the APDPs and DSDs over all $P = 16$ single antenna element links.

Scenario 1 - Urban, V2V, Opposite Directions: This measurement was carried out during the LUND'07 measurement campaign. The measurement vehicles were traveling in opposite directions in an urban environment at a speed of 50 km/h, each. Figure 5.6 presents the measured street having buildings on the left hand side and leafless trees on the right hand side. This measurement example can be also found in [11].

Figure 5.6: Photo of the street "Esplanaden" in the center of Lund (Scenario 1)

For this scenario I was averaging the magnitude squared of the IR over 40 wavelengths. This equals at a relative speed of 100 km/h a distance of 2.3 m and thus yields an averaging time of $t_{av} = 83\,\mathrm{ms}$, i.e., $K_{av} = 271$ snapshots. The two vehicles were passing each other after 1.6 s of the 10 s measurement time.

Figure 5.7 shows the strong LOS component (i) with decreasing delay until 1.6 s (vehicles passing) and increasing delay afterwards. There are also several MPCs (ii) with constant delay over the time. The explanation for such a constant-delay component is depicted in Fig. 5.8. The reflector is along a straight line connecting the two vehicles, where one vehicle is approaching the reflector and the other is driving away from it. Note that such MPCs also show zero Doppler shift.

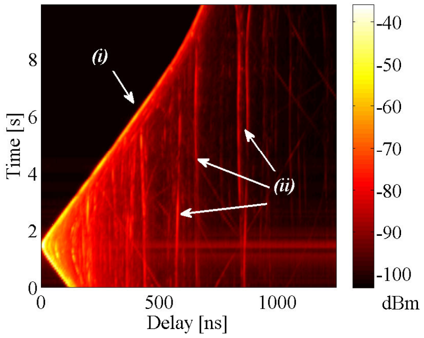

Figure 5.7: Time-varying APDP for V2V in opposite directions and urban environment (Scenario 1)

Figure 5.8: Scenario leading to constant delay scatterer

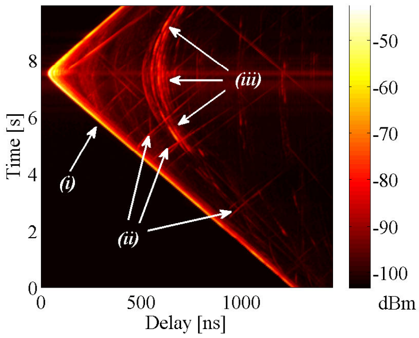

Figure 5.9: Time-varying APDP for V2V in opposite directions and highway environment (Scenario 2)

Scenario 2 - Highway, V2V, Opposite Directions: In this example I consider a highway scenario with medium traffic (approximately 1 vehicle per second), where the vehicles traveled in opposite directions. It is the same example scenario as used for the estimation of the pathloss in Sec. 5.1. Figure 5.1 (a) shows the Rx vehicle traveling on the opposite lane just before the vehicles were passing. The satellite photo of the highway scenario, see Fig. 5.1 (b), indicates that the Tx vehicle was heading in southwest direction while the Rx vehicle headed northeast. The speed of each vehicle was approximately 90 km/h, which results in a relative speed between the two vehicles of approx. 180 km/h. The evaluation of this example scenario was first presented in [24]. For this measurement run I used an averaging time of $t_{av} = 23\,\text{ms}$, i.e., $K_{av} = 75$ snapshots.

Figure 5.9 shows the strong LOS component (i) with decreasing delay until 7.5 s (vehicles passing) and increasing afterwards. There are also several MPCs (ii) whose trajectories in Fig. 5.9 are approximately parallel to the LOS component. These MPCs are scattered at vehicles that are traveling with approximately the same speed as our measurement vehicles. Such a MPC show parallel behavior over time to the LOS component if the speed of the scattering vehicle equals the measurement vehicle. Further, there is a group of MPCs (iii) from approx. 5 s to 10 s, whose delays are slightly decreasing from a delay of about 700 ns to 600 ns until a time of 7.5 s and increasing afterwards. These MPCs are much stronger than most of the MPCs, reflected from vehicles. The most likely explanation for this group of MPCs is scattering at factory buildings in the southeast of the highway, see Fig. 5.1 (b). Note that such MPCs should show a Doppler shift that is less than the Doppler shift of the LOS component, because the angle between driving direction and wave propagation direction is larger than zero.

Scenario 3 - Highway, V2V, Overtaking in Traffic Congestion: For the estimation of the GLSF, which is used for the calculation of the APDP and DSD for this and the following example scenario, I used a time window length $K = 128$ and a frequency window length of $Q = 256$. The considered number of snapshots for this scenario is equal to the overall number of snapshots from this measurement run $N_t = K_{\text{seg}} = 32500$.

In this scenario the Tx vehicle is stuck in a traffic congestion on the right lane, whereas the Rx vehicle overtakes the Tx on the left lane. This situation is of special interest from the traffic safety point of view. It is not uncommon that the driver of a vehicle stuck in a traffic congestion on a single lane suddenly wishes to change lane. This example measurement was carried out during the DRIVEWAY'09 measurement campaign and was first presented in [12].

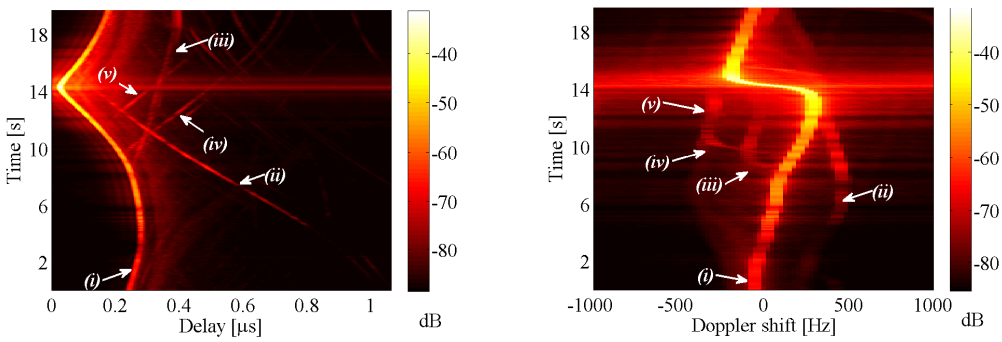

(a) (b)

Figure 5.10: Time-varying (a) APDP and (b) DSD for overtaking in traffic congestion (Scenario 3)

I analyze different MPCs in the APDP and DSD, labeled in Fig. 5.10 from (i) to (v). Figure 5.11 shows a model of the mobile and static scatterers. MPC (i) corresponds to the LOS between the Tx and Rx vehicle. In the beginning, the Rx stays on the right lane behind a large truck and moves to the left in order to overtake the Tx. In Fig. 5.10 (a) it can be seen how the delay corresponding to this path gets slightly longer in the beginning, because the Tx vehicle is driving faster than the Rx vehicle. After some seconds the Rx vehicle accelerates and therefore the delay gets shorter until the Rx overtakes the Tx at 14.3 s. At this time the delay is the shortest, corresponding to a distance between

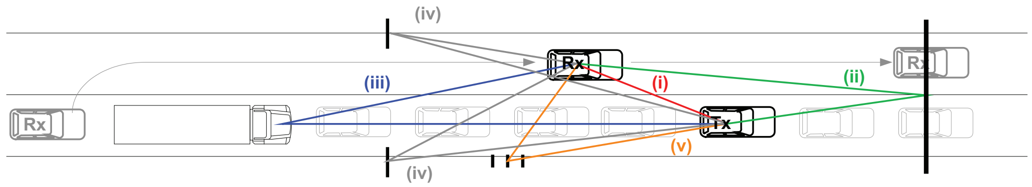

Figure 5.11: Scatterers distribution model for overtaking in traffic congestion

the vehicles of about 4 m. Since this is the minimum distance between the measurement vehicles the received power achieves its maximum at this time.

In Fig. 5.10 (b) the Doppler shift is negative in the beginning, when both vehicles are on the right lane and stuck in the traffic congestion (the Tx vehicle is driving slightly faster than the Rx vehicle). It increases towards positive values when the Rx starts overtaking. Between 3.5 and 14.3 s, the two vehicles are approaching (positive Doppler shift) and after 14.3 s on, the Rx drives away from the Tx (negative Doppler shift). At the end of the measurement, the Rx breaks due to a congestion also on the left lane and, as a result, the Doppler shift decreases to 0 Hz.

MPC (*ii*) corresponds to a single bounce reflection produced by a large traffic sign placed ahead of both vehicles. This MPC occurs at 4.3 s. The Rx is not able to receive it earlier because there is a large truck blocking the signal coming from this direction. The maximum Doppler shift of MPC (*ii*) is 445 Hz, which implies a relative speed of 85 km/h. At this point, Tx and Rx are driving about 25 km/h and 60 km/h, respectively.

The large truck standing in front of the Rx in the beginning of the measurement causes MPC (*iii*) after the Rx overtakes the truck at 8.7 s. The maximum Doppler shift observed on MPC (*iii*) corresponds to a relative speed of 17 km/h.

A similar phenomenon occurs for MPCs (*iv*) and (*v*). They correspond to temporary traffic signs at a construction site at both sides of the road. They contribute to the received signal as soon as they are left behind. Since both Tx and Rx are leaving these objects, the observed Doppler shift is negative and the delay increases.

The other cars present in the measurement do not have a significant influence on the wave propagation. They do not significantly contribute as scatterer and they do not shadow the LOS component. One reason is the antenna pattern and height of the vehicular antennas that are mounted on the roof of the measurement vehicles.

Scenario 4 - Highway, V2V, General LOS Obstruction: As mentioned in the beginning of the description of Scenario 3, I use a time window length and a frequency window length of $K = 128, Q = 256$, respectively, for the estimation of the GLSF and I consider the overall number of snapshots of this measurement run $N_t = K_{\text{seg}} = 65535$. In this scenario, see Fig. 5.13, the Rx drives in front of a truck at about 80 km/h and the Tx is behind this truck and drives at about 65 km/h. This is a common situation of obstructed LOS, where the first path between Tx and Rx occurs through diffraction on the roof surface of the truck. Figure 5.14 shows the APDP and DSD observed for this scenario where I identify 5 different MPCs. As Scenario 3, the evaluation of this scenario is also presented in [12].

The first MPC corresponds to the obstructed LOS between Tx and Rx. Since the Rx drives faster than the Tx, the delay of this path grows in time. Noteworthy are three

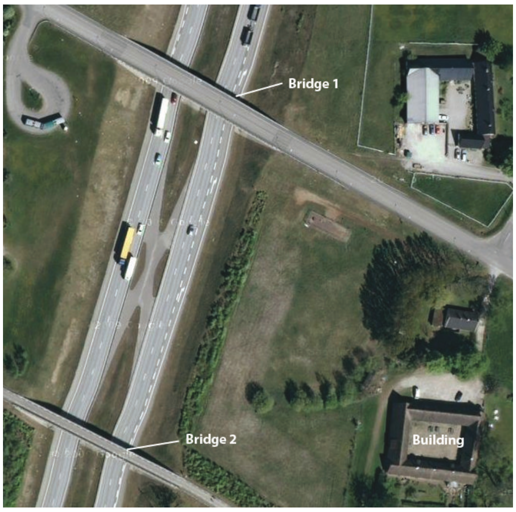

Figure 5.12: Satellite photo of scenario 4, general LOS obstruction (©2009 Google-Map data)

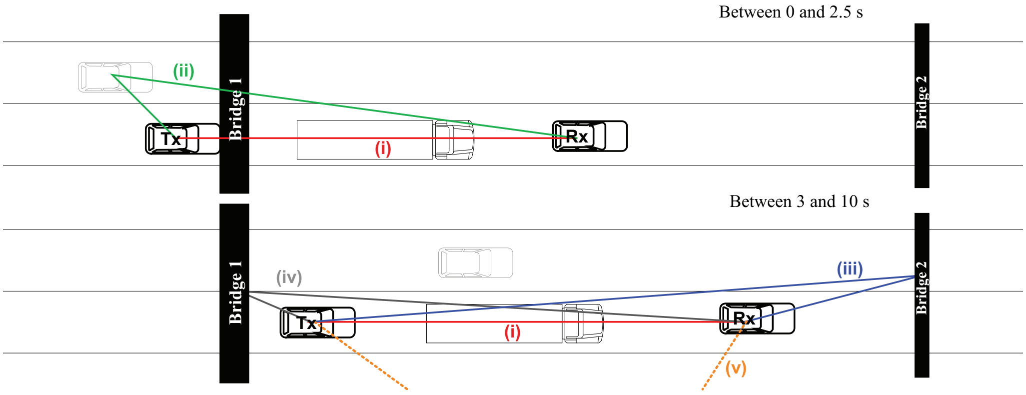

Figure 5.13: Scatterers distribution model for general LOS obstruction

intervals in which the signal strength increases. The first interval starts at time 0 s and lasts until 3 s and corresponds to the time while there is a bridge between Tx and Rx. The same phenomenon happens during a second interval, between 4.5 and 5.5 s, when the Rx passes under a second smaller bridge and at 9.5 s, when the Tx drives under this bridge. The reflections caused by these objects contribute to increasing the received power at the Rx. For the first MPC, the observed Doppler shift is slightly shifted towards negative values. The Rx drives between 10 and 15 km/h faster than the Tx, the observed Doppler shift is −63.5 Hz, well matching with a relative speed of 12 km/h. During the measurement run, the Tx decreases the speed about 5 km/h starting at 4 s, and therefore the Doppler shift of this first path gets more negative down to −89 Hz.

MPC (*ii*) corresponds to a car that passes the Tx at 1.1 s. In most measurements it is not possible to observe any contribution from other cars driving beside Tx and Rx. In

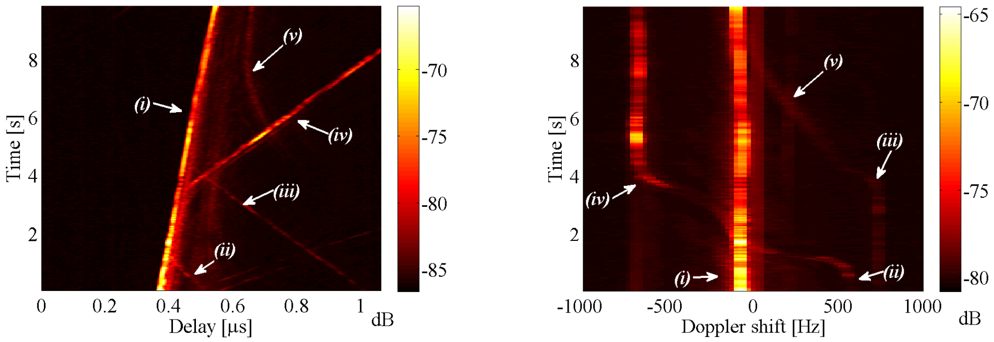

(a) (b)

Figure 5.14: Time-varying (a) APDP and (b) DSD for general LOS obstruction scenario (Scenario 4)

this case, since the overtaking takes places under the bridge, this MPC becomes stronger at that time. The Doppler shift associated to this component is 545 Hz, this leads to a relative speed of 105 km/h. Taking the Tx speed of 77 km/h and the Rx speed of 65 km/h into account, this third car should be driving at about 124 km/h.

The third MPC stems from a reflection at the second bridge and shows a decreasing delay with time. It is visible until 4.5 s, Rx passes under the bridge, and has a Doppler shift of 735 Hz, corresponding to a relative speed to the bridge from both vehicles of 142 km/h. The fourth MPC appears shortly after the Tx leaves the first bridge, and it is produced by a reflection on this bridge. The delay increases with time and the Doppler shift is -700 Hz. The observed Doppler shift of path (iv) is smaller in magnitude than the one for path (iii) because at 4 s the Tx reduces its speed below 60 km/h.

In Fig. 5.12 a large building about 100 meters off the road can be seen. This building causes the fifth MPC. Since it is an object placed far away from the Tx and Rx, the changes on the delay are smoother. The shortest delay of this MPC is 0.65 μs with a traveled distance of 195 m.

5.4 Criticism of IEEE 802.11p Model

5.4.1 Overview

In an early version of the draft standard IEEE 802.11p (D0.26) [80] a tap delay model presented for vehicular communications. This channel model is based on radio channel measurements at 2.4 GHz, described in [84] and [85]. The proposed channel model shows several weaknesses (e.g., the conclusions that are drawn for the 5.9 GHz band from 2.4 GHz channel measurements) that are stated in the following in this section. This model proposal is not anymore present in the draft IEEE 802.11p standards later than the version D0.26

[80]. No models are proposed in the subsequent versions of the draft standard. For this reason I discuss the problems of the proposed channel model, presented in [80], and propose a channel model that is more reasonable for vehicular communications.

The proposed IEEE 802.11p channel model is a tap delay model, i.e., that the IRs are modeled with components at certain delays, which are called *taps*. It is assumed that the average gain of the taps is decaying exponentially in delay lag. The amplitude statistics over time are varying, according to specific distributions, in order to implement fading. With this implementation a strong LOS component as well as a weak MPC can be implemented. An individual Doppler Spectrum is dedicated to each tap. In the following I compare this tap delay model with our measurement data from the LUND'07 measurement campaign and show why such a model does not reflect the behavior of a vehicular radio channel. This is presented in [86].

5.4.2 Measurement Scenario

I consider a highway V2V scenario in order to allow further comparison to the proposed model in the draft standard IEEE 802.11p [80], because this model is also based on V2V highway measurements. Figure 5.15 (a) shows a satellite photograph (source [75]) of the investigated highway and in Fig. 5.15 (b) a photograph taken during the measurements of the highway scenario is presented. Both vehicles were driving in the same direction. 19 measurements, each with a length of 10 s, were carried out in this scenario. In the following I denote such a single measurement with 10 s duration a *measurement run*. The speed of the measurement vehicles was 90 km/h in 10 measurement runs and 105 km/h in the other 9 measurement runs. The distance between the two vehicles was varied between 50 m and 150 m, where we kept the distance approx. constant during each measurement run.

(a) (b)

Figure 5.15: (a) Satellite photo of the highway (source: [75]) and (b) photo of the highway in the east of Lund

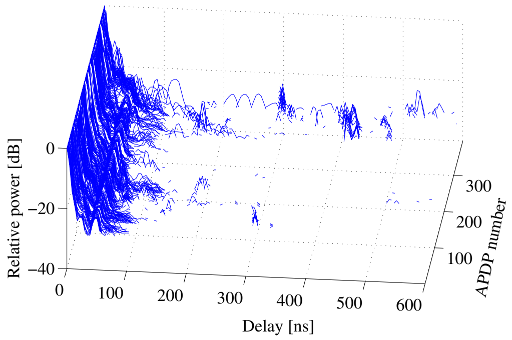

Figure 5.16: Normalized APDPs from the highway measurements

5.4.3 Evaluation Results

From our measurements I evaluated the significant parameters of the IEEE 802.11p channel model for comparison. The IEEE 802.11p channel model is a tap delay model, with 10 taps. For each tap, the gain, the excess delay, the Ricean K-factor, and significant parameters describing the Doppler spectrum, are given. A detailed description of the design of the IEEE 802.11p model can be found in [84].

Parameter Evaluation

I estimate the APDP with Eq. (5.13) with $K_{av} = 232$ snapshots for the averaging. An averaging over $K_{av} = 232$ snapshots is equal to $t_{av} = 71\,\text{ms}$ and approx. 30 wavelengths at 90 km/h. As shown in Sec. 5.2.1, $T_{\text{stat}} = 1479\,\text{ms}$ on average for the highway scenario, where the vehicles are traveling in the same directions, i.e., a WSS radio channel can be assumed over this duration of 71 ms. In order to limit the noise contribution I set all values smaller than the noise threshold of 6 dB above the noise level to zero. Further I selected only these APDPs that showed a peak-to-noise ratio greater than 35 dB. Each APDP was normalized to its maximum. Figure 5.16 shows the normalized APDP of our measurements. The maximum of each segment corresponds to the LOS component and was shifted to delay bin zero. After a delay of 200 ns I observe only a few significant parts of this average PDPs. This is much smaller than the delay duration of approx. 1 μs found in [84].

In order to make a comparison with the IEEE 802.11p model I use the same number of taps, $I = 10$, as in [84]. In [84] the delay difference between the taps is equal to the delay resolution of 50 ns. So the tap delay has equidistant values 0 ns, 50 ns, 100 ns, etc. The delay resolution of our measurements, $\Delta\tau = 4.17\,\text{ns}$, is much higher. In order to get the same tap delay I use $J = 12$ delay bins for each tap.

Table 5.3: Estimated tap model parameters

Tap	**Tap delay** [ns]	**Tap gain** [dB]	K_{Rice}
1	0	0.0	193.96
2	50	−20.2	10.34
3	100	−29.9	1.63
4	150	−33.4	0.66
5	200	−36.2	0.30
6	250	−37.1	0.24
7	300	−33.5	0.23
8	350	−40.5	0.13
9	400	−32.9	0.08
10	450	−38.7	0.05

The gain for each tap is obtained by

$$P_{\text{tap}}[k; l_i] = \frac{1}{J} \sum_{l=l_i}^{l_i+J-1} P_{\text{APDP}}[k; l], \tag{5.16}$$

for $0 \leq i \leq I-1$, where I is the number of taps and l_i is the delay bin number at the start of each tap.

By investigating the amplitude distribution of the taps I found that a Rice distribution, [61], fits very well. As in the IEEE 802.11p channel model I evaluated the Ricean K-factor K_{Rice}. I estimate the Ricean K-factor, using the moment-method, described in [87]. With this estimation I obtain a Ricean K-factor for each delay bin of the individual APDPs. In order to obtain the mean Ricean K-factor for each tap I averaged K_{Rice} over the $J = 12$ delay bins associated with each tap.

Parameter Comparison

Table 5.3 presents the estimated 10-tap model parameters from our V2V highway scenario measurements. Column one presents the tap number, column two the tap delay, the third column the relative tap gain in dB, and column four shows the tap Ricean K-factor.

The relative tap gain in Tab. 5.3 is the mean over the tap gain of all APDPs. The tap gain of the second tap is 20.2 dB below the gain of the first tap. All other tap gains are more than 29 dB lower than the maximum in the first tap. Considering the minimum peak-to-noise ratio of the APDPs of 35 dB and the noise threshold of 6 dB above the noise level, all gains lower than 29 dB below the first tap can be discarded. Compared with the IEEE 802.11p model, the tap gain extracted from our measurements decreases much faster, e.g., the tap gain of tap 2 of the IEEE 802.11p model is equal to −6.5 dB. A possible

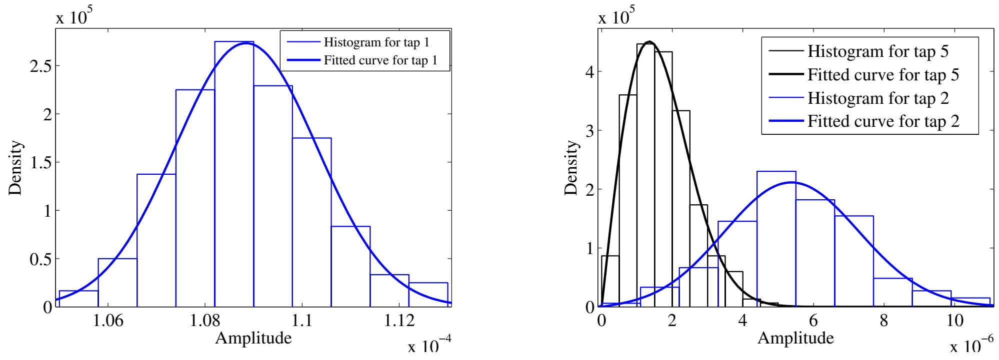

(a) (b)

Figure 5.17: Amplitude statistics for (a) tap 1 and (b) tab 2 and tab 5

explanation for this is the different highway environment in our measurement campaign. Considering also the tap gains below −29 dB we observe some later taps with higher gain, e.g., tap 9 with −32.9 dB. In Fig. 5.16 it can be seen that this gain is coming only from a few APDPs, at a delay of approx. 400 ns. This shows the temporal variation of the V2V radio channel, which is not reflected by the 10-tap delay IEEE 802.11p model. I will focus on this time variance in more detail in the following section, delay-Doppler spectra comparison.

An investigation of the amplitude distribution of the taps yielded a Rice distribution. The ratio of the gain in the LOS component to the gain in the diffuse component is called the Ricean K-factor. Figure 5.17 (a) presents a typical amplitude distribution over approx. 30 wavelengths for the first tap compared with a Rice distribution. We see that this Ricean shape fits very well to our amplitude distribution. In Fig. 5.17 (b) typical amplitude distributions for tap 2 and tap 5 are presented, where also a Ricean behavior is observed.

Table 5.3 presents the estimated *median* Ricean K-factor of our measurements. A high Ricean K-factor can be observed for tap 1, which is congruent with a strong LOS component in this tap. Also the value of 10.3 for the Ricean K-factor of tap 2 represents a tap with a dominant component. From tap 4 to 10 the Ricean K-factors are smaller than one, which can be interpreted by a more or less equally distributed gain of all arriving MPCs. The estimated Ricean K-factors are in the same range as in the IEEE 802.11p model. In Fig. 5.18 the cumulative distribution function (cdf) is shown. I can be see that there are considerably high Ricean K-factors in the first tap. Approx. 10 % of the Ricean K-factors are greater than 700.

Doppler Spectrum Comparison

I estimate the delay-Doppler spectrum using the Fourier transform (time $\overset{\mathcal{F}}{\leftrightarrow}$ Doppler) over a time duration of 71 ms (232 snapshots) and taking the sum of the magnitude squared of

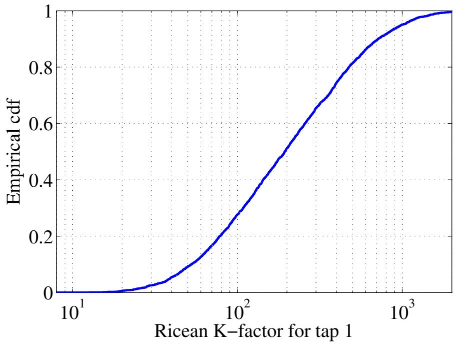

Figure 5.18: cdf of the Ricean K-factor for tap 1

the terms over all 16 single antenna element links of the measured 4 × 4 MIMO channel

$$P_{\text{DD}}[l,m] = \sum_{p=1}^{P} |\mathcal{F}\{h[k,l;p]\}|^2. \tag{5.17}$$

The duration of 71 ms is chosen because the WSS condition is fulfilled within that window. With our measurement setup and this Fourier transform interval a Doppler resolution of $\Delta\nu = 14\,\text{Hz}$ and a maximum resolvable Doppler frequency of $\nu_{\text{max}} = 1.6\,\text{kHz}$ can be achieved.

Figure 5.19 (a) shows an example of one delay-Doppler spectrum from a measurement with a speed of 90 km/h. A strong LOS component near a Doppler frequency of zero can be observed, which fits to the driving scenario where both vehicles are traveling in the same direction with approximately the same speed. Important are the two peaks at a delay of approx. 500 ns and a Doppler shift of approx. ±850 Hz. Peaks with these Doppler shifts were also found in all other delay-Doppler spectra at variant delays. A Doppler frequency of 850 Hz corresponds to a speed of 176 km/h, at our center frequency of 5.2 GHz, which is about twice the speed of our measurement vehicles. MPCs with this Doppler frequency result from a single bounced stationary scatterer in driving direction, above or next to the road, compare Fig. 5.8. Such scatterers can be overpasses or traffic signs, especially the latter ones have good reflection properties, because usually they are made of metal. The sign of this Doppler frequency depends on the relative position of the scatterer — in front or behind the measurement vehicles. Further two important peaks are observed at delays of approx. 150 ns and 300 ns and a Doppler shift of approx. 1370 Hz. These peaks are important, because in the IEEE 802.11p model no Doppler shifts greater than two times the vehicle's speed are modeled. In our measurements we found peaks with such a high Doppler shift, which should be included in a V2V channel model.

In order to make further comparisons with the IEEE 802.11p model I estimate an average delay-Doppler spectrum over one measurement run, as it is proposed in the standard. I would like to point out that such an averaged spectrum can not anymore be interpreted

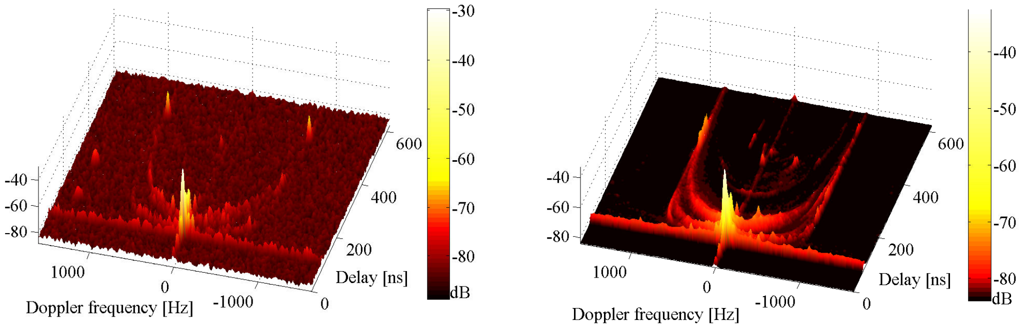

(a) (b)

Figure 5.19: (a) Delay-Doppler spectrum and (b) average delay-Doppler spectrum of a measurement with a speed of 90 km/h

as a delay-Doppler spectrum, because the WSSUS assumption is not fulfilled over this duration. I show that such an averaged spectrum does not reflect the time variance of a V2V radio channel that is an important characteristic of such a channel.

Figure 5.19 (b) presents the average delay-Doppler spectrum over one measurement run. As described above, the two peaks in Fig. 5.19 (a) at the Doppler frequencies of ±850 Hz are moving from larger delays to smaller delays over time. It is not possible to observe these single scatterers in the average delay-Doppler spectrum, because the peaks are blurred over the delay domain. Also the two peaks at the high Doppler frequency of 1370 Hz can not be found in the average delay-Doppler spectrum.

These differences between the short-time delay Doppler spectrum and the averaged spectrum are more prominent in the tap delay-Doppler spectra that are used in the IEEE 802.11p model. Each tap in the IEEE 802.11p model is described by one average delay-Doppler spectrum. For the calculation of the delay-Doppler spectra for each tap I take the mean of the delay-Doppler spectra over the 12 delay bins associated to each delay tap.

In Fig. 5.20 (a) and 5.20 (b) the short-time tap delay-Doppler spectra and the average tap delay-Doppler spectra over one measurement run are presented, respectively. The LOS peak near the Doppler frequency of zero is also present in the IEEE 802.11p model. By investigating the same four peaks as in the continuous delay-Doppler spectra some important differences can be seen. The two peaks in tap 9 in the short-time spectrum, Fig. 5.20 (a), can not be found with the same gain in the average spectrum, Fig. 5.20 (b), but there is one peak with approximately the same gain in tap 8. The other two peaks in tap 2 and tap 5 at a Doppler frequency of 1370 Hz are not anymore present in the average delay-Doppler spectra. I conclude that the 10-tap delay model from the IEEE 802.11p standard version D0.26 unfortunately does not reflect the time variance behavior of the radio channel. However, this would be most important in V2V scenarios.

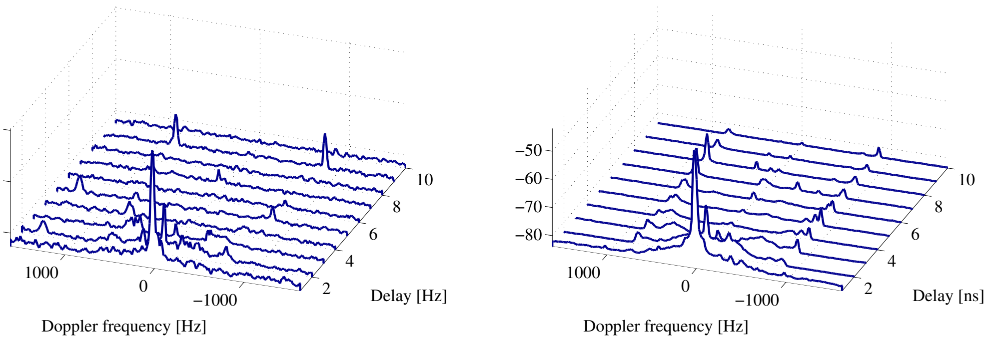

(a) (b)

Figure 5.20: (a) Tap delay-Doppler spectrum and (b) average tap delay-Doppler spectrum of a measurement with a speed of 90 km/h

5.4.4 Conclusions on the Proposed IEEE 802.11p Channel Model

Shorter impulse responses for the LUND'07 V2V measurements on the highway compared to the proposed ones by the IEEE 802.11p model were observed. The measured maximum significant delay is about one fifth of the maximum delay of the IEEE 802.11p model. This results also in a faster decrease of the tap gain. As in the IEEE 802.11p model it was found that a Rice distribution is the best approximation for the amplitude distribution for all taps. A large Ricean K-factor for the first tap indicates the existence of a strong LOS component in this tap. Later taps (tap 4 to tap 10) showed a Ricean K-factor less than 1. These results indicate that the IEEE 802.11p 10-tap delay model (version D0.26) does not reflect the time variant behavior of the channel. The statistical properties of vehicular channels change over time (violation of WSS assumption) and may show correlated fading for different delays due to several MPCs interacting with one-and-the-same object (violation of US assumption). These are specific characteristics of vehicular channels which are not adequately reproduced in standard tap delay models. Extensions to the standard tap delay model, in order to model vehicular radio channels, are presented in [5]. Consequently we developed a geometry-based stochastic MIMO V2V model considering this time variance [28].

6

IEEE 802.11p PHY Performance in Vehicular Scenarios

THE international standard IEEE 802.11p, which is part of the WAVE initiative, is intented for V2I and V2V traffic telematics applications. In order to evaluate the performance of this technology in real-world scenarios, we carried out a V2I PHY measurement campaign on a highway in Austria, see Sec. 4.2 for description. In this section I present important measures for possible improvements of the PHY and IEEE 802.11p site planning, e.g., maximum coverage range for one site (RSU) and maximum achievable data volume that can be transmitted passing one RSU. Further I investigate the dependency of coverage range and correctly received data volume on the packet length, data rate, Tx power, and vehicle speed. Since these are system measurements, the behavior of the radio channel cannot be investigated directly. Therefore the environmental effects (antenna height, wave propagation effects, traffic influence) are explained based on the measured Signal-to-Noise-Ratio (SNR) and Frame-Success-Ratio (FSR) together with the measurement-related videos, with the experience on the vehicular radio channel gained in the radio channel measurement evaluations described in Ch. 5.

In Sec. 6.1 I define the performance indicators that I use for the evaluation of this IEEE 802.11p PHY measurements. The environmental effects of the V2I link are discussed in Sec. 6.2. This section is divided in three parts, the effect of antenna height, important characteristics of wave propagation, and the influence of traffic on the system performance. In Sec. 6.3 I present the influence of the parameter settings at the transmitting RSU and the vehicle (OBU) speed on the performance indicators. Firstly the achievable coverage ranges are discussed, followed by the influence of selecting different packet lengths and data rates. Finally the dependency of the performance indicators on the vehicle speed is investigated.

6.1 Definition of Performance Indicators

I define the FSR as the number of OFDM frames $N_{\text{frame,corr}}$ that can be decoded with correct Cyclic Redundancy Check (CRC)-32 divided by the number of total transmitted frames $N_{\text{frame,Tx}}$ during a time interval

$$FSR = \frac{N_{\text{frame,corr}}}{N_{\text{frame,Tx}}}. \tag{6.1}$$

The *achievable range* d_{achiev} for the RSU is defined on the interval where the FSR is permanently above a certain threshold γ_{thresh}. Based on a first evaluation of the FSR over distance for all measurement runs, I chose two thresholds of $\gamma_{\text{thresh}} = 0.5$ and $\gamma_{\text{thresh}} = 0.25$. In Fig. 6.1 an example for the achievable range is depicted, where distance 0 m on the x-axis is the position of the RSU. Since we were using omni-directional RSU antennas, the achievable range for the RSU is the overall range before and after the RSU. As *total data volume* V_{total} I define the sum of all correctly received frames from the RSU multiplied by the packet length $V_{\text{total}} = N_{\text{frame,corr}} N_{\text{MSDU}}$. The *achievable data volume* V_{achiev} is calculated in the same way as the total data volume, but only the correct frames within the achievable range $d_{\text{achiev}}(\gamma_{\text{thresh}} = 0.25)$, are considered. Furthermore I define the *theoretical data volume* V_{theo} as the number of transmitted frames from the RSU, when the OBU was inside the achievable range $d_{\text{achiev}}(\gamma_{\text{thresh}} = 0.25)$, multiplied by the packet length $V_{\text{theo}} = N_{\text{frame,Tx}}(\in d_{\text{achiev}}(\gamma_{\text{thresh}} = 0.25)) N_{\text{MSDU}}$.

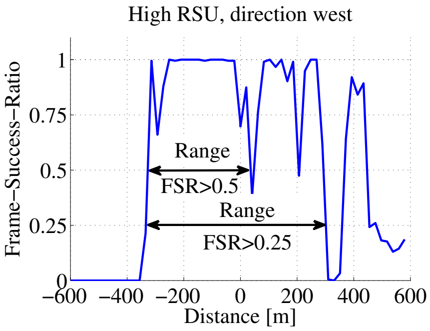

Figure 6.1: Definition of achievable range d_{achiev} for FSR>0.5 and FSR>0.25 (measurement example: high Tx power, $R_{\text{data}} = 3\,\text{Mbit/s}$, $N_{\text{MSDU}} = 1554\,\text{Byte}$, $v = 80\,\text{km/h}$)

6.2 Environmental Effects

In this section, I analyze the impact of environment effects on the measurement values, coverage range and the transmission throughput. I focus the attention on the antenna height, propagation effects that are caused by reflection, diffraction, focusing, and blocking of the electromagnetic wave propagation by objects between the RSU and the OBU. Furthermore, I investigate the impact of road traffic on the performance of the system.

6.2.1 Antenna Height

The antenna height influences the coverage range and the instantaneous throughput significantly. Figure 6.2 shows a typical SNR plot for a measurement run in direction west. The positions of the RSUs are at distance zero. Figure 6.2 (a) depicts the SNR for the high antenna location, whereas Fig. 6.2 (b) shows the case where the antenna was mounted next to the traffic lane.

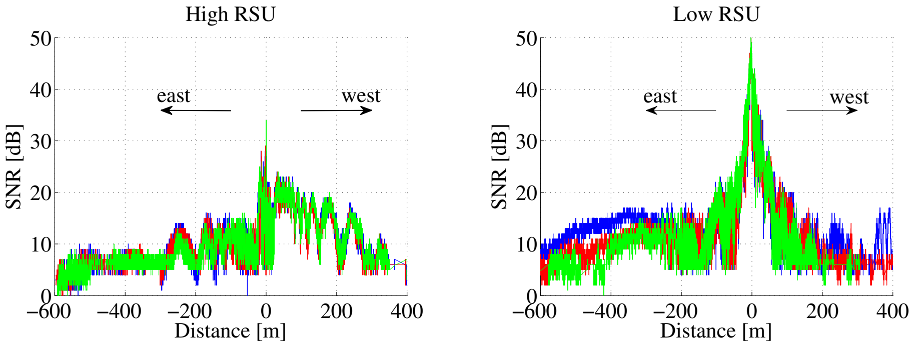

(a) (b)

Figure 6.2: SNR plot for vehicle driving west for (a) high RSU and (b) low RSU (high Tx power, $R_{\text{data}} = 3\,\text{Mbit/s}$, $N_{\text{MSDU}} = 0\,\text{Byte}$, $v = 80\,\text{km/h}$)

The Tx power was set to 15.5 dBm for the high RSU and 16 dBm for the low RSU. The SNR curve of the high RSU shows a typical large- and small-scale fading after passing the RSU location in direction west. Surprisingly, the average SNR values before passing the RSU are around 10 dB lower than the average SNR values after passing the RSU and the curve does not show the typical small-scale fading behavior. This behavior of the curve is caused by the antenna pattern and analyzed in further detail in Sec. 6.2.2. The maximum SNR values are around 30 dB. The SNR curve for the low RSU is peaky. Clearly, the peak SNR value is higher than for the high antenna setting and typically around 50 dB.

The coverage range depends on the antenna position and the direction of the measurement run. The maximum achievable range for the high RSU is 700 m for both driving directions. For the low RSU the maximum achievable range is 905 m driving in direction west and 500 m for direction east (all maximum ranges are achieved with $R_{\text{data}} = 3\,\text{Mbit/s}$).

The large difference between the maximum range for the low RSU is due to the blocking of the signal by the median strip of the highway and the traffic on the lanes between the RSU and the OBU. Since the vehicle was driving on the right lane with a speed of 80 km/h there is no lane between the vehicle and the RSU, when the vehicle is driving in direction west. Otherwise, when the vehicle is driving in direction east, there are three lanes between the vehicle and the RSU. The additional traffic on these lanes is blocking the transmission between RSU and OBU and these explains the large difference on the achievable range, based on the driving direction.

For higher-order modulation schemes the lower antenna position outperforms the high antenna position both in terms of peak coverage range and overall received data volume. The reason for this is the omni-directional antenna pattern in the horizontal plane. When the vehicle is close to the RSU, the antenna gain of the high RSU antenna (vehicle under the antenna) is much lower compared to the antenna gain of the low RSU antenna (vehicle next to the antenna in the horizontal plane). However, depending on the traffic situation, these peak values cannot be guaranteed.

For 64-QAM modulation schemes, the low antenna position can increase the overall transmitted data volume up to 2.5 times compared to the high antenna position. Figure 6.3 shows a comparison of the FSR for the 27 Mbit/s setting between low, Fig. 6.3 (a) and (b), and high RSU, Fig 6.3 (c) and (d). The most favorable conditions for this 64-QAM setting are low RSU and measurement direction west, where a FSR of 1 can be achieved in the vicinity of the gantry. The peak FSR of the high RSU has been measured below 0.8. However, the coverage range for the 27 Mbit/s setting is just some tenth of meters and therefore this high data rate setting is not recommended.

6.2.2 Propagation

Effects caused by the propagation of the electromagnetic waves are examined in the following. I observed an unexpected behavior in the FSR curves and drew conclusions by visual inspection of the measurement videos and the topology. Propagation effects close to the Tx, i.e., the antenna surrounding, and a bridge railing effect could be observed. Propagation effects close to the Tx cause the aforementioned SNR curve effect for the high RSU setting (see Fig. 6.2). The typical small-scale fading can be observed only in direction west. This behavior has a significant influence on the FSR that can be visualized for higher order modulation schemes. Figure 6.4 shows the FSR for the high RSU with modulation schemes 16-QAM (18 Mbit/s) and 64-QAM (24 Mbit/s and 27 Mbit/s). The surrounding of the antenna causes a destructive superposition of the electromagnetic waves and causes the SNR and throughput drop. Better signal quality can be measured towards west. Hence, the coverage range becomes unsymmetrical.

Figure 4.18 (a) illustrates the antenna mounting on top of the gantry and the metal

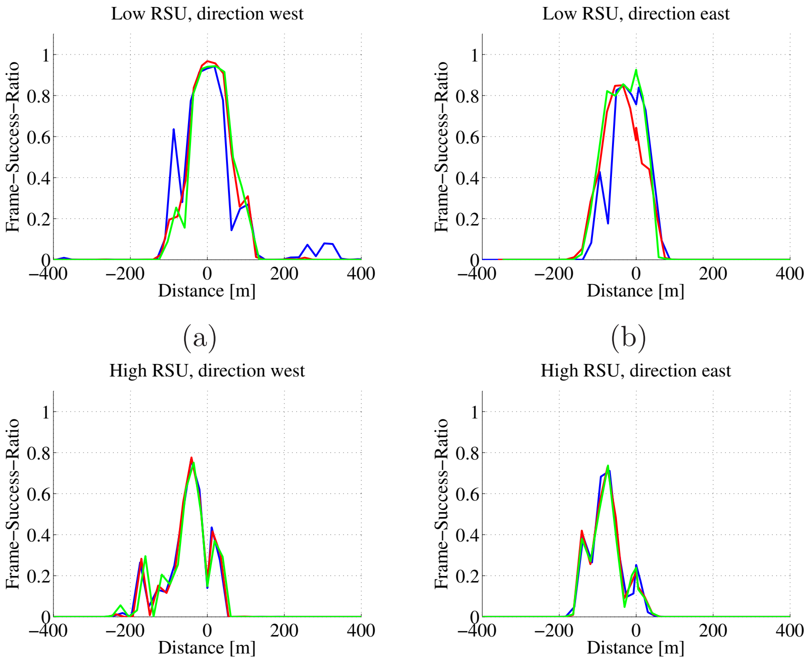

(a) (b) (c) (d)

Figure 6.3: FSR comparison for 64-QAM modulation for the low RSU (a) direction west and (b) direction east and for the high RSU (c) direction west and (d) direction east (high Tx power, $R_{\text{data}} = 27\,\text{Mbit/s}$, $N_{\text{MSDU}} = 0\,\text{Byte}$, $v = 80\,\text{km/h}$)

pillars that cause the propagation effect. Figure 6.4 shows the antenna pattern effect and the unsymmetrical coverage range.

Further an unexpected behavior of the FSR curve caused by a propagation effect approximately $0.7 - 1.2\,\text{km}$ after the low RSU in direction west, i.e., between the locations of the RSUs, was noticed. I observed additional peaky coverage intervals caused by the wave focusing and directing capabilities of the railings of the highway overpass, i.e., the second bridge in Fig. 4.20 (b). The bridge railing leads to additional coverage after the FSR has already dropped to zero. This phenomena can be observed when measuring the throughput in direction east.

Figure 6.5 illustrates the bridge railing effect caused by the second overpass. For the parameter settings at hand, in driving direction east the additional coverage starts about 1 km after passing the low RSU. The additional coverage interval has a maximum length of 250 m but is highly dependent on the traffic situation. Trucks can block the signal, see in Fig. 6.5 (a) and (b) in one of the three measurement runs. In direction west, additional coverage intervals caused by the bridge railing effect could be observed in certain situations and appear about $0.75 - 1\,\text{km}$ before passing the low RSU. The additional data volume received is negligible. However, if site planning is considered, this additional data volume must be considered as interference for the adjacent IEEE 802.11p

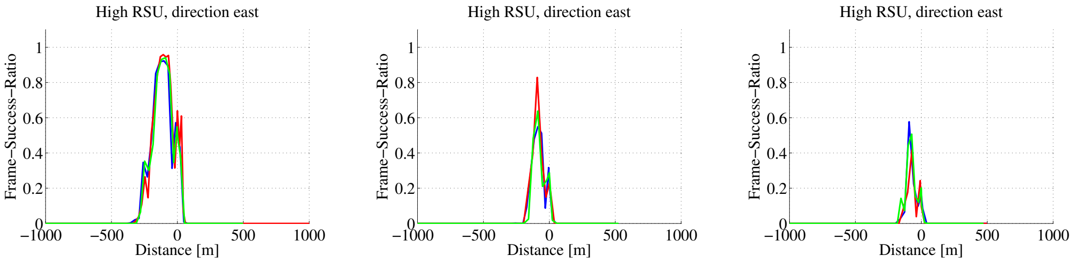

(a) (b) (c)

Figure 6.4: Antenna pattern effect at high RSU (a) 18 Mbit/s, (b) 24 Mbit/s, and (c) 27 Mbit/s (high Tx power, $N_{\text{MSDU}} = 200$ Byte, $v = 120$ km/h)

cells. Therefore, I recommend mitigating this effect, using additional structuring measures at the bridge railings.

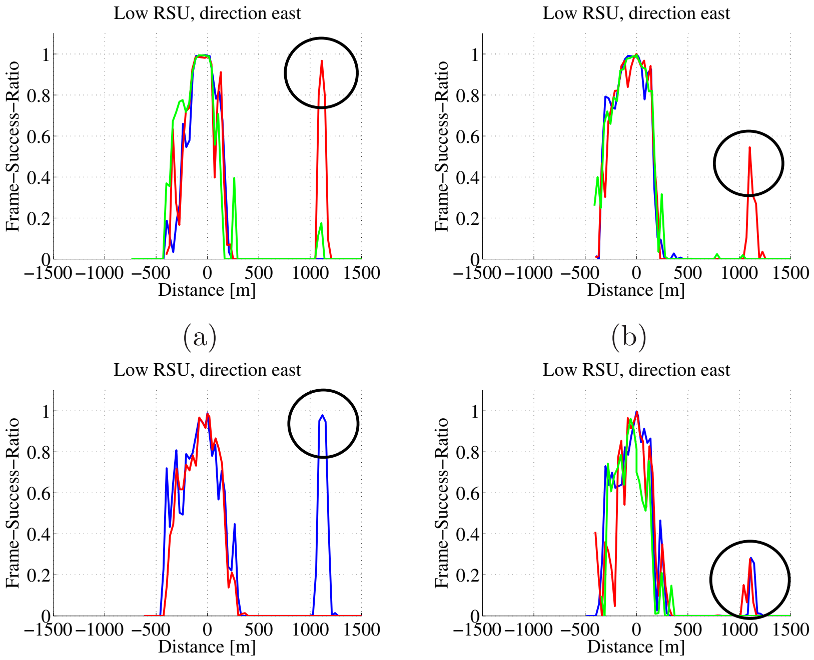

(c) (d)

Figure 6.5: Bridge railing effect of low RSU (a) 0 Byte, (b) 200 Byte, (c) 1554 Byte, and (d) 787 Byte (high Tx power, $R_{\text{data}} = 3$ Mbit/s, $v = 120$ km/h)

Figure 6.6 shows the front view during a measurement run in driving direction east. During this run, the car passed the second overpass, see Fig. 4.20 (b), and is entering an additional coverage interval since the traffic is not blocking the signals.

Table 6.1 lists the additional transmit data volume caused by the bride railing effect for the above measurement runs. In column one the parameter setting for this measurement run is shown, where the “E” stands for driving direction east and the number afterwards the repetition number for this setting. The relative received data volume is the number

Figure 6.6: Bridge (overpass Wattens Bahnhofstrasse), driving direction east

Table 6.1: Additional Tx data volume caused by bridge railing effect

Parameter setting	Relative received data volume	Received data volume
PS 2.1 E2	16 %	197 kB
PS 2.1 E3	2 %	21 kB
PS 2.3 E1	18 %	1214 kB
PS 2.3 E3	14 %	807 kB
PS 3.1 E2	8 %	283 kB
PS 2.5 E1	4 %	176 kB
PS 2.5 E2	4 %	176 kB

of frames received in the additional coverage interval divided by the total number of frames received from the RSU during a run. The received data volume is the number of frames received in the additional coverage interval multiplied by the packet length. The outstanding value listed in Tab. 6.1 occurred during the first measurement run with Parameter Setting (PS) 2.3, when almost one fifth of the overall data volume was received in the coverage extension window.

Finally, I investigate a drop in throughput, occurring in several measurement runs at the same geographical location, relatively close to the high RSU. The effect occurs in both driving directions. A conclusive explanation for this effect could not be found. However, this throughput drop could be caused by LOS blocking, by interference, or by the receiver hardware, which may not be able to equalize MPCs at low SNR. Figure 6.7 shows the FSR for several parameter settings, where the throughput drop is marked with a circle.

6.2.3 Traffic

The traffic has a severe influence on the successful transmission of the data. Depending on the traffic situation, moving objects (cars, vans or trucks) that are blocking the LOS between Tx and Rx cause severe performance differences. The instantaneous range, trans-

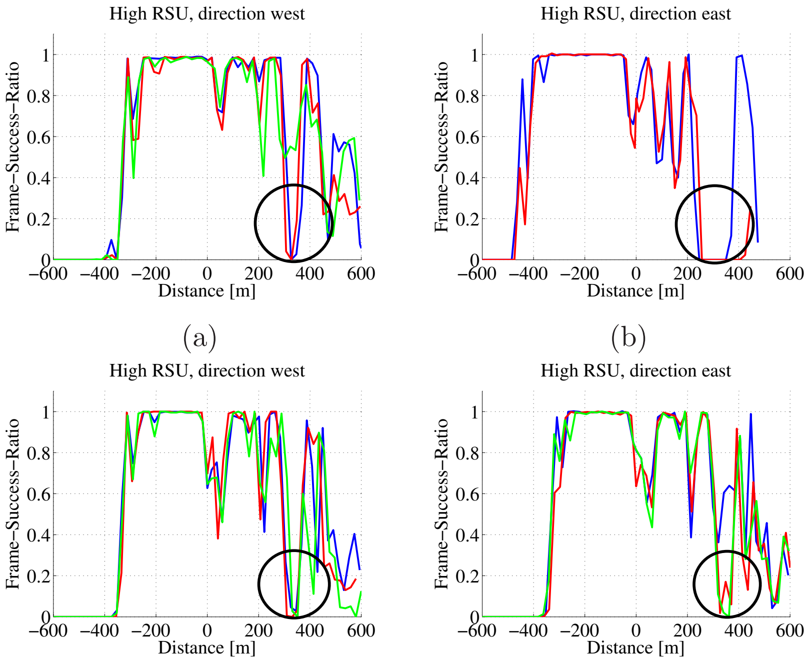

(a) (b)

(c) (d)

Figure 6.7: Throughput drop from the high RSU for (a) direction west and $N_{\mathrm{MSDU}} = 0\,\mathrm{Byte}$, (b) direction east and $N_{\mathrm{MSDU}} = 1554\,\mathrm{Byte}$, (c) direction west and $N_{\mathrm{MSDU}} = 1554\,\mathrm{Byte}$, and (d) direction east and $N_{\mathrm{MSDU}} = 787\,\mathrm{Byte}$ (high Tx power, $R_{\mathrm{data}} = 3\,\mathrm{Mbit/s}$, $v = 80\,\mathrm{km/h}$)

mit data volume and FSR of the measurement runs vary significantly. Figure 6.8 depicts a LOS blocking effect that can be observed for several measurement runs in direction west close to the low RSU. Clearly LOS blocking has a much larger influence on the performance at the low RSU. The antenna position, see Fig. 4.20 (a) is unfavorable. The FSR of different runs vary significantly where the blocking occurs, highlighted with the circles.

Depending on the instantaneous traffic situation, I observed that the FSR curve for a fixed parameter setting between the runs can vary significantly. In the following I compare two settings with identical data rate but different packet length and speed. Figure 6.9 (a) shows the FSR for the setting with the longest packet length and the higher speed.

It can be observed that the FSR fluctuates stronger in the case of the long packet length and the high speed. In addition to a less beneficial traffic situation the packet length and the higher speed causes a higher packet loss. For runs with 120 km/h, we were driving on the left lane.

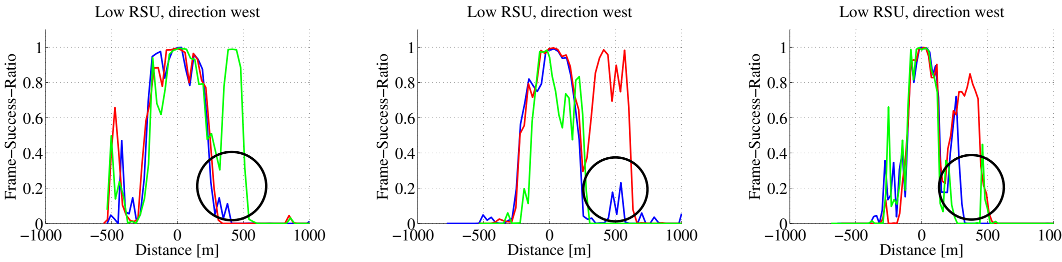

(a) (b) (c)

Figure 6.8: LOS blocking for the low RSU caused by the traffic (a) $R_{\text{data}} = 3\,\text{Mbit/s}$ and $v = 120\,\text{km/h}$, (c) $R_{\text{data}} = 6\,\text{Mbit/s}$ and $v = 120\,\text{km/h}$, (e) $R_{\text{data}} = 12\,\text{Mbit/s}$ and $v = 80\,\text{km/h}$ (high Tx power, direction west, $N_{\text{MSDU}} = 200\,\text{Byte}$)

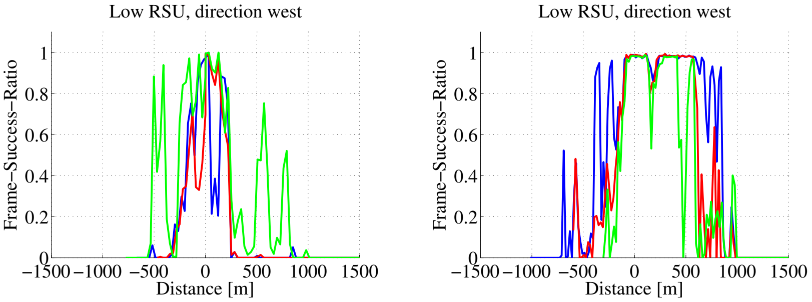

(a) (b)

Figure 6.9: Comparison of FSR depending on packet length and speed for the low RSU (a) $N_{\text{MSDU}} = 1554\,\text{Byte}$ and $v = 120\,\text{km/h}$ and (b) $N_{\text{MSDU}} = 0\,\text{Byte}$ and $v = 80\,\text{km/h}$ (high Tx power, $R_{\text{data}} = 3\,\text{Mbit/s}$, direction west)

6.2.4 Conclusions of Environmental Effects

Investigating the effect of the antenna height it was found that the low antenna position outperforms the high antenna position both in terms of maximum achievable coverage range and transmitted data volume just in one driving direction (direction west). However, the range of the low antenna position strongly depends on the traffic situation. Therefore, for vehicular safety communication the high RSU setting should be favored.

Considering the propagation effects, it turned out that the metal pillars of the gantry lead to a unsymmetrical antenna pattern (that is omni-directional, considering just the antenna) and therefore also to a unsymmetrical coverage area. Such an influence has to be taken into account for a IEEE 802.11p site planning. Furthermore, certain metallic structures on the road can cause significant focusing of the waves along the street, thus leading to a strongly increased coverage range of the RSU. This increased coverage is very peaky, hence it cannot be used for effective coverage extension. Thus, for site planning, this effect must be considered as additional interference, which has to be taken into account between neighboring RSUs. It seems that the current receiver implementation cannot cope

Table 6.2: Achievble ranges with high RSU at speed 80 km/h

	$P_{\text{Tx}} = 15.5\,\text{dBm}$		$P_{\text{Tx}} = 10.5\,\text{dBm}$	
	$\gamma_{\text{thresh}} = 0.5$	$\gamma_{\text{thresh}} = 0.25$	$\gamma_{\text{thresh}} = 0.5$	$\gamma_{\text{thresh}} = 0.25$
3 Mbit/s (east)	525 m	601 m	370 m	425 m
3 Mbit/s (west)	550 m	698 m	245 m	413 m
27 Mbit/s (east)	45 m	112 m	-	-
27 Mbit/s (west)	62 m	76 m	-	-

with a large number of MPCs at low SNR. This leads to unexpected throughput drop.

I identified the road traffic as a main factor that influences the performance of the IEEE 802.11p system. I observed strong shadowing effects caused by trucks obstructing the LOS for the low RSU. This leads to strongly fluctuating performance of the system, especially for receiver "challenging" settings, such as long packet length and increased speed.

6.3 Parameter Setting Effects

6.3.1 Range

Table 6.2 shows the achievable ranges for the high RSU at a vehicle speed of 80 km/h and a packet length of 0 Byte. The second and third columns show the achievable ranges for the thresholds $\gamma_{\text{thresh}} = 0.5$ and $\gamma_{\text{thresh}} = 0.25$ for high Tx power of 15.5 dBm. In columns four and five the achievable ranges for low Tx power of 10.5 dBm are presented. In the following explanations I focus on the maximum achievable range, based on the threshold of $\gamma_{\text{thresh}} = 0.25$.

Considering the high Tx power a maximum achievable range of approximately 700 m in the case of the smallest possible data rate of 3 Mbit/s can be observed. With the highest possible data rate of 27 Mbit/s the achievable range decreases to a value of about 100 m. The maximum achievable range with low Tx power of 10.5 dBm is about 400 m with data rate of 3 Mbit/s. In the case of a data rate of 27 Mbit/s the frame success ratio is always smaller than 0.25 and therefore no range can be given.

Table 6.3 shows the achievable ranges for the low RSU. With the data rate of 3 Mbit/s and high Tx power of 16 dBm the maximum achievable range is about 850 m. The results depend strongly on the driving direction. As explained in Sec. 6.2.1 there are more or less lanes between the RSU and the OBU, depending on the driving direction, which results in blocking or non-blocking of the LOS. This effect in the range is not observed for the high RSU, because in that case the RSU antenna is mounted above the vehicles. In Sec. 6.3.2 further influence of the driving direction on the range considering the low RSU can be

Table 6.3: Achievble ranges with low RSU at speed 80 km/h

	$P_{\text{Tx}} = 16\,\text{dBm}$		$P_{\text{Tx}} = 7.5\,\text{dBm}$	
	$\gamma_{\text{thresh}} = 0.5$	$\gamma_{\text{thresh}} = 0.25$	$\gamma_{\text{thresh}} = 0.5$	$\gamma_{\text{thresh}} = 0.25$
3 Mbit/s (east)	325 m	441 m	177 m	202 m
3 Mbit/s (west)	782 m	865 m	216 m	237 m
27 Mbit/s (east)	95 m	146 m	18 m	85 m
27 Mbit/s (west)	117 m	160 m	46 m	88 m

found.

With the low Tx power the maximum achievable range at a data rate of 3 Mbit/s is between 200 m and 250 m. At a data rate of 27 Mbit/s the achievable range is about 150 m with high Tx power and smaller than 100 m in the case of low Tx power. The effect of driving direction is not so high in these cases. One possible explanation is that the probability that other vehicles are blocking the transmission is lower, when the coverage area is smaller, as in the case of higher data rate and/or lower Tx power.

6.3.2 Packet Length

Figure 6.10 shows the achievable ranges for high Tx power, a data rate of 3 Mbit/s and a vehicle speed of 80 km/h for different packet lengths (0 Byte, 200 Byte, 787 Byte, and 1554 Byte).

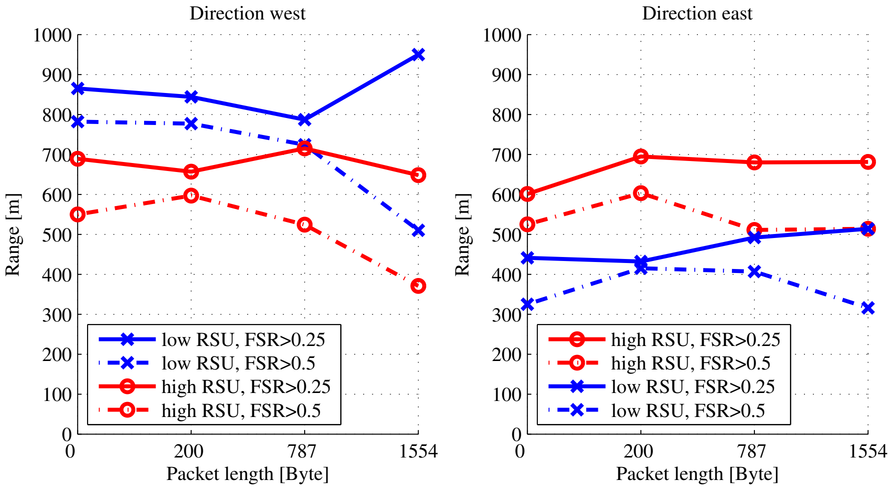

(a) (b)

Figure 6.10: Achievable range for high Tx power, $R_{\text{data}} = 3\,\text{Mbit/s}$ and $v = 80\,\text{km/h}$, (a) direction west and (b) direction east

The blue solid line in Fig. 6.10 (a) shows the range of the low RSU, based on the $\gamma_{\text{thresh}} = 0.25$. The maximum value of about 950 m is achieved at a packet length of

1554 Byte. When the vehicles are driving in direction west on the right lane, as it is the case with a speed of 80 km/h, the achievable range is always larger with the low RSU. Considering driving direction east the high RSU achieves larger ranges compared to the low RSU. The reason for this is, as mentioned in Sec. 6.2.1 that there are three lanes between the RSU and the OBU, in the case of driving in direction east. The traffic on these lanes is strongly influencing the transmission with the low RSU. Considering the range curves for the high RSU in Fig. 6.10 there is no noticeable difference between the driving directions. The achievable range, for $\gamma_{\text{thresh}} = 0.25$, is in both cases between 600 m and 700 m. This means that the driving direction has no influence, considering the high RSU.

In all four cases, high/low RSU and driving direction, there is no influence of the packet length on the achievable range, for $\gamma_{\text{thresh}} = 0.25$, observed. Only in the case of the achievable range, for $\gamma_{\text{thresh}} = 0.5$, there is a slight trend of decreasing range with increasing the packet length. This is because in the case of larger packet lengths, the FSR over distance is fluctuating stronger. If it drops down below the value of 0.5, whether only for a short time, this sets the achievable range for $\gamma_{\text{thresh}} = 0.5$. For this reason this effect does not influence the achievable range for $\gamma_{\text{thresh}} = 0.25$.

Figure 6.11 shows the total correctly received data volume for the high and low RSU, when the vehicle is driving in direction west, Fig. 6.11 (a), and for the high and low RSU, when the vehicle is driving in direction east, Fig. 6.11 (b), for different packet length. As mentioned in Sec. 6.1 the total data volume is calculated by the multiplication of the number of all correct received OFDM frames with the packet length. Since this total transmitted data volume is zero for the case of packet length 0 Byte, it is not included in this figure.

This total data volume is increasing with increasing packet length. For the high RSU the total data volume is increasing from 6 MB (for $N_{\text{MSDU}} = 200$ Byte) to 11 MB (for $N_{\text{MSDU}} = 1554$ Byte), for both driving direction cases. As for the range investigation, mentioned above, the driving direction has no influence on the total data volume, considering the high RSU. Also the total data volume, considering the low RSU, shows the same driving direction behavior as for the range investigation. In the case of driving in direction west the total data volume is larger for the low RSU compared to the high RSU. It increases from 7 MB (for $N_{\text{MSDU}} = 200$ Byte) to 14 MB (for $N_{\text{MSDU}} = 1554$ Byte). For the opposite driving direction (east), the total data volume for the low RSU is smaller than for the high RSU. It increases from 4 MB to 7 MB.

Figure 6.12 shows a comparison of the achieved data volume and the theoretical possible data volume for high Tx power, a data rate of 3 Mbit/s and a vehicle speed of 80 km/h. Different packet lengths of 200 Byte, 787 Byte and 1554 Byte are considered. As described in Sec. 6.1 these data volumes are calculated inside the achievable range with

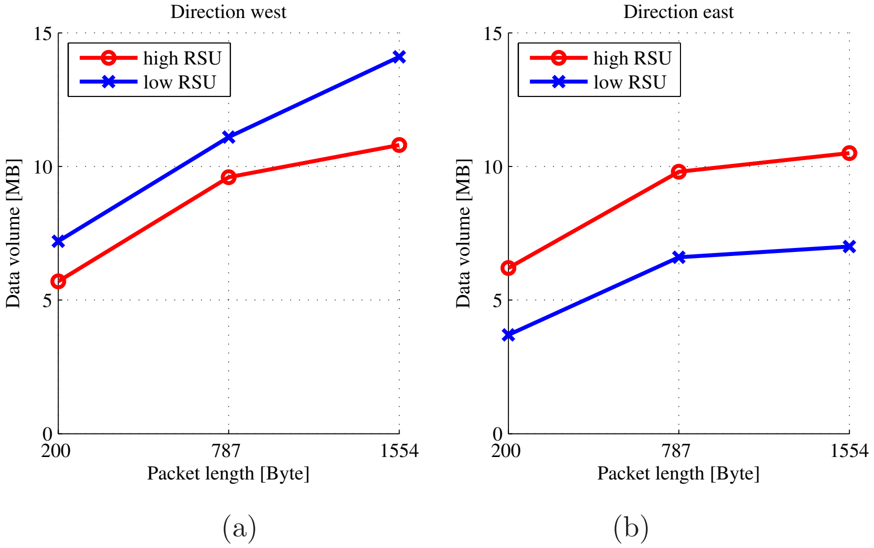

(a)

(b)

Figure 6.11: Total data volume for high Tx power, $R_{\text{data}} = 3\,\text{Mbit/s}$ and $v = 80\,\text{km/h}$, (a) direction west and (b) direction east

$\gamma_{\text{thresh}} = 0.25$.

Except of the achieved and theoretical data volume for the case low RSU, driving direction west, the data volumes are increasing with increasing packet length. One major difference in comparison with the total data volume, Fig. 6.11, and achievable ranges, Fig. 6.10, is that the achieved data volume as well as the theoretical volume, from the low RSU is below that one from the high RSU, considering driving direction west. The reason of this is that there are considerable contributions of correct received OFDM frames after the FSR dropped down below 0.25.

A further important result is the difference between theoretical data volume and achieved data volume. This result shows, how much data is lost during the transmission period. For driving direction east this difference is increasing with increasing the packet length, 0.9 MB, 2 MB, 2.5 MB, considering the high RSU and 1 MB, 1.9 MB, 2 MB, considering the low RSU, for packet lengths of 200 Byte, 787 Byte, and 1554 Byte. This means that the loss of data is higher, if the packets are longer. In the case of driving direction west, we cannot observe this behavior. The data volume difference considering the high RSU is 0.8 MB, 1.9 MB, 1.6 MB and considering the low RSU 1 MB, 1.9 MB, 1.8 MB again for packet lengths of 200 Byte, 787 Byte and 1554 Byte.

6.3.3 Modulation and Coding Scheme

Figure 6.13 shows the achievable ranges for high Tx power, a packet length of 200 Byte and a vehicle speed of 120 km/h over all possible data rates defined in IEEE 802.11p (3 Mbit/s - 27 Mbit/s). The modulation scheme and coding rate for each data rate is shown in

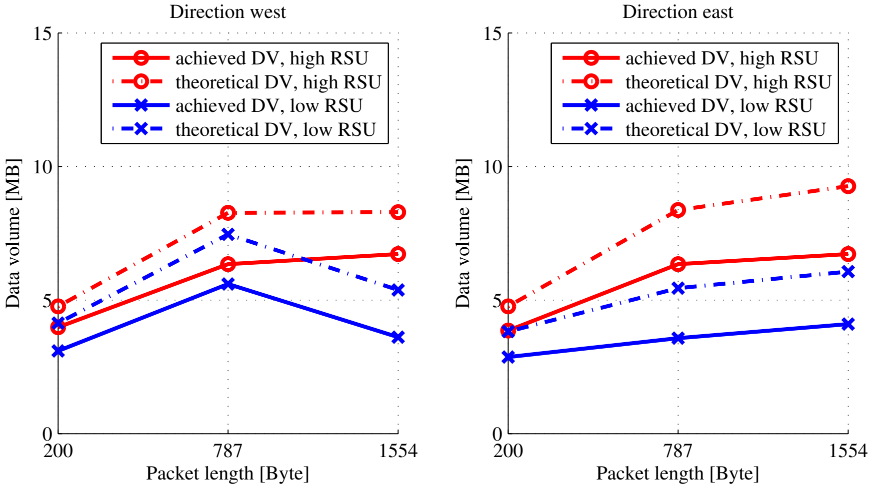

(a) (b)

Figure 6.12: Comparison of achieved and theoretical data volume (DV) for high Tx power, $R_{\text{data}} = 3\,\text{Mbit/s}$ and $v = 80\,\text{km/h}$, (a) direction west and (b) direction east

Tab. 4.6.

A decreasing range with increasing data rate, except in one situation for the low RSU, driving direction west from 3 Mbit/s to 4.5 Mbit/s, can be observed. This exception is explainable with heavier traffic in the 3 Mbit/s case compared with the 4.5 Mbit/s case. The achievable range, when the vehicle is driving in direction west, is going from more than 700 m, at low data rates, down to less than 100 m, at high data rates. When the vehicle is driving in direction east, the curves show the same behavior, but especially the ranges for the low RSU are smaller, about 550 m at 3 Mbit/s and about 150 m at 27 Mbit/s.

Figure 6.14 shows the total correct received data volume for high Tx power, a packet length of 200 Byte and a vehicle speed of 120 km/h over all possible data rates. The highest data volume of about 6.1 MB is achieved with the high RSU, when the vehicle is driving in direction west at a data rate of 9 Mbit/s. The data volume over the data rate for the high RSU shows the same behavior for both directions. When the vehicle is driving in direction east, the maximum data volume of about 5.4 MB is achieved at data rates 6 Mbit/s and 9 Mbit/s. Both data rates use Quadrature Phase Shift Keying (QPSK) modulation with different coding rates.

The explanation of the behavior of the total data volume curves over data rate is the following. The total data volume is increasing with increasing data rate, because more data can be transmitted in the same time. This is the reason, why the data volume is increasing at lower data rates. But if the data rate is increased, higher modulation schemes are used, and therefore more errors occur. This is the reason, why the data volume is decreasing after a specific data rate.

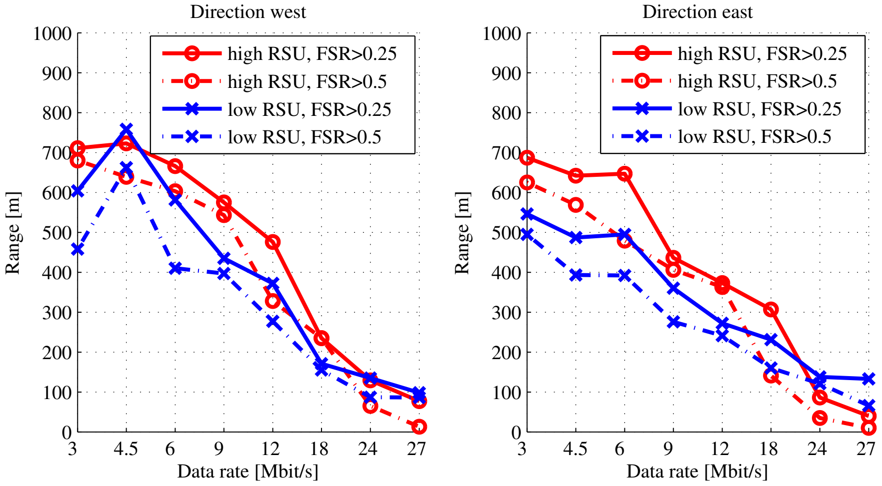

(a) (b)

Figure 6.13: Achievable range for high Tx power, $R_{\text{data}} = 3\,\text{Mbit/s}$ and $v = 120\,\text{km/h}$, (a) direction west and (b) direction east

The low RSU achieves the maximum data volume of 5.7 MB at a data rate of 4.5 Mbit/s, when the vehicle is driving in direction west, and the maximum data volume of 3.8 MB at a data rate of 6 Mbit/s, when the vehicle is driving in direction east. In general the achieved total data volume of the low RSU is always smaller than the data volume of the high RSU. Only at high data rates, 24 Mbit/s and 27 Mbit/s, the low RSU achieves a higher data volume compared with the high RSU, but this data volume is still below 2 MB.

In Fig. 6.15 a comparison of theoretical data volume and achieved data volume inside the achievable range over data rate is plotted. The difference between theoretical data volume and achieved volume is between 0.8 MB and 2.5 MB. No trend can be observed that this difference is higher at lower data rates or higher data rates. The reason why the theoretical data volume is decreasing at higher data rates is because this data volume is calculated inside the achievable range and this range is decreasing at higher data rates, see Fig. 6.13.

The achieved data volumes for all four cases, high/low RSU and driving direction west/east, show the same behavior as the total data volume, see Fig. 6.14. Also the maxima are achieve at the same data rates, 6 Mbit/s and 9 Mbit/s for the high RSU and 4.5 Mbit/s and 6 Mbit/s for the low RSU.

6.3.4 Vehicle Speed

In this section I investigate the difference in achievable range and total correct received data volume using two different vehicle speeds, 80 km/h and 120 km/h. Fig. 6.16 shows

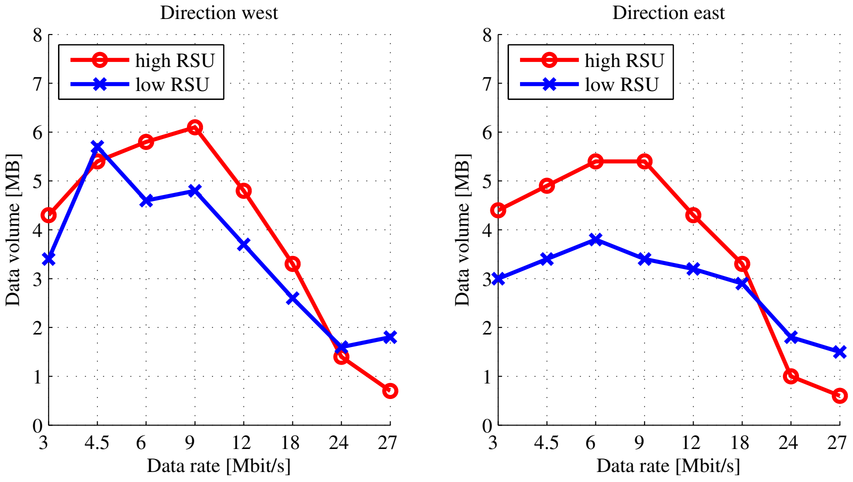

(a) (b)

Figure 6.14: Total data volume for high Tx power, $R_{\text{data}} = 3\,\text{Mbit/s}$ and $v = 120\,\text{km/h}$, (a) direction west and (b) direction east

the achievable ranges, for $\gamma_{\text{thresh}} = 0.25$, for high Tx power, and a data rate of 3 Mbit/s. No influence of the speed on the achievable range can be seen. Also the driving direction has no influence on the achievable range for the high RSU. The range is always about 700 m.

Considering the low RSU I observe different ranges for different speeds. The reason for this difference is not the speed of the vehicle, but the lane, where the vehicle is driving. When the vehicle is driving in direction west, it drives on the right lane with speed 80 km/h and on the left lane with speed 120 km/h. Driving on the left lane means that there is one lane between the RSU and the OBU. The traffic on this lane is blocking the transmission from the RSU and therefore the achievable range is smaller. When the vehicle is driving in direction east there are either two lanes between the OBU and the RSU (120 km/h) or three lanes between them (80 km/h). The difference of two or three lanes between OBU and RSU does not have an influence on the achievable range.

Figure 6.17 shows the total correct received data volume for high Tx power and a packet length of 200 Byte. In Fig. 6.17 (a) (high RSU) a smaller total data volume for the higher speed can be observed. This behavior is similar for both driving directions. The average difference of total data volume between high speed and low speed is 2.5 MB. The main reason for this difference is that with the higher speed, the vehicle is passing the RSU faster. In this case there is less time to transmit data and therefore the total data volume is smaller.

Considering the low RSU the lane where the vehicle is driving has an additional influence on the total data volume. The lower total data volume, because of the higher speed, together with the lower total data volume, because the vehicle is driving on the

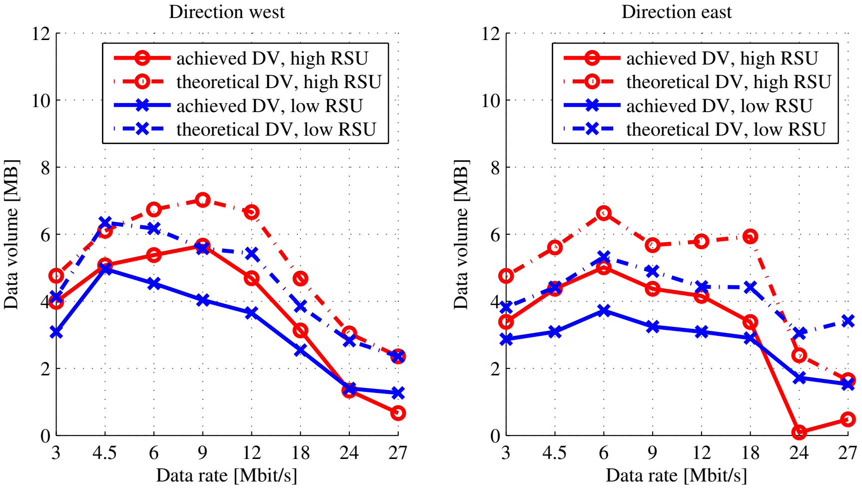

(a) (b)

Figure 6.15: Comparison of achieved and theoretical data volume (DV) for high Tx power, $R_{\text{data}} = 3\,\text{Mbit/s}$ and $v = 120\,\text{km/h}$, (a) direction west and (b) direction east

left lane, results in an average difference of about 6 MB, for driving direction west. When the vehicle is driving in direction east this averaged difference is much smaller, 1.6 MB, because the driving lane has not so much influence on the data volume.

Figure 6.18 shows the achievable range, for $\gamma_{\text{thresh}} = 0.25$, for high Tx power and a packet length of 200 Byte, considering different data rates. As mentioned above, Fig. 6.16, no influence of the speed on the achievable range for the high RSU can be observed. In this case the achievable range for driving direction west is even slightly larger for the higher vehicle speed. In Fig. 6.18 (a) (low RSU) again the effect of the driving lane can be observed. Driving on the right lane in direction west, which is the case with speed 80 km/h, yields the largest achievable ranges.

Figure 6.19 shows the total correct received data volume for high Tx power and a packet length of 200 Byte. The same behavior as described for total data volume vs. packet length investigation, see Fig. 6.17, can be observed. Similar data volume differences in the case of the high RSU are observed with an average value of 1.9 MB. The total data volume for the lower speed is higher. For the low RSU the driving direction west yields an average difference of data volume of 3.4 MB for the two different speeds. Remember that the driving lane has an additional influence. For driving direction east the total data volume difference is smaller, 1.7 MB.

6.3.5 Conclusions of Parameter Setting Effects

The maximum achievable range considering the high RSU is about 700 m (at $R_{\text{data}} = 3\,\text{Mbit/s}$ and $P_{\text{Tx}} = 15.5\,\text{dBm}$). Contrarily the achievable range decreases to about 100 m

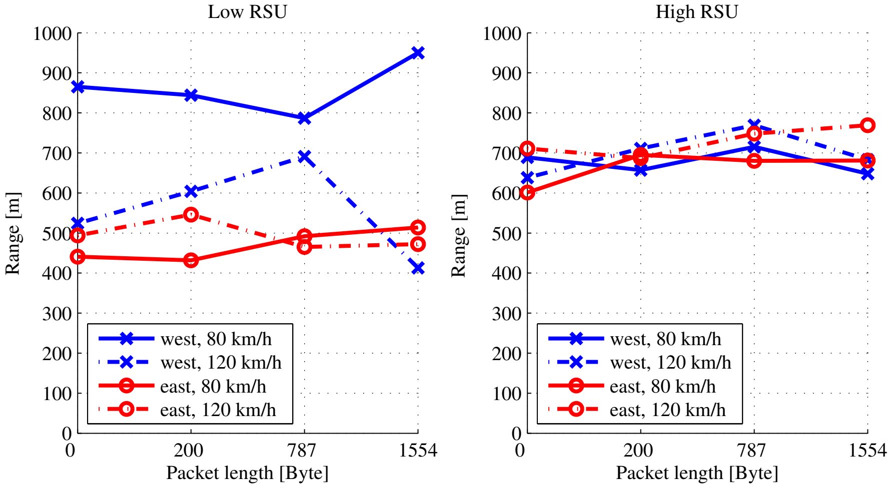

(a) (b)

Figure 6.16: Achievable ranges ($\gamma_{\text{thresh}} = 0.25$) for high Tx power and $R_{\text{data}} = 3\,\text{Mbit/s}$, (a) low RSU and (b) high RSU

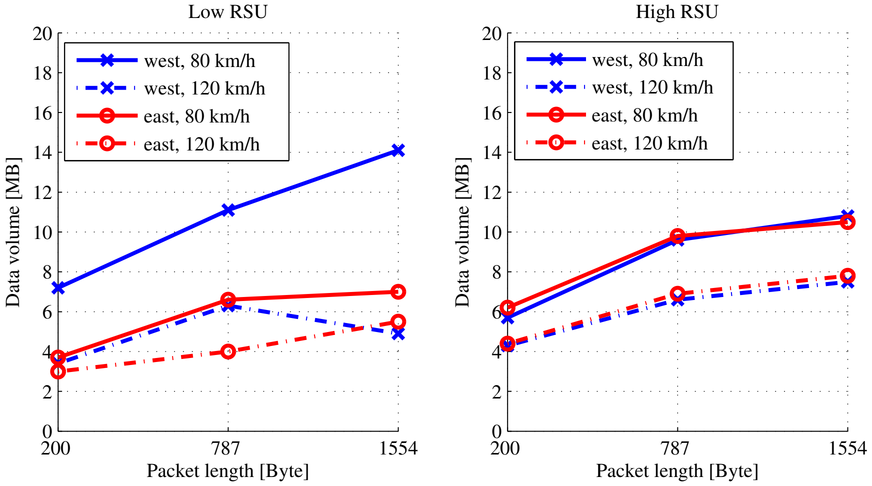

(a) (b)

Figure 6.17: Total data volume for high Tx power and $R_{\text{data}} = 3\,\text{Mbit/s}$, (a) low RSU and (b) high RSU

using a data rate of 27 Mbit/s. The FSR is always below 0.25 for the low Tx power and the highest data rate and therefore no achievable range can be calculated. In the case of the low RSU the maximum achievable range can be higher, up to 850 m, compared to the case of the high RSU, but depends strongly on the amount of traffic. The reason of this larger achievable range is because of the omni-directional antenna pattern in the horizontal plane.

Investigations of different packet length (with $v = 80\,\text{km/h}$ and $R_{\text{data}} = 3\,\text{Mbit/s}$)

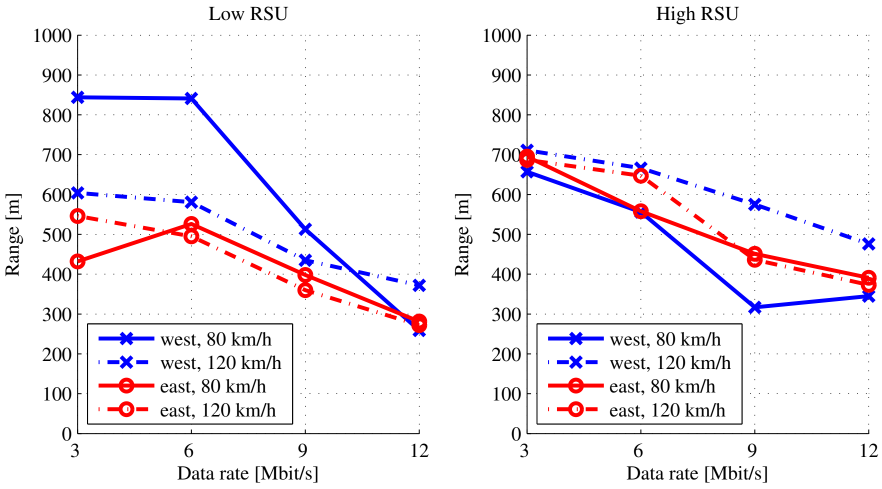

(a) (b)

Figure 6.18: Achievable ranges ($\gamma_{\text{thresh}} = 0.25$) for high Tx power and $N_{\text{MSDU}} =$ 200 Byte, (a) low RSU and (b) high RSU

showed no influence on the achievable range, for $\gamma_{\text{thresh}} = 0.25$. The achievable ranges, for $\gamma_{\text{thresh}} = 0.5$, are slightly decreasing with increasing packet lengths. Considering the low RSU, the achievable ranges and total data volume strongly depends on the driving direction. When the vehicle is driving in direction west, the achievable ranges and total data volumes are larger in the low RSU case compared with the high RSU. For driving direction east it is the other way around. In all cases the total correct received data volume is increasing with increasing packet length.

Considering different data rates, the achievable range is decreasing with increasing data rate. The maximum range is about 700 m at a data rate of 3 Mbit/s and drops down to a value of less than 100 m at a data rate of 27 Mbit/s. The maximum correct received data volume is achieved at low data rates of 4.5 Mbit/s, 6 Mbit/s and 9 Mbit/s. These data rates are using Binary Phase Shift Keying (BPSK) and QPSK modulation.

There is no influence from the speed of the vehicle on the achievable range observed. Only in the case of the low RSU and driving direction west the lower speed yields a higher range compared to the higher speed. The reason for this is not the difference in speed, but the lane where the vehicle is driving. The vehicle is driving on the right lane with the lower speed and on the left lane with the higher speed. Driving on the left lane means that there is a lane between OBU and RSU and additional blocking of the transmission from the traffic on this lane.

Considering the total correct received data volume, there is a difference between different speeds observed. At the high RSU a total data volume of 2.2 MB larger in averaged could be achieved with the lower speed compared to the higher speed. The high RSU

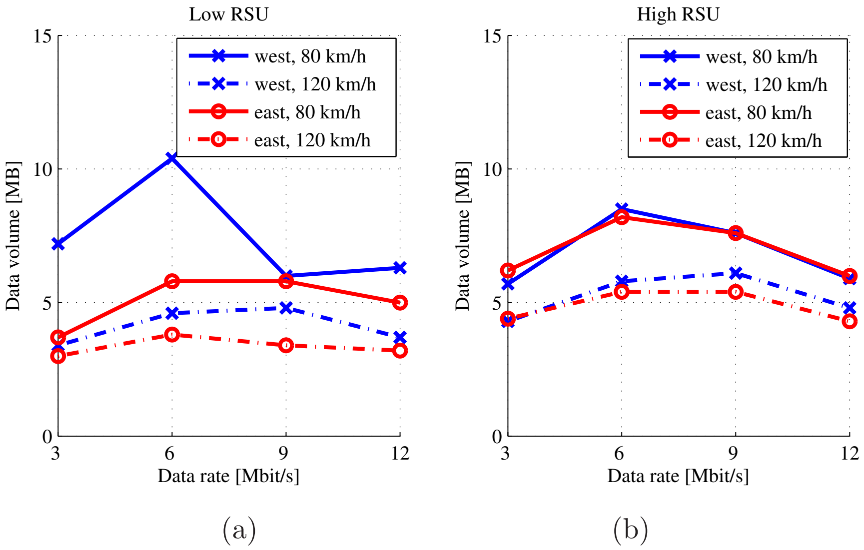

Figure 6.19: Total data volume for high Tx power and $N_{\mathrm{MSDU}} = 200\,\mathrm{Byte}$, (a) low RSU and (b) high RSU

gives the more meaningful result, because it does not include the effect on which lane the vehicle is driving. The main reason for this difference is that the vehicle is passing the RSU faster, when the speed is higher and therefore there is less time, in order to transmit data.

7

Conclusions

In this thesis I give an overview about the theory of time-variant radio channels. One of the most important concepts describing a time-variant non-WSSUS radio channel is the LSF, which can be seen as a time- and frequency-variant scattering function. The characterization and modeling of radio channels is based on extensive channel measurement campaigns. For this reason I spend one main part of my thesis describing two vehicular radio channel measurement campaigns, which we carried out in 2006 and 2009, respectively. Vehicular measurement campaigns have different requirements compared with stationary measurement campaigns. This has to be considered during the planning of such vehicular campaigns, e.g., mobile power supply, limited space in vehicles, location logging, documentation (with videos) of the changing environment and traffic. Based on these channel measurements I explain the methodology of the characterization of time-variant vehicular radio channels, with respect to the LSF.

Beside the discussion of vehicular radio channel measurement campaigns and the characterization of the radio channel, the second main part of my thesis is focused on system performance investigations for vehicular communications. Similar to the channel description I separated this system performance part in a detailed explanation of a measurement campaign and in one part for the evaluation of the measurements.

In the following I present the main conclusions from the vehicular radio channel characterization and vehicular system performance evaluation.

7.1 Radio Channel Characterization

We developed pathloss models for four different scenarios, where V2V communication systems are expected to be useful: rural, highway, urban, and suburban. Regarding the rural environment a two-ray propagation model showed the best congruence with our measurement results. This is reasonable since the environment provides few scatterers, which makes the LOS component and the ground reflection dominant. The pathloss of the other three environments is modeled with a classical power law model. Because of heavier traffic in this scenarios and the existence of more scatterers (buildings, traffic signs, bridges) more MPCs appear and the ground reflection is not dominant anymore. An interesting result is that the observed pathloss exponents are smaller than 2, which is the exponent of free space propagation. This effect can be caused by waveguiding effects.

The concept of LSF estimation considers a quasi-static radio channel, which means that there exist specific (limited in time and frequency) regions, where the channel can be assumed as non-WSSUS. This quasi-static behavior of the radio channel is confirmed by our measurements. Investigations showed that the region in time, the stationarity time, notably depends if the vehicles are driving in convoy or in opposite directions. For a highway environment the stationarity time is very short, when the vehicles are traveling in opposite directions, $T_{\text{stat}} = 23\,\text{ms}$. For the same environment, but with vehicles driving in the same direction, the stationarity time is much larger, $T_{\text{stat}} = 1479\,\text{ms}$.

The time-varying APDP and DSD were used in order to describe the MPCs. The measurements from the first measurement campaign (LUND'07) always showed a strong LOS component. The chosen scenarios — same direction and opposite direction in rural, highway, urban, and suburban environments and the height of the antennas (2.4 m) — were the reasons for it. In the second measurement campaign, we focused on more safety-critical applications and observed weaker obstructed LOS components in several situations, e.g., vehicles entering intersections; one vehicle is entering the highway on an entrance ramp, while the other vehicles is driving on the highway; trucks between the vehicles. An important finding is that the most significant scatterers are traffic signs, trucks, and bridges. Other cars do not significantly contribute to the multipath propagation. One reason is that we used realistic vehicular antennas mounted on the roof of the measurement cars and their resulting antenna pattern. Comparing the results from different intersections, we noted that in the absence of the LOS component, the coverage is dependent on the availability of significant scatterers such as buildings, which may account for a large fraction of the received power.

In an early version of the draft standard IEEE 802.11p a tap delay model is specified for vehicular communications. I compared the model parameters and found that a Rice distribution is the best approximation for the amplitude distribution for all taps, as proposed in the IEEE 802.11p model. The first tap showed a large Ricean K-factor, representing a strong LOS component. Later taps showed a Ricean K-factor less than 1. On the other side we found that the measured maximum significant delay is about one fifth of the maximum delay of the IEEE 802.11p model. This results in a faster decrease of the tap gain. Further, a standard tap delay model does not reflect the time variant behavior of the vehicular channel. The statistical properties of vehicular channels change over time (violation of WSS assumption) and may show correlated fading for different delays due to several MPCs interacting with one-and-the-same object (violation of US assumption). Consequently we developed a geometry-based stochastic MIMO V2V model considering this time variance [28].

7.2 IEEE 802.11p PHY Performance

IEEE 802.11p measurements for V2I links in Tyrol along the highway A12 have been analyzed with a focus on achievable range, achievable transmitted data volume, data rates, and reliability. The results only apply to a broadcast transmission mode.

Environmental effects, such as antenna height, electromagnetic wave propagation effects and traffic, were found to have a severe impact on the performance of the IEEE 802.11p system. Strong shadowing effects caused by trucks obstructing the LOS for the RSU were observed. This leads to a strongly fluctuating performance of the IEEE 802.11p system, especially for settings with long packet length and higher speed. Furthermore, the pattern of the antenna mounted on the gantry was found to be strongly influenced by the surrounding metal pillars. Hence, the coverage range became unsymmetrical. It turned out that certain metallic structures on the road cause significant focusing of the waves along the street, thus leading to a strongly increased coverage range of the RSU. This increased coverage was very peaky, hence it cannot be used for effective coverage extension. Thus, for site planning, this effect must be considered as additional interference, which has to be taken into account between neighboring RSUs. Unexpected throughput drop, caused by the poor equalizer capabilities of the receiver hardware, was observed for situations with a large number of MPCs at low SNR.

Beside the environmental effects, different parameter settings of the RSUs were considered. A maximum range of up to 900 m was achieved with a data rate of 3 Mbit/s at the low RSU ($h_{\mathrm{Tx}} = 1.8\,\mathrm{m}$) transmitting with a power of 16 dBm. At the low RSU this achievable range varies strongly with the traffic. The maximum achievable range at the high RSU ($h_{\mathrm{Tx}} = 7.1\,\mathrm{m}$) was about 700 m. This range decreases to about 100 m using the highest possible data rate of 27 Mbit/s.

I observed no variation of the achievable range for different packet length. The total received data volume is increasing, when longer packets are used. For the low RSU the achievable ranges and total data volume strongly depends on the driving direction. The reason for this is the lane where the vehicle is driving. When the vehicle is driving in direction west with 80 km/h it drives on the lane directly next to the RSU. If it is driving in direction east, there are three lanes between the OBU and the RSU. The traffic on these lanes is blocking the wave propagation from the RSU. In this case the achievable range and the correct received data volume are much smaller compared to driving in direction west. For the high RSU, no variation of the achievable ranges and received data volume at different driving directions could be observed. The maximum correct received data volume considering different data rates is achieved at low data rates of 4.5 Mbit/s, 6 Mbit/s and 9 Mbit/s.

The speed of the vehicles showed no influence on the achievable ranges. The total correct received data volume was higher in the case of the lower vehicle speed. The main reason for this difference is that the vehicle with the higher speed is passing the RSU faster and therefore there is less time, in order to transmit data.

For vehicular safety-related applications the high RSU antenna setting is recommended, because the performance of the low antenna position strongly depends on the traffic situation.

8

Future Directions / Outlook

ONE of the main contributions of this thesis is the description of how to conduct vehicular measurement campaigns in real-world scenarios. Further, methodologies for the evaluation of the collected measurement data are presented. The results are shown for several selected measurement examples. The next step will be the description of all measured scenarios by specific measures, like the RMS delay spread and RMS Doppler spread. With a description like that the differences between the scenarios can be pointed out. These evaluations are currently under investigation by our research group.

Another important characterization of the channel are directional analysis, which are possible with our collected MIMO measurement data. Colleagues are currently working on this evaluation [88]. This work can extend the scenario characterization by the RMS angular spread. Further channel models, beside our already available channel model for highway scenarios [28], are requested, in order to yield input for the higher layers in simulation tools.

The propagation conditions for V2V communications depend strongly on the mounting position of the antennas. Problems can occur, when the curvature of the vehicle roof blocks the direct "view" into the front of the vehicle, if the antenna is mounted on the back of the roof. The position of the vehicular antenna as well as the usage of multi-element antennas has to be investigated in more detail.

Until 2009 V2V scenarios were categorized by the "classical" scenarios highway, rural, urban, and suburban, where the vehicles were even driving in convoy or in opposite directions. As shown in this thesis the investigation of specific safety-related application scenarios, e.g., intersections, merging lanes, and traffic congestions, is more meaningful and should therefore be considered for future research.

The resulting radio channel characteristics, in particular the time-varying joint Doppler and delay spreads, have to be taken into account for future system design. The standard IEEE 802.11p, which will be implemented in the first commercial vehicular communication systems still has the potential for future improvements. Possible enhancements are the adaptation to multi-element antennas, in order to increase the diversity and thus the reliability of vehicular links, especially important for safety-related applications. Further a modification of the pilot patterns would improve the channel estimation and reduce the receiver complexity. We are currently working on these topics in the national research project ROADSAFE [89].

Overall, there are still many open research questions in the field of vehicular communications. These fascinating challenges and the implementation of the first commercial communication systems into vehicles in the near future are offering interesting and hot research topics for us.

List of Acronyms

ABS Anti-Lock Braking System

ACF Auto Correlation Function

APDP Average Power-Delay Profile

ASFINAG Autobahnen- und Schnellstraßen-Finanzierungs-AG

ASTM American Society for Testing and Materials

BP Band Pass

BPSK Binary Phase Shift Keying

C2C-CC Car-to-Car Communication Consortium

CALM Communication Architecture for Land Mobiles

cdf cumulative distribution function

COMeSafety Communications for eSafety

COOPERS Cooperative Systems for Intelligent Road Safety

CRC Cyclic Redundancy Check

CVIS Cooperative Vehicle-Infrastructure Systems

DSD Doppler Spectral Density

DPS Discrete Prolate Spheroidal

DSP Digital Signal Processing

DSRC Dedicated Short Range Communication

EC European Commission

EIRP Equivalent Isotropically Radiated Power

ETC Electronic Toll Collection

ETSI European Telecommunications Standards Institute

FCC Federal Communications Commission

FFT Fast Fourier Transform

FOT Field Operational Test

FSR Frame-Success-Ratio

GLSF Generalized Local Scattering Function

GPS Global Positioning System

ICC Inter Carrier Interference

IEEE Institute of Electrical and Electronics Engineers

IR Impulse Response

ISI Inter Symbol Interference

ISO International Organization for Standardization

ITRD International Transport Research Documentation

ITS Intelligent Transport Systems

LOS Line-of-Sight

LTI Linear Time Invariant

LTV Linear Time Variant

LSF Local Scattering Function

LTE Long Term Evolution

MAC Medium Access Control

MIMO Multiple-Input Multiple-Output

MMSE Minimum Mean Square Error

MPC Multipath Component

MPDU Medium Access Control Protocol Data Unit

MSDU Medium Access Control Service Data Unit

MSE Mean Square Error

NLOS Non-Line-of-Sight

NoW Network on Wheels

OBU Onboard Unit

OFDM Orthogonal Frequency Division Multiplexing

PCI Peripheral Component Interconnect

pdf probability density function

PDP Power-Delay Profile

PHY Physical Layer

PLCP PHY Convergence Procedure

PMD Physical Medium Dependent

PReVENT Preventive and Active Safety Applications

PROMETHEUS Programme for a European Traffic of Highest Efficiency and Unprecedented Safety

PS Parameter Setting

PSDU PHY Sublayer Data Unit

QPSK Quadrature Phase Shift Keying

RF Radio Frequency

RFID Radio Frequency Identification

RMS Root Mean Square

RSU Roadside Unit

Rx Receiver

SAFESPOT Safe Cooperative Driving — Smart Vehicles on Smart Roads

SIM-TD Sichere Intelligente Mobilität — Testfeld Deutschland

SISO	Single-Input Single-Output
SNR	Signal-to-Noise-Ratio
TC	Technical Committee
TF	Transfer Function
TG	Task Group
Tx	Transmitter
ULA	Uniform Linear Array
UMTS	Universal Mobile Telecommunications System
US	Uncorrelated Scattering
V2I	Vehicle-to-Infrastructure
V2V	Vehicle-to-Vehicle
VSWR	Voltage Standing Wave Ratio
WAVE	Wireless Access in Vehicular Environments
WiMAX	Worldwide Interoperability for Microwave Access
WLAN	Wireless Local Area Network
WSS	Wide-Sense Stationary
WSSUS	Wide-Sense Stationary Uncorrelated Scattering

List of Symbols

Lowercase symbols	**Description**
c_0	speed of light
c_{thres}	threshold for stationarity time
d	distance
d_{achiev}	achievable range
f	continuous frequency
f_{c}	center frequency
h	time-variant impulse response
h_{ant}	antenna height
h_{Rx}	Rx antenna height
h_{Tx}	Tx antenna height
i	index counter
j	index counter
j	imaginary unit
k	discrete time index
k_0	wavenumber
l	discrete delay index
l_i	tap delay index
m	discrete Doppler index
n	pathloss exponent
n_f	index counter for frequency
n_t	index counter for time
p	single antenna element link number
q	discrete frequency index
r	signal envelope
r	index of the prototype system

t	continuous time
t_{av}	averaging time
t_{rec}	recording time
t_{rep}	snapshot repetition time
t_{snap}	snapshot time
u	discrete prolate spheroidal sequence
v	speed
x	input signal
y	output signal

Uppercase symbols	**Description**
B	Doppler-variant transfer function
BW	bandwidth
B_{coh}	coherence bandwidth
B_{stat}	stationarity bandwidth
$\mathcal{F}$	Fourier transform
FS	file size
FSR	frame-success-ratio
G_{12}	pathloss constant
G_{ch}	channel gain
$\boldsymbol{G}_r$	linear time-variant prototype filter
$G_{\mathrm{Rx,iso}}$	Rx antenna gain
$G_{\mathrm{Tx,iso}}$	Tx antenna gain
H	time-variant transfer function
$H_{\boldsymbol{G}_r}$	transfer function of linear time-variant prototype filter
$\mathcal{H}^{(\boldsymbol{G}_r)}$	single generalized LSF
I	maximum index
$\mathcal{I}$	interval
J	maximum index
K	maximum time index
K_{av}	averaging time in snapshots
K_{Rice}	Ricean K-factor
M_{Rx}	number of Rx antenna elements
M_{Tx}	number of Tx antenna elements
N_{cbps}	number of coded bits per symbol
N_{bpsc}	number of coded bits per subcarrier
N_{data}	number of data bits

N_{dbps}	number of data bits per symbol
N_f	overall number of frequency bins
$N_{\mathrm{frame,corr}}$	number of correctly received OFDM frames
$N_{\mathrm{frame,Tx}}$	number of transmitted frames
N_{MSDU}	MSDU length (packet length)
N_{PSDU}	PSDU length
N_{sym}	number of OFDM symbols
N_t	overall number of snapshots
P	maximum number of antenna element links
P_{Rx}	received power
P_{APDP}	average power-delay profile
P_B	Doppler cross power spectral density
$P_{\mathrm{B,m}}$	Doppler power
P_{DD}	delay Doppler spectrum
P_{DSD}	Doppler spectral density
P_h	delay cross power spectral density
P_{tap}	tap gain
P_{Tx}	transmitted power
$\widetilde{\widetilde{P_S}}$	part of the ACF of the delay Doppler function for WSS
$\widetilde{P_S}$	part of the ACF of the delay Doppler function for US
P_S	scattering function
$\mathcal{P}_S$	local scattering function
$\widetilde{\mathcal{P}_S}$	generalized LSF
PL_c	pathloss correction term
Q	maximum frequency index
R	maximum index of prototype system
R_{data}	data rate
R_B	ACF of the Doppler-variant transfer function
R_h	ACF of the impulse response
R_H	ACF of the time-variant transfer function
$\mathcal{R}_h$	4-dim ACF in the non-WSSUS case
R_S	ACF of the delay Doppler function
R_{xx}	ACF of the input signal
R_{yy}	ACF of the output signal
$R_{\widetilde{\mathcal{P}_S}}$	collinearity of the generalized LSF
S	delay Doppler function

T_{coh}	coherence time
T_{stat}	stationarity time
V_{achiev}	achievable data volume
V_{theo}	theoretical data volume
V_{total}	total data volume
X	input spectrum
X_{σ_1}	normally distributed random variable 1
X_{σ_2}	normally distributed random variable 2
Y	output spectrum

Greek symbols	**Description**
γ	incident angle
γ_r	coefficient for generalized LSF
γ_{thresh}	FSR threshold
$\delta(\cdot)$	dirac impulse
Δf	frequency difference
Δt	time difference
$\Delta\tau$	delay difference
$\Delta\nu$	Doppler difference
λ	wavelength
ν	continuous Doppler
$\bar{\nu}$	mean Doppler
ν_{RMS}	Doppler spread
ν_{max}	maximum Doppler shift of the channel
ρ	reflection coefficient
σ	standard deviation
τ	continuous delay
$\bar{\tau}$	mean delay
τ_{max}	maximum delay of the channel
$\tau_{\text{max, CS}}$	test signal length of the channel sounder
τ_{RMS}	RMS delay spread
ζ	forward/reverse pathloss coefficient

Bibliography

[1] L. Cheng, B. Henty, D. Stancil, F. Bai, and P. Mudalige, "Mobile vehicle-to-vehicle narrow-band channel measurement and characterization of the 5.9 GHz dedicated short range communication (DSRC) frequency band," *IEEE J. Sel. Areas Commun.*, vol. 25, pp. 1501–1516, 2007.

[2] L. Cheng, B. Henty, D. D. Stancil, F. Bai, and P. Mudalige, "A fully mobile, GPS enabled, vehicle-to-vehicle measurement platform for characterization of the 5.9 GHz DSRC channel," in *Proc. IEEE Antennas Propagation Soc. Int. Symp.*, pp. 2005–2008, 2007.

[3] J. Maurer, T. Fügen, and W. Wiesbeck, "Narrow-band measurement and analysis of the inter-vehicle transmission channel at 5.2 GHz," in *Proc. IEEE Veh. Technol. Conf. 2002 spring*, pp. 1274–1278, 2002.

[4] A. F. Molisch, *Wireless Communications.* IEEE-Press - Wiley and Sons, 2005.

[5] I. Sen and D. Matolak, "Vehicle–vehicle channel models for the 5-GHz band," *IEEE Trans. Intell. Transp. Syst.*, vol. 9, no. 2, pp. 235–245, 2008.

[6] L. Cheng, B. Henty, R. Cooper, D. Stancil, and F. Bai, "Multi-path propagation measurements for vehicular networks at 5.9 GHz," in *Proc. IEEE Wireless Commun. Networking Conf.*, pp. 1239–1244, 2008.

[7] G. Acosta and M. A. Ingram, "Model development for the wideband expressway vehicle-to-vehicle 2.4 GHz channel," in *IEEE Wireless Communications and Networking Conference (WCNC) 2006*, 3-6 April 2006.

[8] I. Tan, W. Tang, K. Laberteaux, and A. Bahai, "Measurement and analysis of wireless channel impairments in DSRC vehicular communications," in *Proc. IEEE Int. Conf. Commun.*, pp. 4882–4888, 2008.

[9] P. Paschalidis, M. Wisotzki, A. Kortke, W. Keusgen, and M. Peter, "A wideband channel sounder for car-to-car radio channel measurements at 5.7 GHz and results for an urban scenario," in *Proc. IEEE Veh. Technol. Conf. 2008 fall*, September 2008.

[10] J. Kunisch and J. Pamp, "Wideband car-to-car radio channel measurements and model at 5.9 GHz," in *Proc. IEEE Veh. Technol. Conf. 2008 fall*, 2008.

[11] A. Paier, J. Karedal, N. Czink, H. Hofstetter, C. Dumard, T. Zemen, F. Tufvesson, C. F. Mecklenbräuker, and A. F. Molisch, "First results from car-to-car and car-to-infrastructure radio channel measurements at 5.2 GHz," in *International Symposium on Personal, Indoor and Mobile Radio Communications (PIMRC 2007)*, pp. 1–5, 3-7 September 2007.

[12] A. Paier, L. Bernadó, J. Karedal, O. Klemp, and A. Kwoczek, "Overview of vehicle-to-vehicle radio channel measurements for collision avoidance applications," in *71st IEEE Vehicular Technology Conference*, (Taipei, Taiwan), 16-19 May 2010.

[13] O. Renaudin, V. M. Kolmonen, P. Vainikainen, and C. Oestges, "Wideband MIMO car-to-car radio channel measurements at 5.3 GHz," in *Proc. IEEE Veh. Technol. Conf. 2008 fall*, September 2008.

[14] A. F. Molisch, F. Tufvesson, J. Karedal, and C. F. Mecklenbräuker, "A survey on vehicle-to-vehicle propagation channels," *IEEE Wireless Communications Magazine, special issue on "On-the-Road communications"*, vol. 16, pp. 12–22, December 2009.

[15] G. Matz, "On non-WSSUS wireless fading channels," *IEEE Transactions on Wireless Communications*, vol. 4, pp. 2465–2478, September 2005.

[16] Z. Wang and G. B. Giannakis, "Wireless multicarrier communications," *IEEE Signal Process. Mag.*, vol. 17, pp. 29–48, May 2000.

[17] S. B. Weinstein and P. M. Ebert, "Data transmission by frequency-divison multiplexing using the discrete Fourier transform," *IEEE Trans. Commun.*, vol. 19, pp. 628–634, October 1971.

[18] M. Wellens, B. Westphal, and P. Mahonen, "Performance evaluation of IEEE 802.11-based WLANs in vehicular scenarios," in *Proc. IEEE Veh. Technol. Conf. 2007 spring*, pp. 1167–1171, April 2007.

[19] L. Cheng, B. E. Henty, R. Cooper, and D. D. Stancil, "A measurement study of time-scaled 802.11a waveforms over the mobile-to-mobile vehicular channel at 5.9 GHz," *IEEE Communications Magazine*, vol. 46, pp. 84–91, May 2008.

[20] D. Jiang and L. Delgrossi, "IEEE 802.11p: Towards an international standard for wireless access in vehicular environments," in *Proc. IEEE Veh. Technol. Conf. 2008 spring*, pp. 2036–2040, May 2008.

[21] S. Eichler, "Performance evaluation of the IEEE 802.11p WAVE communication standard," in *Proc. IEEE Veh. Technol. Conf. 2007 fall*, pp. 2199–2203, September 2007.

[22] L. Stibor, Y. Zang, and H.-J. Reumerman, "Evaluation of communication distance of broadcast messages in a vehicular ad-hoc network using IEEE 802.11p," in *IEEE Wireless Communications and Networking Conference (WCNC 2007)*, pp. 254–257, March 2007.

[23] A. Paier, J. Karedal, N. Czink, H. Hofstetter, C. Dumard, T. Zemen, F. Tufvesson, A. F. Molisch, and C. F. Mecklenbräuker, "Car-to-car radio channel measurements at 5 GHz: Pathloss, power-delay profile, and delay-Doppler spectrum," in *IEEE International Symposium on Wireless Communication Systems (ISWCS 2007)*, pp. 224–228, 17-19 October 2007.

[24] A. Paier, J. Karedal, N. Czink, C. Dumard, T. Zemen, F. Tufvesson, A. Molisch, and C. F. Mecklenbräuker, "Characterization of vehicle-to-vehicle radio channels from measurements at 5.2GHz," *Wireless Personal Commun.*, vol. 50, pp. 19–29, 2009.

[25] J. Karedal, N. Czink, A. Paier, F. Tufvesson, and A. F. Molisch, "Pathloss modeling for vehicle-to-vehicle communications," *IEEE Trans. Veh. Technol.*, 2010. submitted, second round of reviews.

[26] A. Paier, T. Zemen, L. Bernadó, G. Matz, J. Karedal, N. Czink, C. Dumard, F. Tufvesson, A. F. Molisch, and C. F. Mecklenbräuker, "Non-WSSUS vehicular channel characterization in highway and urban scenarios at 5.2 GHz using the local scattering function," in *Smart Antennas, 2008. WSA 2008. International ITG Workshop on*, (Darmstadt, Germany), pp. 9 –15, 26-27 February 2008.

[27] L. Bernadó, T. Zemen, A. Paier, J. Karedal, and B. Fleury, "Parametrization of the local scattering function estimator for vehicular-to-vehicular channels," in *Vehicular Technology Conference Fall (VTC 2009-Fall), 2009 IEEE 70th*, (Anchorage, Alaska, USA), pp. 1 –5, September 2009.

[28] J. Karedal, F. Tufvesson, N. Czink, A. Paier, C. Dumard, T. Zemen, C. F. Mecklenbräuker, and A. F. Molisch, "A geometry-based stochastic MIMO model for vehicle-to-vehicle communications," *IEEE Trans. Wireless Commun.*, vol. 8, pp. 3646–3657, July 2009.

[29] J. Karedal, F. Tufvesson, N. Czink, A. Paier, C. Dumard, T. Zemen, C. F. Mecklenbräuker, and A. F. Molisch, "Measurement-based modeling of vehicle-to-vehicle MIMO channels," in *Communications, 2009. ICC '09. IEEE International Conference on*, pp. 1 –6, June 2009.

[30] J. Karedal, F. Tufvesson, T. Abbas, O. Klemp, A. Paier, L. Bernadó, and A. F. Molisch, "Radio channel measurements at street intersections for vehicle-to-vehicle safety applications," in *Vehicular Technology Conference (VTC 2010-Spring), 2010 IEEE 71st*, pp. 1 –5, May 2010.

[31] A. Thiel, O. Klemp, A. Paier, L. Bernadó, J. Karedal, and A. Kwoczek, "In-situ vehicular antenna integration and design aspects for vehicle-to-vehicle communications," in *4th European Conference on Antennas and Propagation*, (Barcelona, Spain), April 2010.

[32] A. Paier, R. Tresch, A. Alonso, D. Smely, P. Meckel, Y. Zhou, and N. Czink, "Average downstream performance of measured IEEE 802.11p infrastructure-to-vehicle links," in *IEEE International Conference on Communications, Workshop on Vehicular Connectivity*, (Cape Town, South Africa), 23-27 May 2010.

[33] C. F. Mecklenbräuker, A. F. Molisch, J. Karedal, F. Tufvesson, A. Paier, L. Bernadó, T. Zemen, O. Klemp, and N. Czink, "Vehicular channel characterization and its implications for wireless system design and performance," *Proceedings of the IEEE, Special Issue on Vehicular Communications*, Spring 2011. submitted, second round of reviews.

[34] A. Paier, T. Zemen, J. Karedal, N. Czink, C. Dumard, F. Tufvesson, C. F. Mecklenbräuker, and A. Molisch, "Spatial diversity and spatial correlation evaluation of measured vehicle-to-vehicle radio channels at 5.2 GHz," in *Digital Signal Processing Workshop and 5th IEEE Signal Processing Education Workshop, 2009. DSP/SPE 2009. IEEE 13th*, pp. 326 –330, January 2009.

[35] A. Alonso, A. Paier, T. Zemen, N. Czink, and F. Tufvesson, "Capacity evaluation of measured vehicle-to-vehicle radio channels at 5.2 GHz," in *Communications Workshops (ICC), 2010 IEEE International Conference on*, pp. 1 –5, May 2010.

[36] A. Alonso, C. F. Mecklenbräuker, A. Paier, T. Zemen, N. Czink, and F. Tufvesson, "Temporal evolution of channel capacity in vehicular MIMO channels in the 5 GHz band," in *20th International Symposium on Electromagnetic Theory*, (Berlin, Germany), August 2010.

[37] L. Bernadó, T. Zemen, A. Paier, G. Matz, J. Karedal, N. Czink, C. Dumard, F. Tufvesson, M. Hagenauer, A. F. Molisch, and C. F. Mecklenbräuker, "Non-WSSUS vehicular channel characterization at 5.2 GHz - spectral divergence and time-variant coherence parameters," in *Proceedings of the XXIXth URSI General Assembly*, (Chicago, Illinois, USA), August 2008.

[38] L. Bernadó, T. Zemen, J. Karedal, A. Paier, A. Thiel, O. Klemp, N. Czink, F. Tufvesson, A. F. Molisch, and C. F. Mecklenbräuker, "Multi-dimensional K-factor analysis for V2V radio channels in open sub-urban street crossings," in *International Symposium on Personal, Indoor and Mobile Radio Communications (PIMRC 2010)*, (Istanbul, Turkey), September 2010.

[39] P. Belanovic, D. Valerio, A. Paier, T. Zemen, F. Ricciato, and C. F. Mecklenbräuker, “On wireless links for vehicle-to-infrastructure communications,” *Vehicular Technology, IEEE Transactions on*, vol. 59, pp. 269 –282, January 2010.

[40] W. Karner, A. Paier, and M. Rupp, “Indoor coverage prediction and optimization for UMTS macro cells,” in *Wireless Communication Systems, 2006. ISWCS ’06. 3rd International Symposium on*, pp. 625 –630, September 2006.

[41] “International transport research documentation.” http://www.itrd.org.

[42] ETSI TR 102 638, “Intelligent transport sytems (ITS); vehicular communications; basic set of applications; definitions.” V1.1.1, June 2009.

[43] “Communications for eSafety.” http://www.comesafety.org. COMeSafety.

[44] “Car-to-car communications consortium.” http://www.car-2-car.org.

[45] “PReVent.” http://www.prevent-ip.org/en/home.htm.

[46] “Network on Wheels.” http://www.network-on-wheels.de.

[47] “Safespot (Integrated Project), Contract No. IST-4-026963-IP.” http://www.safespot-eu.org.

[48] “Cooperative vehicle-infrastructure systems.” http://www.cvisproject.org.

[49] “Co-operative systems for intelligent road safety, contract no. FP6-2004-IST-4 Nr. 026814.” http://www.coopers-ip.eu.

[50] “Preparation for driving implementation and evaluation of C2X communication technology.” http://www.pre-drive-c2x.eu.

[51] “Safe and Intelligent Mobility – Test Field Germany (SIM-TD).” http://www.simtd.de.

[52] “IEEE trial-use standard for wireless access in vehicular environments (WAVE) - resource manager,” *IEEE Std 1609.1-2006*, 2006.

[53] “IEEE trial-use standard for wireless access in vehicular environments - security services for applications and management messages,” *IEEE Std 1609.2-2006*, July 2006.

[54] “IEEE trial-use standard for wireless access in vehicular environments (WAVE) - networking services,” *IEEE Std 1609.3-2007*, April 2007.

[55] “IEEE trial-use standard for wireless access in vehicular environments (WAVE) - multi-channel operation,” *IEEE Std 1609.4-2006*, November 2006.

[56] “Commission decision on the harmonised use of radio spectrum in the 5875-5905 MHz frequency band for safety-related applications of intelligent transport systems (ITS).” 2008/671/EC, August 2008.

[57] “European Telecommunications Standards Institute.” http://www.etsi.org.

[58] J. C. Maxwell, “A dynamical theory of the electromagnetic field,” *Philosophical Transactions of the Royal Society of London*, vol. 155, pp. 459–512, 1865.

[59] P. A. Bello, “Characterization of randomly time-variant linear channels,” *IEEE Transactions on Communications*, vol. 11, pp. 360–393, 1963.

[60] M. Steinbauer, *The Radio Propagation Channel — A Non-Directional, Directional, and Double-Directional Point-of-View*. PhD thesis, Technische Fakultät Wien, 2001.

[61] S. O. Rice, “Mathematical analysis of random noise,” *Bell System Technical Journal*, vol. 24, pp. 46–156, January 1945.

[62] R. E. Collins, *Field Theory of Guided Waves.* IEEE Press, 1991.

[63] D. Marcuse, *Theory of Dielectric Optical Waveguides, (2nd edn.).* Academic Press, 1992.

[64] A. V. Oppenheim and R. W. Schafer, *Discrete-time Signal Processing.* Prentice Hall, 1985.

[65] R. Kattenbach, *Charakterisierung zeitvarianter Indoor-Funkkanäle anhand ihrer System- und Korrelationsfunktionen.* PhD thesis, Universitätsgesamthochschule Kassel, 1997.

[66] G. Matz, "Doubly underspread non-WSSUS channels: Analysis and estimation of channel statistics," in *Proc. IEEE Int. Workshop Signal Processing Advance Wireless Communications (SPAWC)*, (Rome, Italy), pp. 190–194, June 2003.

[67] D. J. Thomson, "Spectrum estimation and harmonic analysis," *Proc. IEEE*, vol. 70, pp. 1055–1096, September 1982.

[68] D. B. Percival and A. T. Walden, *Spectral Analysis for Physical Applications.* Cambridge University Press, 1963.

[69] B. Fleury, "An uncertainty relation for WSS processes and its application to WSSUS systems," *IEEE Transactions on Communications*, vol. 44, pp. 1632 –1634, December 1996.

[70] "REALSAFE." https://portal.ftw.at/projects/realsafe.

[71] "MEDAV GmbH." http://www.medav.de.

[72] R. Thomä, D. Hampicke, A. Richter, G. Sommerkorn, A. Schneider, U. Trautwein, and W. Wirnitzer, "Identification of time-variant directional mobile radio channels," *IEEE Trans. on Instrumentation and Measurement*, vol. 49, pp. 357–364, 2000.

[73] A. Paier, J. Karedal, T. Zemen, N. Czink, C. Dumard, F. Tufvesson, C. F. Mecklenbräuker, and A. F. Molisch, "Description of vehicle-to-vehicle and vehicle-to-infrastructure radio channel measurements at 5.2 GHz," in *COST2100 Action meeting, TD(08)636*, 6-8 October 2008.

[74] "RIEGL Laser Measurement Systems GmbH." http://www.riegl.com.

[75] "Satellite photographs." http://hitta.se.

[76] IEEE 802.11p, "Draft standard for information technology - telecommunications and information exchange between systems - local and metropolitan area networks - specific requirements: Wireless access in vehicular environments." IEEE P802.11p/D9.0, September 2009.

[77] "Q-Free." http://www.q-free.com.

[78] "Smarteq." http://www.smarteq.se.

[79] "Autobahnen- und Schnellstraßen-Finanzierungs-AG." http://www.asfinag.at/.

[80] IEEE 802.11p, "Draft amendment to wireless LAN medium access control (MAC) and physical layer (PHY) specifications: Wireless access in vehicular environments." IEEE P802.11p/D0.26, January 2006.

[81] J. Medbo and J.-E. Berg, "Simple and accurate path loss modeling at 5 GHz in indoor environments with corridors," in *Vehicular Technology Conference, 2000. IEEE VTS-Fall VTC 2000. 52nd*, vol. 1, pp. 30 –36 vol.1, 24-28 September 2000.

[82] D. Slepian, "Prolate spheroidal wave functions, Fourier analysis, and uncertainty - V: The discrete case," *The Bell System Technical Journal*, vol. 57, pp. 1371–1430, May-June 1978.

[83] A. Gehring, M. Steinbauer, I. Gaspard, and M. Grigat, "Empirical channel stationarity in urban environments," in *Proc. Eur. Personal Mobile Communications Conf. (EPMCC)*, (Vienna, Austria), February 2001.

[84] G. Acosta-Marum and M. A. Ingram, “A BER-based partitioned model for a 2.4 GHz vehicle-to-vehicle expressway channel,” *Wireless Personal Communications (WPC)*, pp. 421–443, July 2006.

[85] G. Acosta, K. Tokuda, and M. A. Ingram, “Measured joint Doppler-delay power profiles for vehicle-to-vehicle communications at 2.4 GHz,” in *Global Telecommunications Conference 2004*, 29 November - 3 December 2004.

[86] A. Paier, J. Karedal, N. Czink, C. Dumard, T. Zemen, F. Tufvesson, A. F. Molisch, and C. F. Mecklenbräuker, “Comparison of LUND’07 vehicular channel measurements with the IEEE 802.11p channel model,” in *COST2100 Action meeting, TD(08)436*, 6-8 February 2008.

[87] L. J. Greenstein, D. G. Michelson, and V. Erceg, “Moment-method estimation of the Ricean K-factor,” *IEEE Communications Letters*, vol. 3, pp. 175–176, June 1999.

[88] T. Abbas, J. Karedal, F. Tufvesson, A. Paier, O. Klemp, L. Bernadó, and A. F. Molisch, “Directional analysis of vehicle-to-vehicle propagation channels,” in *Proc. IEEE Veh. Technol. Conf.*, (Budapest, Hungary), May 2011. extended abstract submitted.

[89] “ROADSAFE.” https://portal.ftw.at/projects/roadsafe.